Universität Hamburg
DER FORSCHUNG | DER LEHRE | DER BILDUNG

CLUSTER OF EXCELLENCE
QUANTUM UNIVERSE

INSTITUT FÜR QUANTENPHYSIK

Towards a high-power tabletop prototype of the HF Einstein Telescope

Dissertation

zur Erlangung des Doktorgrades
an der Fakultät für Mathematik, Informatik und Naturwissenschaften
Fachbereich Physik
der Universität Hamburg

vorgelegt von
Justin Nico Hohmann

Hamburg
2024

Gutachter/innen der Dissertation	Prof. Dr. Roman Schnabel Prof. Dr. Oliver Gerberding
Zusammensetzung der Prüfungskommission:	Prof. Dr. Roman Schnabel Prof. Dr. Oliver Gerberding Prof. Dr. Ludwig Mathey Prof. Dr. Henning Moritz Prof. Dr. Ralf Riedinger
Vorsitzende/r der Prüfungskommission	Prof. Dr. Ludwig Mathey
Datum der Disputation	26.06.2024
Vorsitzender Fach-Promotionsausschusses PHYSIK:	Prof. Dr. Markus Drescher
Leiter des Fachbereichs PHYSIK:	Prof. Dr. Wolfgang J. Parak
Dekan der Fakultät MIN:	Prof. Dr.-Ing. Norbert Ritter

Abbreviations

LIGO	Laser Interferometer Gravitational-Wave Observatory
ET	Einstein Telescope
HF	high frequency
LF	low frequency
GW	gravitational wave
GWO	gravitational wave observatory
GWD	gravitational wave detector
BS	beam splitter
PBS	polarizing beam splitter
EOM	electro optic modulator
PMC	pre-mode cleaner
TM	test mass
EITM	east input test mass
NITM	north input test mass
EETM	east end test mass
NETM	north end test mass
FI	Faraday isolator
PD	photo detector
RPD	resonant photo detector
LO	local oscillator
HV	high voltage
PID	proportional-integral-derivative
FSR	free spectral range
ROC	radius of curvature
X arm	the beam path in transmission of the central BS
Y arm	the beam path in reflection of the central BS
PDF	probability density function
KDE	kernel density estimation
PSD	power spectral density
PR	power recycling
RSE	resonant sideband extraction
SR	signal recycling

Abstract

Gravitational wave detection gives information about events in the universe, that can not be observed, using electromagnetic radiation, like black holes merging with each other or with neutron stars. Since the first verified measurement of a binary black hole merger in 2015 it is proven, that more sensitive detectors will increase the number of detection, allowing us to improve our cosmological models. Such a planned observatory for the future is the Einstein Telescope (ET).

Gravitational wave detectors like the ET with kilometres of resonator length rely on a good alignment of all optics, such that the beams overlap well and a good mode matching and alignment is achieved. Misalignment between carrier and squeezed light states induces optical loss and decreases the sensitivity.

In the Hamburg ET high frequency tabletop prototype with arm resonators we use suspended, weighted and curved mirrors, that we steer, using several actuators. All four test masses have piezo motor driven marionette suspensions, that allow an individual alignment under vacuum conditions, with measured pendulum frequencies between 5.7 Hz and 7.2 Hz.

The mirror position can be controlled with sub-nanometre precision. Thus it is possible to control alignment and mode matching precisely. Using the end mirrors, a lateral and vertical precision of 0.3 µrad can be reached with the suspension. The interferometer is aligned to contrast values greater than 99.9 % and the arm resonator mode matchings at least 95 %.

Furthermore the Michelson fringe can be locked to a dark fringe, as long as the seismic excitations are small enough. An active stabilisation of the 30 t concrete block, which is the fundament of the experiment, was necessary. Additionally, the arm cavities can be held on resonance simultaneously by using a combination of the Pound-Drever-Hall technique, thermal actors and a piezo, that are installed in the test masses, to control the

arm length. All locks are possible despite the compact design of the vacuum chamber with a height of only 23 cm.

Moreover the sensitivity for gravitational waves at the frequency of one FSR (free spectral range) of the arm resonators, which is 164 MHz, is discussed. The prototype will help to examine the influence of mismatch on sensitivity, thermal lensing effects and other challenges in GWOs.

Kurzfassung

Gravitationswellendetektion liefert Informationen über Ereignisse im Weltraum, die wir nicht im elektromagnetischen Spektrum beobachten können, wie Verschmelzungen von schwarzen Löchern miteinander oder mit Neutronensternen. Seit der ersten bestätigten Messung von zwei verschmolzenen schwarzen Löchern ist es bewiesen, dass empflindlichere Detektoren die Anzahl an Messungen erhöhen und uns damit erlauben die kosmologischen Modelle zu verbessern. Solch ein geplantes Observatorium ist das Einstein-Teleskop (ET).

Gravitationswellendetektoren wie das ET mit Kilometer-langen Resonatoren sind sehr abhängig von guter Justage aller Optiken, damit eine gute Strahlüberlagerung, Modenanpassung und Justage erreicht wird. Fehljustage zwischen optischem Träger und gequetschen Lichtzuständen führt zu optischem Verlust und verringert die Empfindlichkeit.

Im Hamburger ET hochfrequenz Prototypen mit Armresonatoren benutzen wir aufgehängte, gewichtete und gekrümmte Spiegel, die wir mithilfe mehrerer Aktoren steuern. Alle vier Testmassen haben Piezomotor getriebene Marionettenaufhängungen, die eine individuelle Steuerung unter Vakuumbedingungen erlauben, bei gemessenen Pendelfrequenzen von 5.7 Hz bis 7.2 Hz.

Die Spiegelposition kann mit sub-nanometer Präzision gesteuert werden. Daher ist es möglich die Justage und die Modenanpassung genau zu steuern. Mit den Endspiegeln wurde eine vertikale und laterale Präzision von 0.3 µrad mithilfe der Aufhängung erreicht. Das Interferometer erreicht Kontrastwerte größer als 99.9 % und die Modenanpassungen der Armresonatoren beträgt mindestens 95 %.

Zusätzlich kann der Ausgang des Michelson Interferometers am dunklen Ausgang stabilisiert werden, sofern die seismischen Anregungen klein genug sind. Eine aktive Stabilisierung des 30 t schweren Betonblocks, der das Fundament bildet, war erforderlich. Des weiteren können die Arm Kavitäten gleichzeitig auf Resonanz gehalten werden, indem eine Kombination des Pound-Drever-Hall Verfahrens mit thermischen Aktoren und einem Piezo, die in den Testmassen verbaut sind, um die Armlänge zu regeln, verwendet wird. Alle Regelzustände sind trotz der kompakten Gestaltung der Vakuumkammer mit einer Höhe von nur 23 cm möglich.

Darüber hinaus wird die Empfindlichkeit für Gravitationswellen bei der Frequenz von einem FSR (free spectral range) der Armresonatoren, welche 164 MHz beträgt, diskutiert. Der Prototyp wird helfen den Einfluss von Fehljustagen auf die Sensitivität, thermischen Linsen und andere Herausforderungen in Gravitaionswellenobservatorien zu untersuchen.

This document uses the ComponentLibrary by Alexander Franzen, which is licensed under a Creative Commons Attribution-NonCommercial 3.0 Unported License [1]. Partly the symbols have been altered. The used symbols are:

Optical components

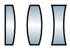 lenses

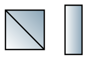 (polarising) beamsplitters

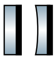 mirrors

 piezo coupled mirror

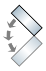 flip mirror

 fiber output coupler

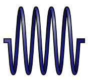 optical fiber

 wave plates

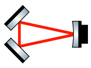 mode cleaner cavity

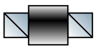 Faraday isolators

 beam dumps

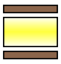 electro-optic modulators

 laser beams

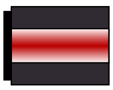 laser

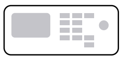 spectrum analyzer

 photodetector

Electronical components

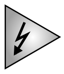 HV amplifier

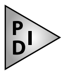

servo

 mixer

 signal generator

 sum

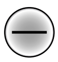 difference

 sum/difference

 low pass filter

 high pass filter

 band pass filter

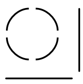 electrical wires

Contents

1 Introduction

Looking into the starry night humans have been riddling about the processes in space for millennia. When it comes to describing the motion of planets, moons and other stellar objects, humans came a long way in the description of the universe formed by gravity. When Newton described his understanding of the universe in his work *Philosophiae Naturalis Principia Mathematica*, he also had definitions for absolute and relative space and time [2]. His work on the movement and law of gravity explained a lot what remained a mystery until then. The elliptical trajectories of the planets and the returning Halley comet are only two examples of their effect on explaining stellar objects and their orbits [3]. But even Newtons theory left unresolved questions itself, as an example the movement of Mercury's perihelion remained unexplained.

When Albert Einstein developed his theory of general relativity the understanding of gravity changed. It was no longer a force between two massive objects, but became a property of space-time itself, which is influenced by mass. Not only did his equations explain Mercury's movement, but also predicted new, undiscovered physics, which was proven about a century later [4, 5, 6].

1.1 Gravitational waves

After publishing the general theory of relativity Einstein also predicted the existence of gravitational waves as a solution of his equations. These are ripples in the space-time, comparable to surface waves of an infinite plane of fabric, which gets bend by marbles rolling on it. The waves are created by moving mass, since the gravitational fields of the masses propagate with the speed of light c, which is after all a finite number. [7, Ch.2].

For decades scientist built detectors to find these waves. There was an approach to detect gravitational waves with resonant bar detectors, whose resonance frequencies would be changed by the influence of gravitational waves. Weber, who build the detectors also claimed to have found gravitational radiation, but because no one else could reproduce his findings in similar experiments, they were considered implausible [8, 9].

The first reliable hint on gravitational waves was delivered by Hulse and Taylor in 1981, who investigated a pulsar in a binary system. Their data showed a decreasing of the orbit period and their calculations indicated, that the loss of energy fits the emission of gravitational waves, suggested by Einsteins equations. They got the Nobel price for the finding of the pulsar in the binary system in 1993 [10, 11].

The search for gravitational waves had started and laser interferometric detectors were build. The Laser Interferometer Gravitational-Wave Observatory (LIGO), using two four kilometre Michelson interferometers, announced the first verified detection of gravitational waves in 2015 [4].

The waves have a quadrupole nature and while propagating along an axis, the effect takes place in the plane orthogonal to it. In this plane the space-time is compressed in one direction and stretched in the perpendicular one. This property makes Michelson interferometers suitable detectors, because they compare the length of two orthogonal paths to each other on the scale of the wavelength of light. The amplitude of these perturbations is called *strain* and defined as the normalised length change $h = L/L_0$, where L is the disturbed and L_0 the undisturbed length.

The use of gravitational wave detection is among others the probing of the universe and the models we have of it. Analysing the wave signals gives information about their sources. The observatories already detected merging black holes and neutron stars [4, 12, 13]. Other possible sources, that might be detected in the future, are among other pulsars, supernovae and the stochastic background [7]. Collecting these data about the events incidence frequency and spatial distribution can be compared to the present models of the universe [14].

There is an ongoing strive in the scientific community to improve the existing observatories and plan newer generations, so that a higher rate of gravitational waves can be measured. This will allow to verify or improve the existing models of cosmology, since it can provide information, that electromagnetic waves can not.

The possible existence of gravitational waves derives from the theory of general relativity by Albert Einstein. A more detailed derivation can be found in [7, ch.2, 3], which is summarised here. In the four dimensional space-time a distance is given by the interval ds and defined by

$$ds^2 = -c^2dt^2 + dx^2 + dy^2 + dz^2. \tag{1.1}$$

It uses the Minkowski metric $\eta_{\mu\nu}$, which is given in Cartesian coordinates by

$$\eta_{\mu\nu} = \begin{pmatrix} -1 & 0 & 0 & 0 \\ 0 & 1 & 0 & 0 \\ 0 & 0 & 1 & 0 \\ 0 & 0 & 0 & 1 \end{pmatrix}. \tag{1.2}$$

The indices μ and ν are indicating the use of the summation convention over doubly occurring indices. Both stand for the dimensions t,x,y and z. This way we can represent ds as

$$ds^2 = g_{\mu\nu}dx^\mu dx^\nu, \tag{1.3}$$

using a modified tensor

$$g_{\mu\nu} = \eta_{\mu\nu} + h_{\mu\nu}, \tag{1.4}$$

that includes small perturbations. In the weak-field limit approximations can be made to reduce the non-linear equations to linear ones. The use of the ”TT gauge” -transverse traceless gauge- is a choice of coordinates, that makes the field equation a wave equation

$$\left(\nabla^2 - \frac{1}{c^2}\frac{\partial^2}{\partial t^2}\right) h_{\mu\nu} = 0. \tag{1.5}$$

This is synonymous to the existence of plane gravitational waves propagating at the speed of light. An example for a perturbation $h_{\mu\nu}$ assuming a wave moving along the z-axis is

$$h_{\mu\nu} = \begin{pmatrix} 0 & 0 & 0 & 0 \\ 0 & a & b & 0 \\ 0 & b & -a & 0 \\ 0 & 0 & 0 & 0 \end{pmatrix}. \tag{1.6}$$

This can be interpreted as the superposition of two different polarisations of the waves. One being the h_+ ("plus"-) polarisation for $a = 1$ and $b = 0$ and the other $h_\times$ ("cross") polarisation for the inverted case [7, ch.2, 3].

An illustration of the effect, that a gravitational wave has, is shown in figure 1.1.

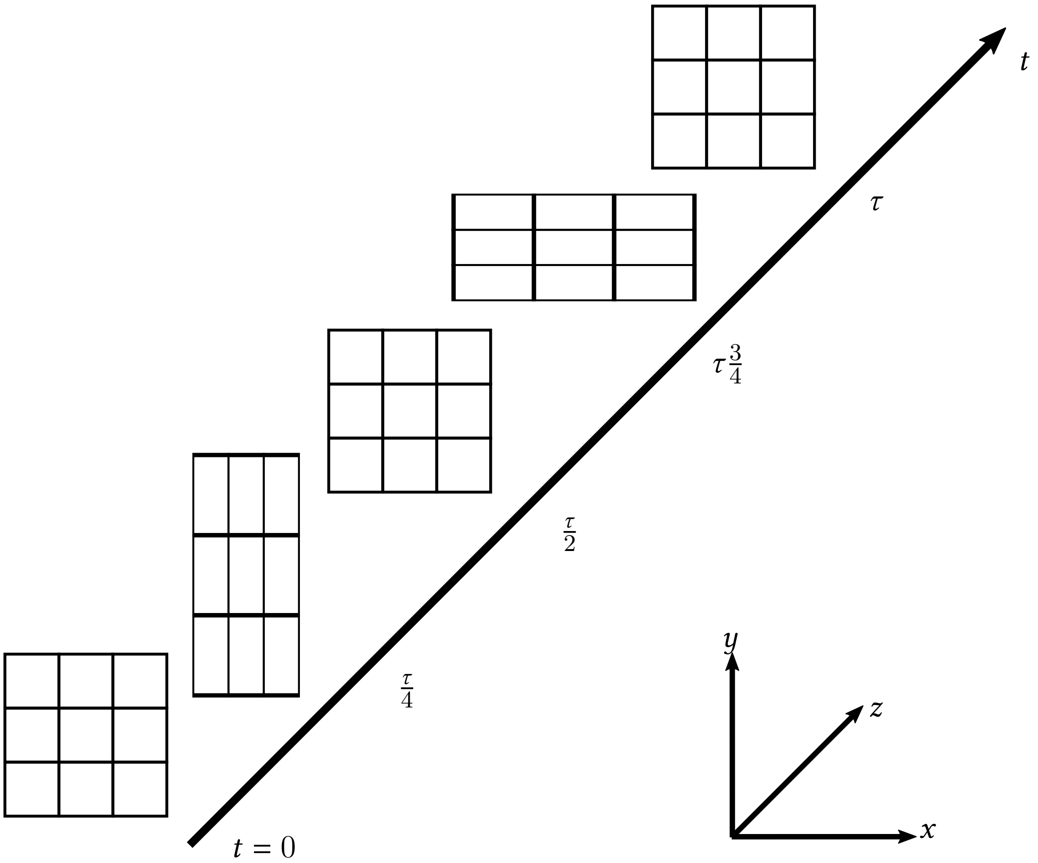

Figure 1.1: The temporal sequence of a gravitational wave in "+" polarisation. With passing time the wave deforms space-time. After a quarter period τ the x-dimension is compressed, while the y-dimension is elongated. At half period the deformation vanishes before being inverted. After three-quarter of the period the x-ax is elongated, while y is shortened. After the full period the effect is at zero again for both axes.

A rough estimation of the magnitude one can expect goes as follows: As an example we look for a binary system of two stars, whose masses are 1.4 $M_\odot$. This is the upper limit for white dwarfs, known as Chandrasekhar limit. These are circulating around each other with a distance $2r_0$ of 40 km at a distance R of 15 Mpc, our distance to the Virgo cluster. The strain is given by

$$|h| \approx \frac{r_{S1} r_{S2}}{r_0 R}, \tag{1.7}$$

where r_{Si} are the Schwarzschild radii of the two stars, r_0 is their distance to the mutual centre of gravity and R the observers distance. In our case this yields a relative length change of 1.9×10^{-21} [7].

This is equal to the diameter of a hydrogen atom compared to one astronomical unit. A gravitational wave detector (GWD) with the length of 10 km like the planned Einstein Telescope (ET) must still detect a length change of 10^{-17} m [15].

1.2 Einstein Telescope

The Einstein Telescope is a planned gravitational wave observatory (GWO) of the third generation with a triangular shape. The sensitivity will be improved by a factor of 10 and higher, depending on the frequency, compared to the design sensitivity of advanced LIGO, another GWO. As a consequence the Einstein Telescope will outperform the second generation GWOs in terms of event rate by a factor of $\mathcal{O}\left(10^3 - 10^5\right)$ for each source [19, 15].

To achieve these enhancements two ten kilometre long interferometers, which are optimised for different frequency ranges, are combined. One interferometer, operating at cryogenic temperatures to reduce thermal noise, is used for low frequencies (LF). This makes it necessary to use silicon instead of fused silica as mirror material. Thus the wavelength will be 1550 nm and not 1064 nm like in the high frequency (HF) interferometer. Also the light power in the arm resonators will be much smaller, with 18 kW compared to 3 MW. Thus the LF interferometer reaches its highest sensitivity in the frequency band between 9 Hz and 20 Hz. The second interferometer, planned to be operated at room temperature, is the most sensitive between 30 Hz and 1 kHz [15].

One interferometer is used for low frequencies (LF) and one for high frequencies (HF), which is described by the name ”xylophone configuration”[15]. Three of these pairs, each having an opening angle of 60 degrees, form one equilateral triangle. The desired strain

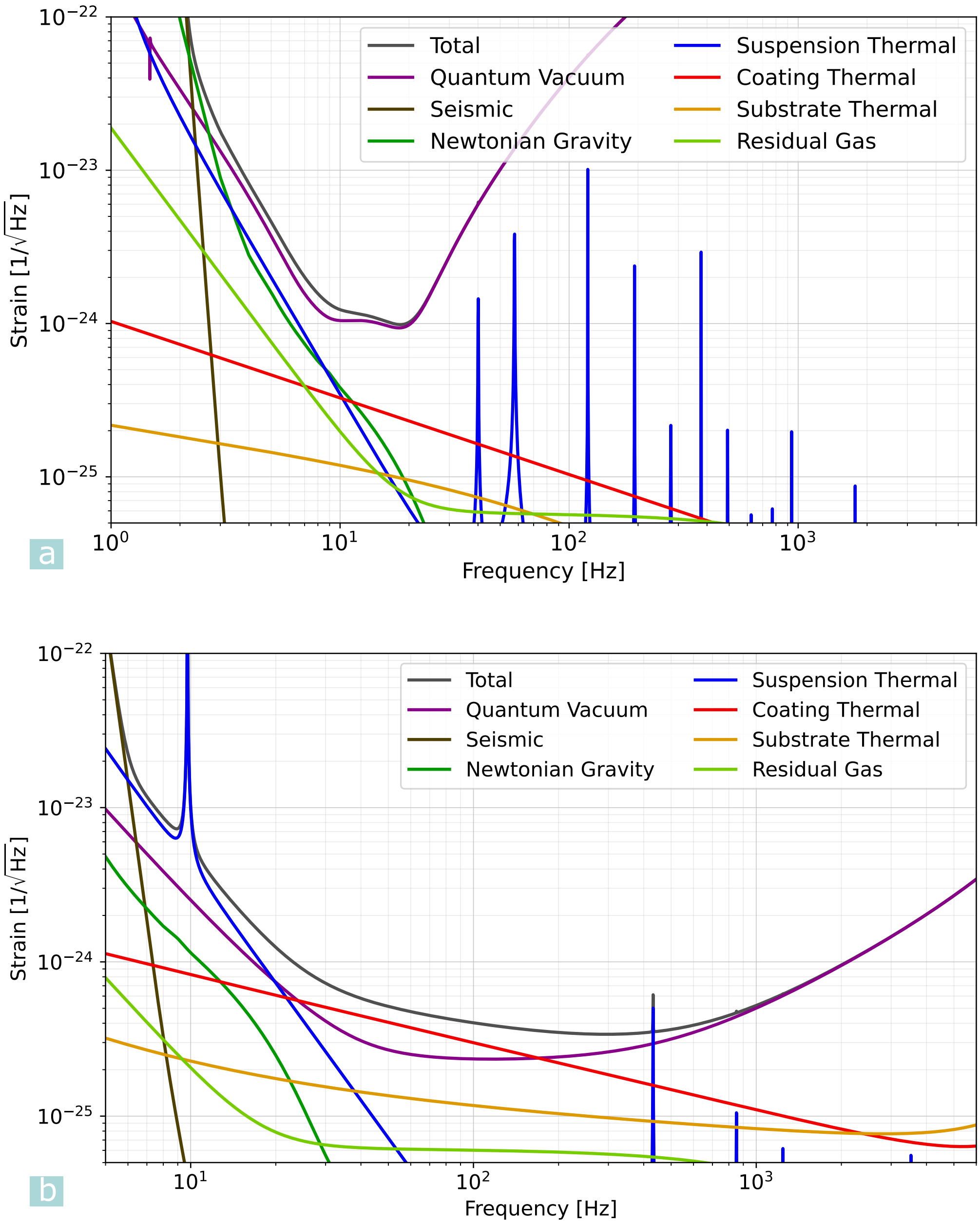

Figure 1.2: Noise budgets of the individual parts of the ET. The plots show the strain normalised amplitude spectral densities of various noise sources for a) the low frequency (LF) detector; b) the high frequency (HF) detector. The quantum noise is a critical limiting factor for the bandwidth, since it increases with frequency. The same is true for seismic noise, which increases towards smaller frequencies. Among other sources it is limiting the low frequency bandwidth. Thermal noise, especially coating thermal noise, limits the minimal detectable strain in the HF detector [16, 17, 18].

sensitivity is below 10^{-24} in the range of approximately 10 Hz to some kHz. This yet unreached sensibility is limited by several factors, visible in figure 1.2. In order to reach the desired precision, an individual consideration of the limiting factors is necessary.

Starting with the low frequency limit of the LF half, Newtonian as well as seismic noise are preventing higher sensitivities below 3 Hz. Above this the quantum noise limits the minimal strain, especially in the region of the highest sensitivity and above. The same is valid for the high frequency bandwidth limit of the HF interferometer, above 300 Hz. Below that down to 30 Hz coating thermal noise contributes more than quantum noise. The spectrum between 6 and 30 Hz is dominated by suspension thermal noise, otherwise the quantum noise is less then half an order of magnitude below it. Finally seismic noise is the limiting factor for frequencies under 6 Hz, for the HF system.

The quantum noise can be manipulated with the power inside the interferometer. To increase the light power each interferometer arm contains a resonator, also known as cavity. The chart 1.3 illustrates the resulting power build up. To bypass the drawbacks of increased power, like higher coating thermal noise, *squeezed light states* are necessary. These have a non-classical noise distribution, which can be used to suppress the detected quantum noise [20, 21]. The reduced relative shot noise of a higher optical power can be used, without actually using more light. Such a noise reduction by a factor of 10, realised by a squeezing factor of 10 dB, is thus planned from the beginning in the ET.

The Hamburg prototype is designed to test the combination of ET's high light power in the arm resonators (arm cavities) and squeezed light states of 10 dB. Using this prototype, it will be possible to investigate quantum noise, contrast, thermal effects and mode mismatch, limiting factors and noise sources for gravitational wave detection as well as new techniques for seismic noise suppression.

The following chapter 2 introduces the most important theoretical aspects of gravitational wave detection, which are necessary for this thesis. In chapter 3 the results of calculations and simulations of the prototypes reachable performance are presented. Chapter 4 is giving an overview about the experimental setup and the prototype itself.

The goal is to have masses floating in space-time free of any acceleration. For this reason the mirrors are also called test masses. I suspended the test masses with wire loops, since it is a passive method to suppress seismic distortions with a pendulum.

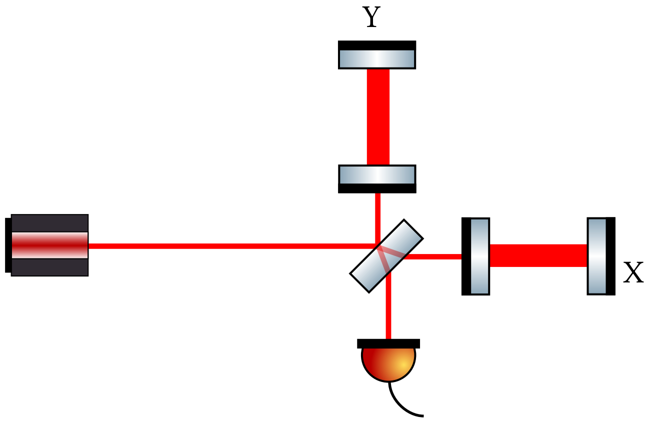

Figure 1.3: Schematic of a Michelson interferometer with arm cavities. This results in a higher circulating power and increased signal. In the X arm I reached a circulating light power of 1.8 kW and 0.4 kW in the Y arm, because of higher optical loss. This is explained in detail in chapter 7.2.

The measurement results of the alignment performance, using the test mass suspension, are explained in chapter 5. The current state of the experiments seismic isolation is presented in chapter 6.

Finally the results of the stabilised Michelson fringe and arm cavities are shown in chapter 7, ending with a conclusion of the thesis and an outlook on the future of the prototype in chapter 8.

2 Gravitational wave detection

This chapter contains explanations of the basics underlying the detection of gravitational waves. The majority of the information is taken from the book *Fundamentals of interferometric gravitational wave detectors* by P. Saulsen [7].

As explained in chapter 1.1 gravitational waves are plane waves. In the special theory of relativity the distance of two events, that are linked via the speed of light, is $ds = 0$, which follows directly from equation 1.1. Since gravitational waves propagate at the speed of light, we can use this property to detect them. For simplicity we choose the wave to propagate along the $z-$axis, so that it affects the $x - y-$plane.

There was already an experiment more than a century ago, that was carried out to measure difference in the movement of light depending on its direction. The Michelson-Morley experiment in the end of the 19^{th} century falsified the aether theory. They set up a light source and shone light onto a 50:50 beam splitter. The light beams were later back reflected to propagate on the same axis as the incoming light and interfere on the beam splitter. Depending on the runtime difference in the paths, which are also called arms, the interference pattern on the output varies. The output power is given by

$$P_{\text{out}} = P_{\text{in}} \cos^2 \left(k_x L_x - k_y L_y \right), \tag{2.1}$$

where L_i is the arm lengths of the optical paths and k_i are the wave vectors [22] [7]. Such an experiment structure, designed to measure differential arm length change is well suited for the detection of a wave, which stretches space in one direction, while shortening it in the perpendicular one. Thus we install a Michelson interferometer such, that one arm follows the x-axis and the other the y-axis [7]. For a gravitational wave passing the interferometer we can calculate the effect on the light beams, using the light-like property of the waves.

$$\begin{aligned} ds^2 = 0 &= g_{\mu\nu} dx^\mu dx^\nu \\ &= \left(\eta_{\mu\nu} + h_{\mu\nu}\right) dx^\mu dx^\nu \end{aligned} \tag{2.2}$$

Since the field equation becomes a wave equation in the TT-gauge coordinates, the elements of $h_{\mu\nu}$ can be written as $h\left(2\pi f t - \mathrm{k} \cdot \mathrm{x}\right)$, with $f = \frac{|\mathrm{k}|}{2\pi}$. Rearranging equation 2.2 using this and looking only at the x coordinates, we receive

$$c^2 dt^2 = 1 + h_{11}\left(2\pi f t - \mathrm{k} \cdot \mathrm{x}\right) dx^2. \tag{2.3}$$

This means, that the travel time from the beam splitter to the mirror is modulated with the perturbation h. The total round trip time from beam splitter to the mirror and back is calculated by integrating the square root of equation 2.3:

$$\begin{aligned} \int_0^{\tau_{out}} dt &= \frac{1}{c} \int_0^L \sqrt{1 + h_{11}} dx \\ &\approx \frac{1}{c} \int_0^L \left(1 + \frac{1}{2} h_{11}\left(2\pi f t - \mathrm{k} \cdot \mathrm{x}\right)\right) dx \\ \int_{\tau_{out}}^{\tau_{rt}} dt &= -\frac{1}{c} \int_L^0 \left(1 + \frac{1}{2} h_{11}\left(2\pi f t - \mathrm{k} \cdot \mathrm{x}\right)\right) dx. \end{aligned} \tag{2.4}$$

Summing both paths gives us

$$\tau_{rt} = \frac{2L}{c} + \frac{1}{2c} \int_0^L h_{11}\left(2\pi f t - \mathrm{k} \cdot \mathrm{x}\right) dx - \frac{1}{2c} \int_L^0 h_{11}\left(2\pi f t - \mathrm{k} \cdot \mathrm{x}\right) dx. \tag{2.5}$$

The equation for the y-arm is calculated equally with a dependency on h_{22} instead of h_{11}.

If the period of the gravitational wave is much bigger, than the time the light needs to make a round trip, the perturbation can be assumed as constant for any phase of the passing gravitational wave.

For cases in which this is not fulfilled a different approach is needed. As an example for $2\pi f_{gw} = \frac{1}{\tau_{rt0}}$ the light passing the interferometer arms experiences exactly one cycle of gravitational wave, where $\tau_{rt0} = \frac{2L}{c}$ is the round trip time for the unperturbated interferomter . This means the positive and negative perturbations cancel and no signal can be detected. This applies to all higher harmonics as well. For a more general description of τ_{rt}, we have to assume the perturbation is also time dependent and not constant $h(t) = h \exp\left(i2\pi f_{gw} t\right)$. Using this in equation 2.5 for both arms, we receive a phase difference of

$$\Delta\phi(t) = h(t)\tau_{rt0}\frac{2\pi c}{\lambda}\operatorname{sinc}\left(f_{gw}\tau_{rt0}\right) e^{i\pi f_{gw}\tau_{rt0}} \tag{2.6}$$

[7].

2.1 Angular dependency

The detection of the signal does not only depend on its frequency and the round trip time. The case of a gravitational wave propagating along the z-axis in + polarisation with $f_{gw} \ll 1/\tau_{rt}$ is ideal for a detector as described previously. But in reality the gravitational waves will pass the interferometer with arbitrary propagation vectors and a mixture of + and $\times$ polarisation. To describe the sensitivity of the detector depending on the waves propagation vector, an Euler transformation using three angles Φ, Θ and Ψ is necessary. The meaning of the angles is depicted in figure 2.1.

In the low frequency limit, the perturbation is modified to:

$$\begin{aligned} h_{11} =& h(t)\left[\cos 2\Phi\left(\cos^2\Psi - \sin^2\Psi\cos^2\Theta\right) - \sin 2\Phi\sin 2\Psi\cos\Theta\right] \\ h_{22} =& h(t)\left[\cos 2\Phi\left(\sin^2\Psi - \cos^2\Psi\cos^2\Theta\right) - \sin 2\Phi\sin 2\Psi\cos\Theta\right]. \end{aligned} \tag{2.7}$$

The ideal case is now given for $\Phi = n\frac{\pi}{2}$, $\Psi = n\pi$ and $\Theta = n\pi$. The generalised phase shift can be expressed as

$$\Delta\phi(t) = h(t)\tau_{rt0}\frac{2\pi c}{\lambda}\left(\frac{1}{2}\left(1+\cos^2\Theta\right)\cos 2\Phi\cos 2\Psi - \cos\Theta\sin 2\Phi\sin 2\Psi\right). \tag{2.8}$$

This equation gets down to zero for only four combinations of values. These are the points in the plane of detection, where both arms are disturbed equally. The simulated direction dependent sensitivity for the Hamburg prototype is shown in chapter 3.

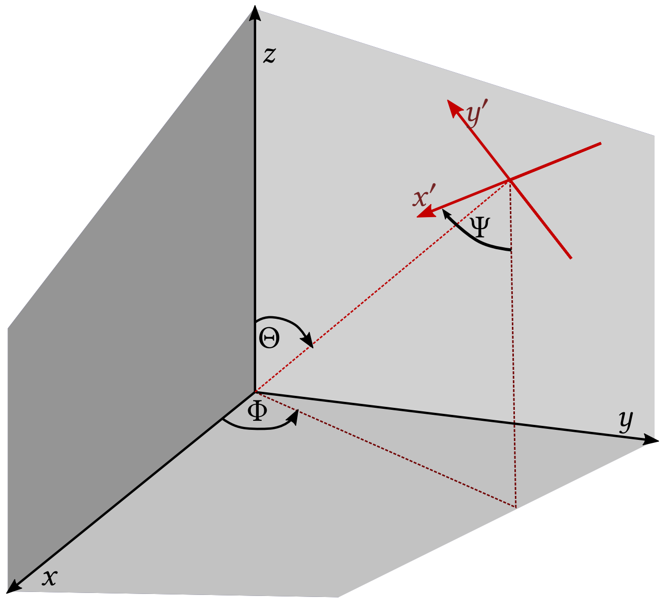

Figure 2.1: The coordination system is transformed to describe the gravitational waves propagation. The angles Φ, Θ and Ψ define the origin and polarisation with respect to the observers initial system.

2.2 Laser radiation

Modern gravitational wave detectors rely on highly monochromatic light sources with a small linewidth, to detect GWs precisely. The best sources for this radiation are lasers. This section gives a short summary about laser radiation. The details can be read in [23].

Laser radiation is a result of stimulated emission inside an optical cavity. The light is propagating in between two mirrors and amplified by external pumping.

There are different kinds of lasers. Continuous wave (cw) lasers emit light constantly, while pulse lasers emit light only for short timespans down to less then femtoseconds [24].

In a continuous wave resonator an active medium is constantly pumped, which causes the atoms in the crystal to excite into states of higher energy. This allows a passing photon to stimulate the emission of the stored energy as a photon similar to the first one. Phase, direction, polarisation and frequency are identical.

During this process a Gaussian beam forms and these underlay specific principles. The light is nearly monochromatic with a certain linewidth. The spatial intensity profile is

Gaussian (for the TEM_{00} mode), hence its name. Figure 2.2 depicts the minimal waist w_0, the waist radius $w(z)$ at any given z, the radius of curvature(ROC) $R(z)$ of the wavefront at point z, the opening angle ϕ and the Rayleigh length z_R. A beam can be defined with only the waist size, its position and the wavelength.

The other properties can be calculated from that, using the formulas

$$w(z) = w_0 \sqrt{1 + \left(\frac{\lambda z}{\pi w_0^2}\right)^2} \tag{2.9}$$

$$R(z) = z\left(1 + \left(\frac{\pi w_0^2}{\lambda z}\right)^2\right) \tag{2.10}$$

$$z_R = \frac{\pi w_0^2}{\lambda} \tag{2.11}$$

$$\phi = \arctan\left(\frac{z}{z_R}\right). \tag{2.12}$$

$$\tag{2.13}$$

The relation of these properties is depicted in figure 2.2.

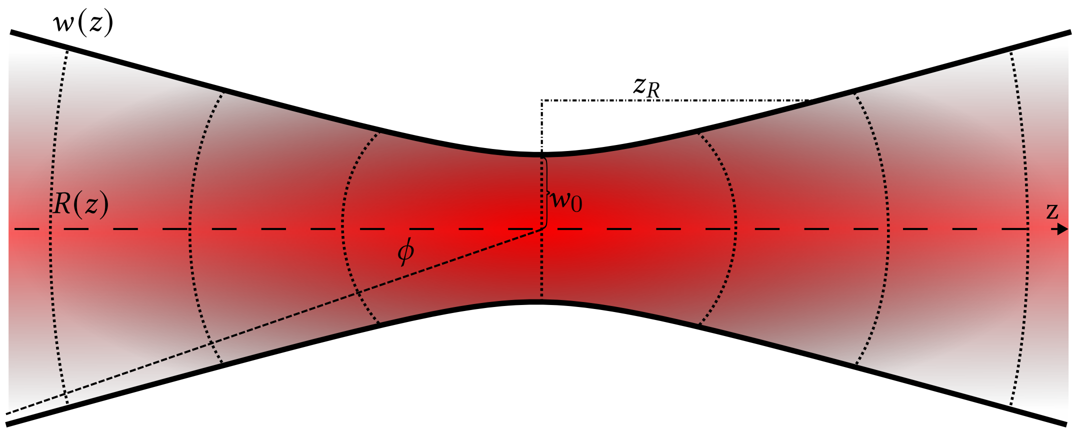

Figure 2.2: A Gaussian beam, w_0 is the minimal waist size, $w(z)$ the waist at position z, $R(z)$ the radius of curvature (ROC) of the wavefront at point z, ϕ the opening angle and z_R the Rayleigh length.

Laser beams also have other properties, that play a role in the experimental environment. Some of these are their *modes* and the polarisation. The polarisation is the time dependent orientation of the electrical field relative to its propagation axis. It can be linear, circular or elliptical. The modes give information about the transverse intensity profile. The most common modes are the Hermite-Gaussian (TEM) and Laguerre-Gaussian (LG) modes.

The experimental noise associated with lasers can be found in section 2.6.2.

2.3 Michelson interferometer

Michelson interferometers are named after Albert A. Michelson, who used one to determine if an ether is present. Nowadays it has become an instrument with a variety of applications, like refractive index measurements, surface measurements and spectroscopy [25, 26, 27]. The basic setup, shown in figure 2.3, consists of a light source with narrow linewidth, a beam splitter and two mirrors. The light shines on the beam splitter and is divided into equal parts onto different paths. The beams are reflected individually by mirrors and overlapped again on the beam splitter [22, 28, 7].

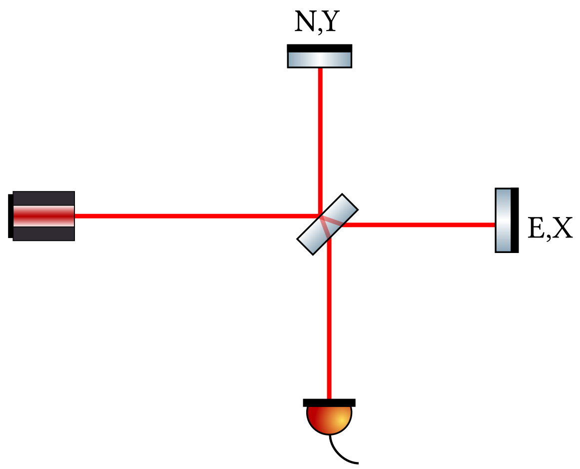

Figure 2.3: Schematic view of a Michaelson interferometer. The beam is split up by the beam splitter and reflected by the mirrors. The two beam paths between BS and mirrors are also called *arms* and as a convention in this thesis the transmitted arm is the *east* (E) arm or X arm, while the reflected beam is the *north* (N) arm or Y arm.

The length difference in the optical paths determines the interference of the beams on the beam splitter. Expressed in terms of light phase ϕ the transmitted power is given by

$$\bar{P}_{\text{out}}(\Delta\phi) = \sin^2\left(\frac{\Delta\phi}{2}\right)\bar{P}_{\text{in}} = \sin^2\left(\frac{\Delta L}{\lambda}2\pi\right)\bar{P}_{\text{in}} \tag{2.14}$$

[7]. The power, that is not transmitted, is reflected back towards the light source. This assumes a perfect contrast. The contrast of the Michelson interferometer is calculated with

$$K = \frac{P_{\text{max}} - P_{\text{min}}}{P_{\text{max}} + P_{\text{min}}}. \tag{2.15}$$

It is a dimensionless value between 0 and 1, but is usually given in %. P_{min} and P_{max} are measured at the in- or output, when ramping the optical phase. Using trigonometrical identities, equation 2.14 can be modified to contain the contrast as

$$\bar{P}_{\text{out}}(\Delta\phi) = \frac{1}{2}\left(1 - K\cos(\Delta\phi)\right). \tag{2.16}$$

For a maximal signal to noise ratio a low minimal power is necessary, which is connected to a good contrast. Thus a high contrast is mandatory for optimal measurements.

2.4 Fabry-Pérot cavities

The perturbations induced by a gravitational wave can be detected the best, when the length of the travelled light is comparable to the length of the wave. A ground based GWO can never fulfil this criterion for frequencies below the MHz range. To increase the travelled time, it is necessary to send the light back and forth the same path. Thus the round trip time is multiplied by the number of round trips to get the total travelled time. A set of (plane) mirrors, that are placed parallel to each other in a way, that the light can travel back and forth between them, is called a Fabry-Pérot cavity. In this the light propagates orthogonally to the planes of the mirrors and the interference of the overlapping beams is used to amplify the lightfield. A schematic is shown in figure 2.4.

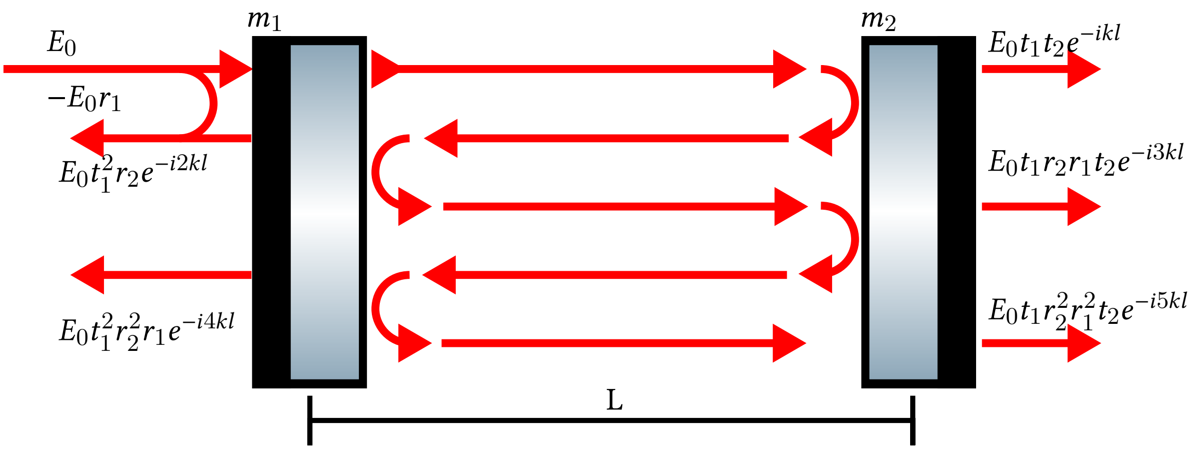

Figure 2.4: A scheme of a Fabry-Pérot cavity. The light reflects back and forth between two plane and parallel mirrors facing each other. The first few terms of the amplitudes of the light fields being reflected and transmitted are shown. The beams were separated in the depiction for easier understanding, but are in reality all on the same axis. Inspired by [7, fig.6.3], [29, fig. 3.2]

An important property of a cavity is its *finesse* $\mathcal{F}$. It gives information about the quality of the optical resonator, meaning how often the light is propagating back and forth and is the quotient of the free spectral range $\Delta\nu_{\mathrm{FSR}}$ and the cavities linewidth $\Delta\nu_{\mathrm{LW}}$.

$$\mathcal{F} = \frac{\pi\sqrt{r_1 r_2}}{1 - r_1 r_2} \tag{2.17}$$

$$\mathcal{F} = \frac{\Delta\nu_{\mathrm{FSR}}}{\Delta\nu_{\mathrm{LW}}} \tag{2.18}$$

$$\Delta\nu_{\mathrm{FSR}} = \frac{c_0}{2L} \tag{2.19}$$

In equation 2.19 L is the cavity length and $r_{1,2}$ in equation 2.17 are the amplitude reflectivities of the mirrors. Whereas $R_{1,2} = r_{1,2}^2$ are the power reflectivities of the mirrors.

To gain high powers in the cavity, a high finesse is required, which is equivalent to high reflectivities of the mirrors. The power inside the cavity can be calculated by modelling the amplitude of the fields A - H, defined by the equations 2.20 to 2.25. Figure 2.5 illustrates the meaning of these equations.

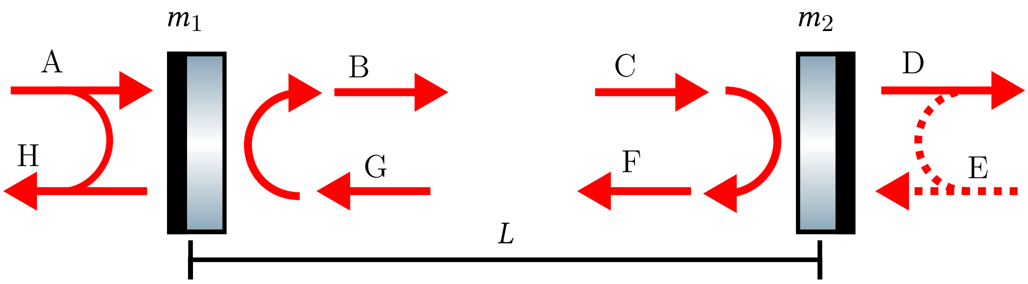

Figure 2.5: The lightfields in the cavity. A and E are sent into the cavity, while D and H are propagating away from it. B, C, G and F are the fields circulating in the cavity, being influenced by the length L and the loss η [30, chapter 3].

$$\mathrm{B} = t_1\mathrm{A} + r_1\mathrm{G} \tag{2.20}$$

$$\mathrm{C} = \mathrm{B}\eta e^{i\left(\omega\frac{L}{c_0}+\varphi\right)} \tag{2.21}$$

$$\mathrm{D} = t_2\mathrm{C} - r_2\mathrm{E} \tag{2.22}$$

$$\mathrm{F} = r_2\mathrm{C} + t_2\mathrm{E} \tag{2.23}$$

$$\mathrm{G} = \mathrm{F}\eta e^{i\left(\omega\frac{L}{c_0}+\varphi\right)} \tag{2.24}$$

$$\mathrm{H} = -r_1\mathrm{A} + t_1\mathrm{G} \tag{2.25}$$

With the reflectivities r_i for the fields and the corresponding transmissivities t_i being the square roots of their power related counterparts R_i, T_i. Or vice versa $r_i^2 = R_i, t_i^2 = T_i$.

Since there is no light coming from the back of the cavity, we set $\mathrm{E} = 0$. The loss factor η is defined like the transmission of the medium between the mirrors. A value of 1 thus means no loss, while a value of 0 represents absolute absorption. This gives us a power build up factor

$$\left(\frac{\mathrm{B}}{\mathrm{A}}\right)^2 = \frac{T_1}{(1-r_1r_2)^2} = \frac{1-R_1}{\left(1-r_1r_2\eta^2\right)^2}[30]. \tag{2.26}$$

Plane mirrors are hard to align perfectly parallel and even small distortions can result in an instability of the cavity. Thus often curved mirrors are used, that reflect the beam back, even if it should wander off a bit. The stability of a cavity is given by the criteria

$$0 < g_1 g_2 < 1, \tag{2.27}$$

where the parameters $g_{1,2}$ are defined as

$$g_i = 1 - \frac{L}{R_i}. \tag{2.28}$$

In equation 2.28 L is the length of the cavity, while R_i is the radius of curvature of mirror i [23, 31].

The measurements on the arm cavities I use in the experiment are presented in chapter 7.2 and their stabilisation in 7.3.

2.5 GWO read-out

The signal measuring can be influenced by the way the perturbation is detected. Behind the output of the Michelson interferometer a photo detector (PD) can detect the light leaving the interferometer. A local oscillator (LO) can increase the signal to noise ratio, thus a small amount of light is superposed with the signal beam before detection.

For a balanced homodyne detection the LO is split up in front of the interferometer and recombined behind the central BS. A phase shifter in the LO path allows to change the read-out quadrature easily. The combined light field is split up equally onto two PDs and measured, thus the term *balanced.* A downside of the homodyne readout is the necessity to carefully stabilise the LO path [19].

A way to stabilise the LO field is to take it directly from the light in the interferometer by adding a *dark-fringe offset* to create a DC readout. This on the other hand loses the advantage of choosing the read out quadrature.

The detection schemes can both be realised with the Hamburg prototype. The read-out optics behind the output of the interferometer are shown in chapter 4.3.

2.6 Noise sources

The sensitive interferometers react on any disturbance, that changes one arm length, with respect to the other. The length is changed, when the mirrors move, which is happing, when a mirror is accelerated by any force. Since the mirrors have a mass, which shall move in space-time free from any terrestrial influence, they are called test masses. They test if a force on their mass is present. The test masses shall be probes of the gravitational forces, that are not caused by anything on earth, but from far more away. This leads to the necessity to isolate them from all surrounding influences. Simulations on these can be made with the python package PyGWINC, the *Python Gravitational Wave Interferometer Noise Calculator*, which processes and plots different noise budgets for GWDs. According to such a simulation for the high frequency (HF) Einstein Telescope, visible in figure 2.6, the major noise sources limiting the sensitivity will be seismic noise, Newtonian noise, noise from gas molecules hitting the mirrors, thermal noise from the suspension and coating and quantum noise [18].

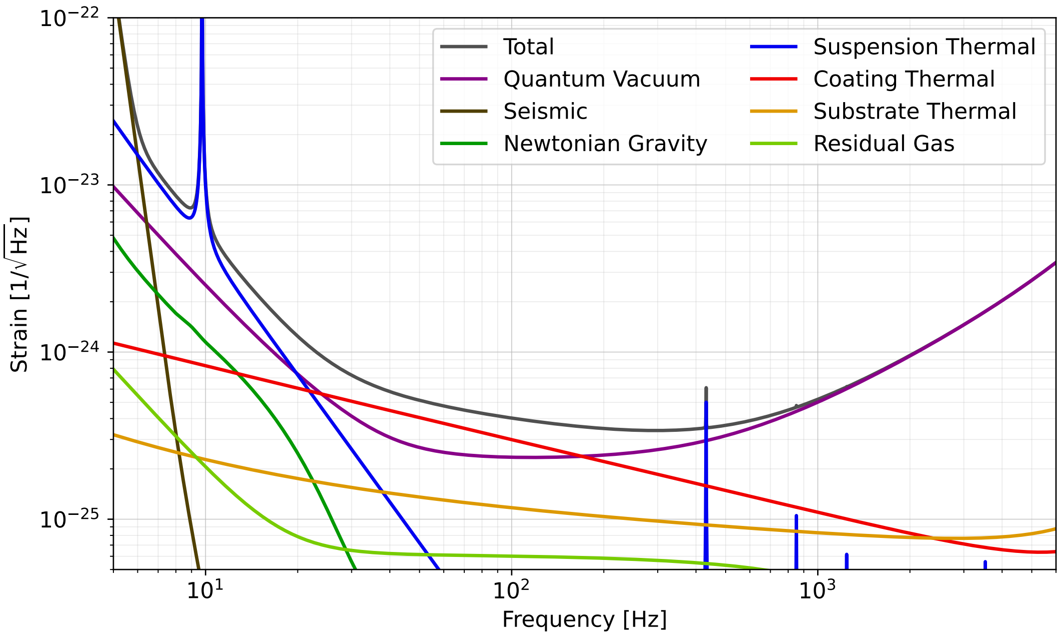

Figure 2.6: The expected strain sensitivity of the HF Einstein Telescope is limited by several noises over its frequency bandwidth. The major noise sources contributing are the seismic for low frequencies, suspension and coating thermal noise from a few up to some hundreds of Hertz, where quantum noise becomes the dominating noise source [16, 17, 18].

These various noises limit the frequency bandwidth, in which GWs can be measured. And since there are connections between noise sources, for example a higher light power

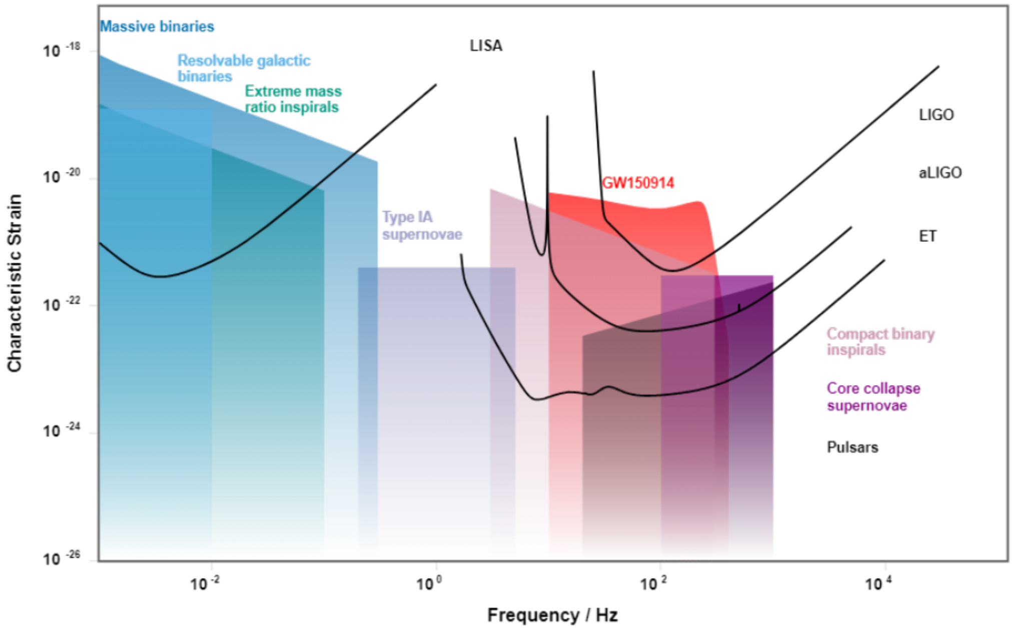

Figure 2.7: The characteristic strain of chosen gravitational wave sources and the sensitivity of chosen detectors in the frequency domain show, that future gravitational wave detectors must be more sensitive to smaller frequencies, in order to detect gravitational waves from type 1A supernovae, galactic binaries and other sources [32].

can reduce the shot noise, a part of the quantum noise, but will increase thermal noise, an optimal configuration for each frequency band must be chosen. In other words different configurations are needed for different frequencies. The thought of each frequency band having its own detector was the origin of the name *xylophone configuration.*

As the graphs in figure 2.7 show, the frequencies below 10 Hz can yet barely be detected with a reasonable sensitivity, even though there are expected sources [32]. Thus there is an interest in pushing the limits to a low frequency detector.

Since for smaller frequencies the thermal noise rises, like shown in the graphs of figure 2.6, it becomes important to cool the test masses and suspensions. This led to the design of a cryogenic low frequency interferometer, while a second room-temperature high frequency interferometer operates simultaneously. The cryogenic system itself makes major changes necessary, like silicon as a mirror material, which has the needed cryogenic properties. It is not transparent for 1064 nm and thus the wavelength must be changed to 1550 nm. The power in the arm cavities must be adjusted and a higher damping of seismic noise is needed.

The ladder is a serious issue, since even the *superattenuator*, used by the GWD Virgo, is not sufficient as isolation for the LF interferometer. The movement transferred to the mirrors by seismic noise is also disturbing the measurements and thus makes a seismic isolation necessary. The *superattenuator* uses six stages of pendulums combined with cantilever springs and an inverted pendulum in a 10 m structure. The needed improvements for LF ET result in an even larger structure and thus more effort to cool the system [33, 15].

A requirement needed not only for the installation of cryogenic cooling structures, but for gravitational wave detection in general, is a vacuum, since it eliminates noise caused by the air molecules and also reduces laser noise by pressure fluctuations in air.

In gravitational wave detectors thermal noise is a limiting factor in various ways. Temperature is a measure of the velocity atoms have and this movement is causing a variety of noise sources. It will not be further investigated in this thesis, but interested people can read more about in [7, 34, 35, 36, 37, 38].

A noise, that can not be isolated against, is Newtonian noise. It is created by changes in earths gravitational field. This can for example be caused by density changes in air or in ground close to the detector. Since this is a direct gravitational coupling between the test masses and the surroundings, it can not be shielded. Some sorts of seismic waves or human activity in the surrounding area are exemplary sources of these perturbations. To reduce the effect of surface waves, the detector site can be built underground and in seismically quite areas. Additionally models of gravitational coupling together with seismic data can be used to subtract the distortions in the post processing of the data stream. [39, 40, 15, 41].

Another noise source is quantum noise, which originates in the quantum nature of light. The interaction between the photons and mirrors, as well as the detection of the photons are processes underlying fluctuations, which are further explained in section 2.6.2 [42, 43].

2.6.1 Seismic isolation

The distortions caused by seismic movement are a limiting factor to today's and future gravitational wave detectors, as seen in figure 2.6. For low frequencies, in the region of a few Hertz and below, it is the dominant noise source preventing higher sensitivities. To suppress this noise, a series of measures can be taken.

Starting with passive systems, such as dampers, to isolate the experiment from its environment. The information and equations are taken from [7]. The equation of motion for a mass m attached to a spring with spring constant k is given by

$$m\ddot{x} = -k\left(x - x_0\right), \tag{2.29}$$

where x is the position of the mass and x_0 is the undisturbed position. We ignore internal damping and the mass of the spring here. This system has a resonance frequency given by

$$f_0 = \frac{1}{2\pi}\sqrt{\frac{k}{m}} \tag{2.30}$$

and its behaviour in the frequency space is described with its transfer function

$$\frac{x}{x_0} = \frac{f_0^2}{f_0^2 - f^2}. \tag{2.31}$$

From this we can derive, that for frequencies much smaller than f_0 the spring has roughly no damping effect. On the other side of the resonance the behaviour is

$$\frac{x}{x_0} \overset{f \gg f_0}{\propto} \frac{f_0}{f^2}. \tag{2.32}$$

When N masses are cascaded with springs, that have the same resonance frequency for each mass spring pair, the answer of the N-th mass is given by

$$\frac{x_N}{x_0} \overset{f \gg f_0}{\propto} \left(\frac{f_0}{f}\right)^{2N}. \tag{2.33}$$

Concluding, high frequencies can be well suppressed, using springs or spring-like dampers. This is visualised in figure 2.8.

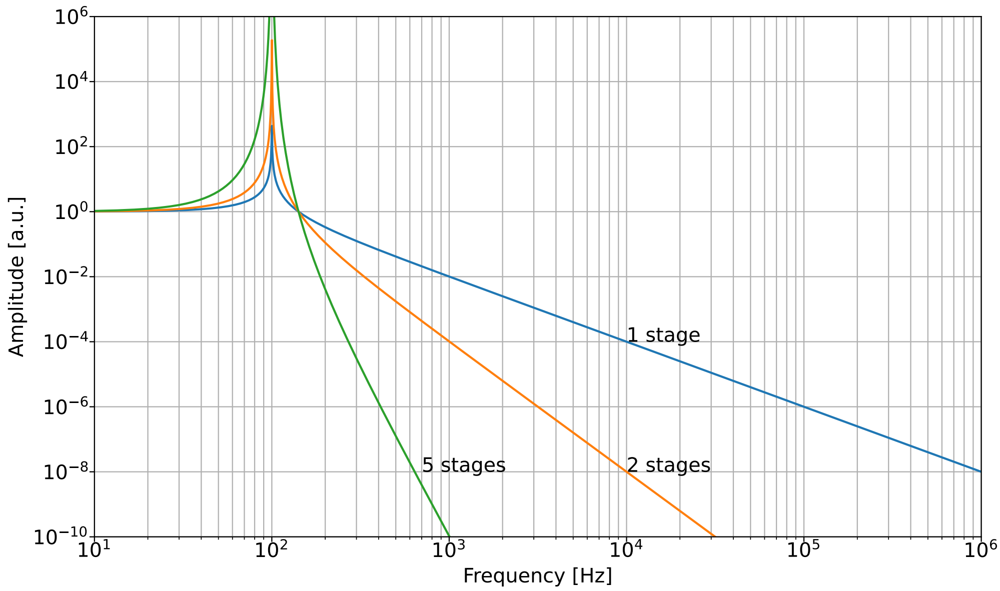

Figure 2.8: The systems response of cascaded springs and masses without damping. The three traces belong to systems with one, two and five stages, each stage containing one spring and one mass with a resonance frequency of 100 Hz. The answer of the system drops rapidly with increasing frequency beyond the resonance and each stage improves the damping.

The isolation, using a pendulum, gives comparable results.

At least for horizontal isolation the transfer function follows the equation 2.33 seen for vibration isolation with springs, if we assume N cascaded pendulums. The vertical isolation of a pendulum is worse by a factor of $\left(f_{0,\mathrm{vert}}/f_{0,\mathrm{horiz}}\right)^2$ for each stage. The vertical resonance frequency is usually significantly higher, so that additional vertical isolation is advisable. This can be done by a combination of vibration isolation with springs or dampers for vertical isolation and a suspended test mass. The seismic isolation used for this experiment is explained and characterised in chapter 6.

A possible expansion of these methods is active control, using sensors to measure the movement or position and to counteract it with actors or motors. These regulation loops are described in chapter 2.7.

2.6.2 Laser noise

The lasers used for GW detection need to be as monochromatic as possible. Mathematically that would require an infinitely long beam, but a single-mode continuous wave (cw) beam in operation can be assumed to be sufficiently monochromatic. Ideally the amplitude and frequency remain constant at all times, but in reality there is always noise. Some of the most common noises are:

phase noise Variations in the phase of the light field. Origins of phase noise can be spontaneous emission in the gain medium into the resonator mode, quantum noise, optical loss and technical noise, like vibrations of the laser resonator or noise of the pump source. Phase noise leads to a finite linewidth [44, 45].

frequency noise Random fluctuations in the frequency, which is the derivative of the phase. Thus the frequency noise is directly related to the phase noise. More precise their power spectral densities are proportional to each other [46].

amplitude noise Changes in the optical power. More often also referred to as (relative) intensity noise. Quantum fluctuations and technical noise create variations in the power of the output field [47].

quantum noise Quantum noise has its origin in the quantisation of light. Even though light underlays the wave-particle dualism the photons are interacting with the detectors and mirror surfaces as if they were particles in the instant moment of interaction. Over time the amount of photons hitting a surface is statistically distributed and thus deviates over time. This introduces shot noise and radiation pressure noise [48].

shot noise The shot noise is a boundary to the intensity noise and a property of the light field itself. Its level for an interferometer with $\mathcal{N}$ times folded arms can be calculated, using the formula

$$h_{SN} = \frac{1}{L\mathcal{N}}\sqrt{\frac{\lambda hc}{2\pi^2 P_{\text{in}}}} \tag{2.34}$$

and is crucial part of the high frequency noise limits for GWOs. It can be suppressed, using squeezed light states. The round trips can be calculated, using $\mathcal{N} = 2\mathcal{F}/\pi$ [7, 49].

radiation pressure noise The reflection on a mirror surface causes a back-action equal to twice the photons momentum, known as radiation pressure. The optical power of the laser is measured as a mean average over time, but on a quantum scale the back action of a statistically distributed number of photons hitting the mirrors per unit time causes changes in the position of the mirrors surface, which is referred to as radiation pressure noise [50].

[45, 51]

The amplitude and phase noise were analysed during this thesis and the results are shown in chapter 7.3. The quantum noise is an important part of the simulations done in chapter 3.

2.7 Feedback control

Experiments tend to be dynamic systems. This dynamic itself can be the interest of observation, but can also be something that needs to be controlled and regulated. These control loops are used in the experiment in the stabilised Michelson fringe (chapter 7), the arm cavities (chapter 7.3) and the seismic isolation (chapter 6). The terms are taken from [52].

The working principle of a regulated system is:

1. Measure control variable $y(t)$.

2. Comparing control variable and reference variable $w(t)$ delivers control deviation $e(t) = w(t) - y(t)$.

3. In the control device the control deviation is converted to the regulating variable $u(t)$ with respect to the control systems dynamic behaviour, which is fed into the control system.

4. The regulation and a possible distortion $d(t)$ act on the control system, which leads to a new value of the control variable.

There can also be constraints, for example a requirement, that there are no oscillations in the system, which must be taken into account, when designing the control device. A controller usually consists of several stages to shape the signal. Commonly used are the following stages:

Proportional: the bigger the difference between reference variable (=set point) and control variable, the bigger the regulating variable. It is a linear gain stage.

Integrator: the past of the current state is important for the current regulation variable value. This prevents a lasting offset between regulation and reference variable.

Differentiator: Instead of the absolute value of the control deviation, its gradient determines the value of the regulating variable.

[52]

To improve the design the transfer function of an existing controller is measured and analysed. Afterwards the different stages are adjusted to improve the regulation loop. This includes addition of filters for example. When the system is regulated actively, using the feedback, we speak of a *closed loop*, while a lack of feedback is called *open loop* operation.

2.7.1 Pound-Drever-Hall technique

There is a method to stabilise a lasers frequency to an external cavity, named after the physicists Pound, Drever and Hall, that worked on this topic. The setup is shown in figure 2.9. The laser is sent through an electro optic modulator (EOM), which imprints sidebands on the beam. Their frequency is outside of the cavity linewidth. Between the modulator and the cavity a polarizing beam splitter (PBS) and a quarter-wave plate form an optical isolator, so that the light back reflected from the cavity can be measured with a detector. The cavity itself consists of two mirrors facing each other. The detected signal is filtered and electronically mixed with the modulation frequency, which delivers an error signal. A servo transforms it to a feedback signal for the laser [53]. The implementation and the way we use this method to lock our laser onto the arm cavities is further explained in chapter 7.3.

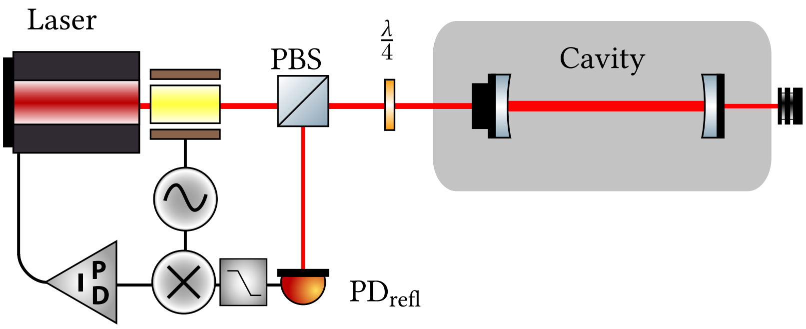

Figure 2.9: A scheme of the Pound-Drever-Hall laser stabilisation. The laser beam is passing an EOM, a PBS and a quarter-wave plate before entering the cavity. The EOM imprints sidebands on the beam. The additional optics form an optical isolator, so that the light reflected from the cavity is guided towards a resonant photo detector (RPD). The signal is demodulated in the resonant circuit to provide an error signal to a controller. This allows to keep the cavity on (anti-) resonance, by tuning the lasers wavelength. This procedure reduces noise and drifts of the wavelength, if the reference cavity is reliably stable[53].

3 Simulation of the quantum noise limited sensitivity anisotropy

To make an estimation of how good the prototype will be able to perform, if everything works perfectly, I calculated and simulated some facts and figures to compare the ET HF design values to the prototype. Using the following parameters,

	ET HF [15]	Hamburg prototype
Length	10 km	0.91 m
λ	1064 nm	1550 nm
P_{in}	500 W	7.75 W
$P_{\mathrm{circulating}}$	3 MW	4.7 kW

Table 3.1: Parameter for ET HF and the Hamburg prototype

and equation 2.34 the sensitivity limit given by the shot noise is $5.5 \times 10^{-20}\,\frac{1}{\sqrt{\mathrm{Hz}}}$ for the prototype in my experiment. With help of Dr. M. Korobko, who provided the necessary MATHEMATICA code, we made a more detailed simulation with the same parameters. This program considers the originating direction and polarisation of the wave, masses of the mirrors, the cavity tunings and reflectivities. The result is plotted in figure 3.1.

According to this simulation, the minimal strain, that this configuration could detect, is from 100 to 100 kHz about $4 \times 10^{-20}\,\frac{1}{\sqrt{\mathrm{Hz}}}$. The cross, plus and mixed polarisation curves assume the best possible angle for a detection, while the simulation for a vertical incident assumes a wave in plus polarisation. The minimal values for the plus, cross and mixed polarisation are in order $5.4 \times 10^{-20}\,\frac{1}{\sqrt{\mathrm{Hz}}}$, $5.3 \times 10^{-20}\,\frac{1}{\sqrt{\mathrm{Hz}}}$ and $7.5 \times 10^{-20}\,\frac{1}{\sqrt{\mathrm{Hz}}}$. Around multiples of the FSR the strain sensitivity drops significantly. It depends only slightly on the polarisation, assuming the wave comes from a direction, where the given polarisation can be measured optimally.

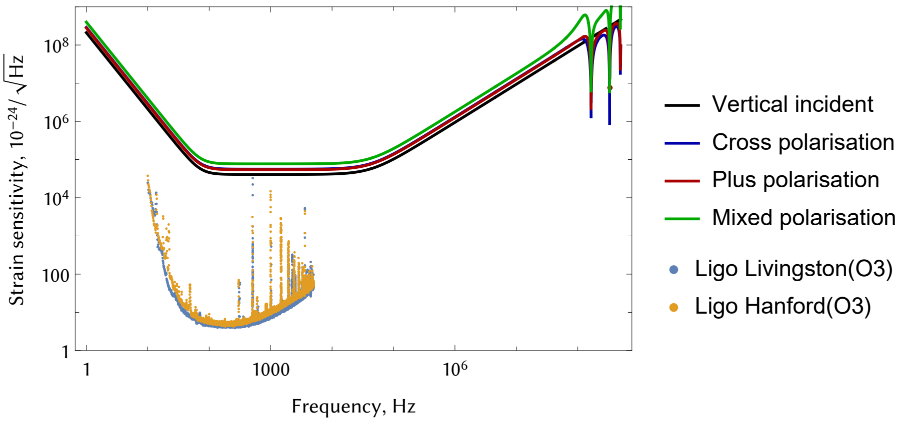

Figure 3.1: Simulated one sided spectral density strain sensitivity between 1 Hz and the first FSRs for different polarisations, using the code kindly provided by Dr. Mikhail Korobko, adapted with the parameters for the Hamburg prototype and data from the LSC [54]. The minimal strain detectable is on the order of $5 \times 10^{-20}\,\frac{1}{\sqrt{\text{Hz}}}$ between 100 and 1×10^5 Hz. After rising, the detectable strain drops by several orders of magnitude around multiples of the FSR. The cross, plus and mixed polarisation curves assume the best possible angle for a detection, while the vertical incident graph assumes a vertical input in plus polarisation.

The minimum given by equation 2.34 and the simulation verify each other, which means in theory the sensitivity is limited by shot noise. This means adding squeezed light states would improve it. Even without them the prototype can reach a strain sensitivity shot noise level in the order of $10^{-20}\,\frac{1}{\sqrt{\text{Hz}}}$.

The higher sensing sensitivity around the FSRs allows to estimate how strong undetected GWs in this frequency region could be maximally. Even though there are no sources expected to cause GWs above 1 kHz, not to mention above 100 MHz, we could still measure and verify the expectations down to the reached strain. If we compare these curves to the sensitivity of advanced LIGO's third observation run, it is apparent, that aLIGO is much more sensitive in low frequency regions. In the spectrum above 10 kHz there is no reliable data to be found about aLIGO's sensitivity, but extrapolating the existing data, it becomes reasonable, that both sensitivities do not deviate much at multiples of the free spectral range frequency. At the first FSR the strain sensitivity drops to $\approx 3 \times 10^{-21} \frac{1}{\sqrt{\mathrm{Hz}}}$. In other words this setup could measure high frequency GWs comparably well as aLIGO for certain high frequencies.

3.1 Sensitivity anisotropy

As already mentioned in other chapters, the gravitational waves have a polarisation. The direction of their effects defines how well they can be measured. Under certain conditions the detection is not possible at all, no matter how strong the wave would be. This dependency on the direction, or anisotropy, is also called the antenna pattern, since the gravitational wave detectors are antennas for gravitational radiation.

3.2 Low frequency approximation

For L-shaped detectors, meaning they have two arms with a 90° angle between them, the antenna pattern is shown in figure 3.2. These are patterns under the condition, that the frequency of the gravitational wave is much lower, than the inverse of the round trip time in the arm. I plotted three different cases with the help of my colleague Dr. Mikhail Korobko, who provided the code. The + and $\times$ polarisation have different antenna patterns, where one feature is the shifting of the longitudinal dependency by $\pi/4$, which is equivalent to the 45° shift between the polarisations. An additional difference is, that the $\times$ polarisation also can not be detected, when its propagation vector lies in the detection plane. The reason is simply, that these waves will always act on both arms equally. The figure 3.2c can be interpreted as renormalised average, that shows for which propagation directions the observatory is not sensitive regardless which polarisation the wave has. For all cases an axial symmetry for latitude and longitude is observable. For the latitude this is also valid for a shift by $n\pi/2$ and for the longitude by $n\pi/4$.

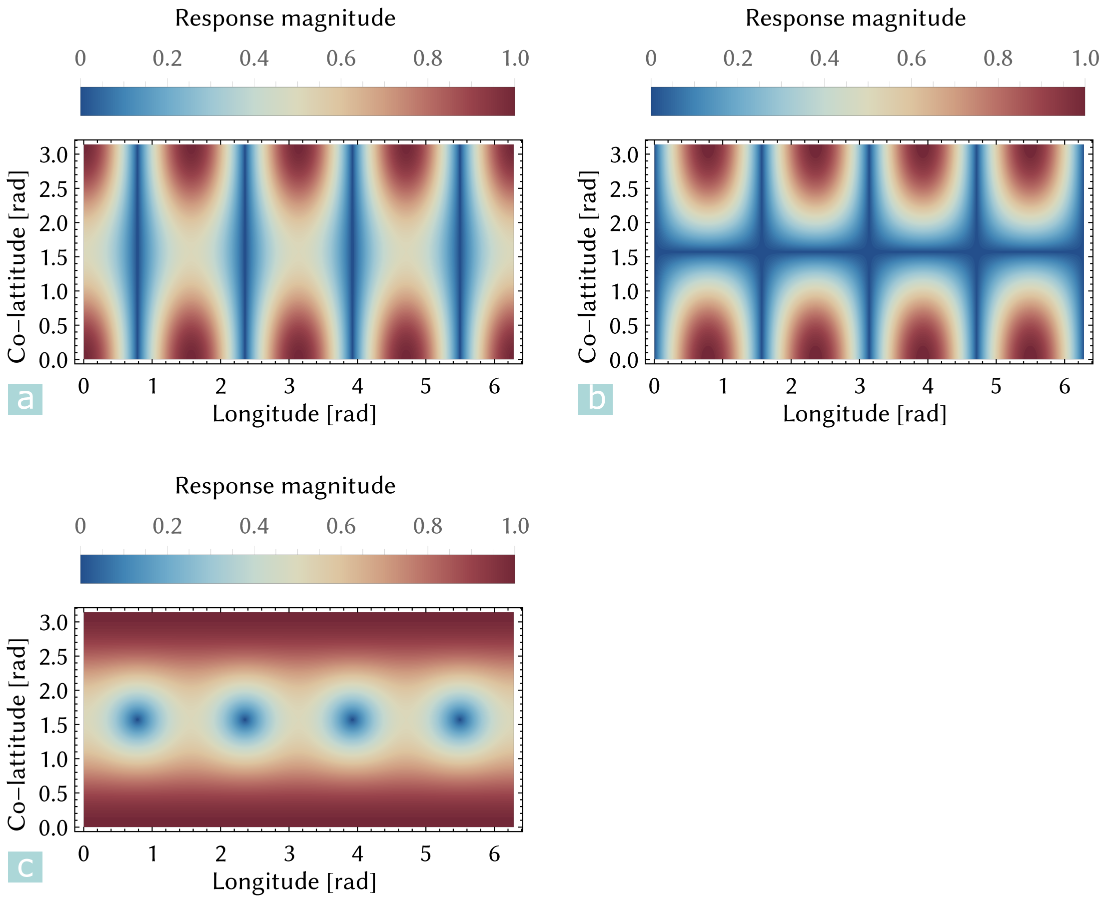

Figure 3.2: The antenna patterns for the ET prototype for different polarisations at frequencies much lower than the FSR. The maximum of sensitivity is given for waves propagating along the normal vector of the detection plane. The type of polarisation defines at which coordinates the sensitivity vanishes. a) Plus polarisation: the sensitivity reaches zero, when the value of the longitude Φ is equal to odd multiples of $\pi/4$. This is when the wave influences both arms in the same way, so that the effects cancel on the beam splitter. b) Cross polarisation: the detector is not sensitive for waves, when they arrive from longitudes multiples to $\pi/2$ or from $\Theta = \pi/2$. c) For a mixed polarisation the only spots, where a gravitational wave can not be detected, are on the $\Theta = \pi/2$ line, when the longitude is an odd multiple of $\pi/4$. These are geometrically the diagonal lines between and around the interferometer arms. The code for the simulation was provided by Dr. Mikhail Korobko.

3.3 Sensitivity at one FSR of the arm resonator

Gravitational waves, that have much higher frequencies, have additional effects on the antenna pattern. In this case the effect of the wave can not be approximated as constant for the round trip time of the light in the arms, but must be treated as a time dependent phenomenon, as stated in equation 2.6. The gravitational wave therefore can have an effect on the light on its way to the end mirror and an opposing effect on its way back, resulting in no signal on the beam splitter. This is shown in figure 3.3, where now in 3.3b the latitudes around zero and π show no sensitivity anymore. In general the sensitivity drops to smaller values for this case at a frequency of one FSR, which for the ET prototype is around 164 MHz.

Now the pattern for the plus polarisation is less symmetric in the longitude, or at least the periodicity doubled. Instead of a symmetry every $\pi/4$, now the values are symmetric to $\pi/4 + n\pi/2$.

Summarizing the results the prototype can reach a sensitivity of $5 \times 10^{-20} \frac{1}{\sqrt{\mathrm{Hz}}}$ and also comparably high sensitivities around multiples of the FSR.

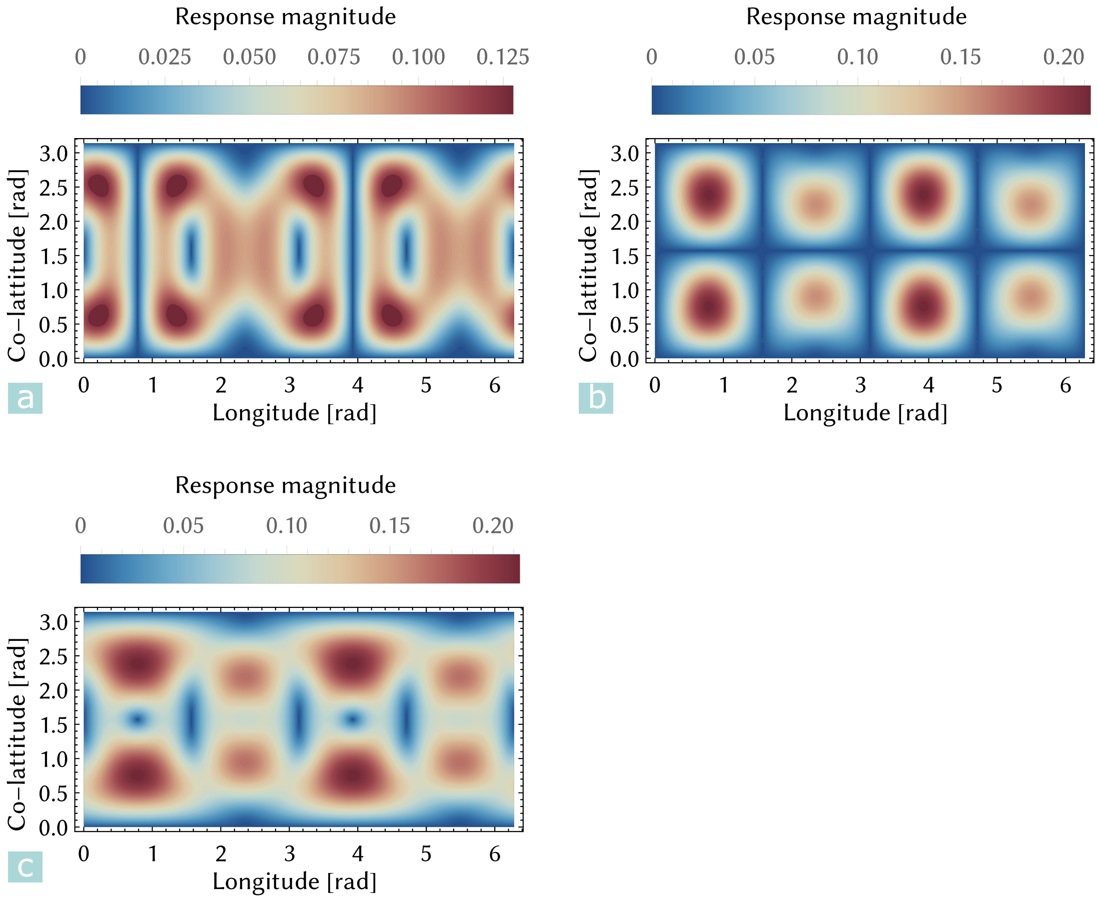

Figure 3.3: The antenna patterns for the ET prototype for different polarisations at the frequency of one FSR. a) plus polarisation; b) cross polarisation; c) mixed polarisation. Unlike for low frequency waves the sensitivity is not optimal any more for waves moving perpendicular to the plane, but for ones that propagate under an angle towards the detector. The patterns are more complex and also the response magnitude decreased compared to the low frequency ones, but some features remain similar. The code for the simulation was provided by my colleague Dr. Mikhail Korobko.

4 Overview of the optical system

In this chapter, the design of the Hamburg ET prototype is described. The optical setup from laser to the interferometer is explained in section 4.1, the interferometer itself in 4.2. The section 4.3 contains information about optics behind the interferometer, needed to adjust the arm cavities and measure the signal. Experimental results regarding the arm cavities, contrast and regulation loops are shown in chapter 7.

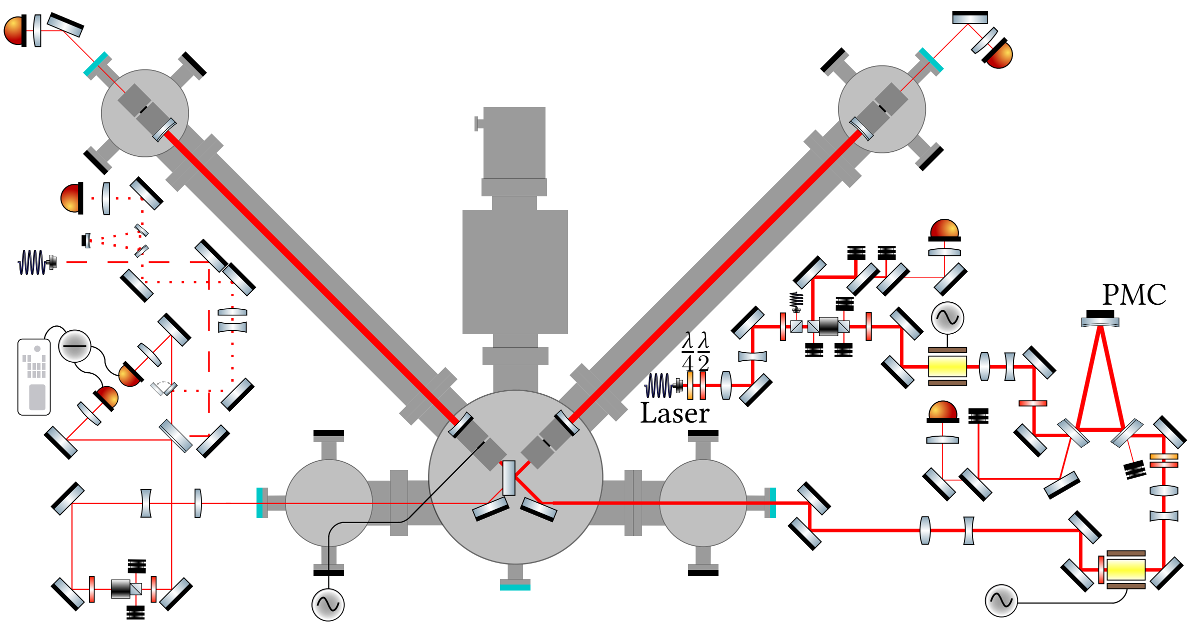

Figure 4.1: The optical setup of the prototype. The dashed line is the path of the LO. The dotted path is an alternative path to the diagnostic cavity.

4.1 Laser beam preparation

Figure 4.1 shows the setup of the experiment with all optical elements. The light is provided by a 1550 nm NKT laser system, with a maximum output power of 8.5 W. The wavelength in the ET is planned to be 1064 nm, but this difference has no effect for the purpose of the prototype and of the available laser systems the used one provided the highest power. The fiber outcoupler produces a beam collimated at its output with a waist radius of 2.6 mm. The beam is send through a quarter- and a half-wave plate to adjust the polarisation. A polarizing beam splitter (PBS) behind allows to split off a variable amount of light towards a fibre, which will be needed for the squeezer and local oscillator (LO) fields in the future. This part is not shown in the picture. The squeeze laser for shot noise reduction was build by Pascal Gewecke and provides a noise reduction of more than 10 dB [55].

Afterwards, a lens set and a set of two mirrors guide the beam through a Faraday isolator (FI). Two half-wave plates in front and behind it regulate the polarisation. In front of the FI it must be parallel to the plane of the propagation (p-polarisation). The light leaves with a polarisation tilted by 45° and is brought to s-polarisation, for which the mirrors are optimised.

Another mirror set maneuvers the beam through an electro optic modulator (EOM), which imprints 45.66 MHz sidebands onto the laser. The EOM is followed by a lens set, a mirror set and a half-wave plate to match the beam to the pre-mode cleaner (PMC). The PMC is a triangular cavity, consisting of two partially transmissive and one high reflective mirror, which filters beam modes. While the eigenmode is transmitted, unmatched light is reflected. A stable output of a single mode can be achieved using a control loop. The highly reflective mirror is mounted on a piezo, so that the length of the cavity can be actuated. The control signal is achieved, using the modulated light field.

In reflection from the PMC the beam is attenuated and steered onto a resonant photo detector (RPD). This detector is also supplied with a 45.66 MHz modulation of which the phase in respect to the EOM modulation can be adjusted. The light signal is multiplied with the modulation and afterwards lowpass filtered, resulting in the error signal.

Using a PID controller and a high voltage (HV) amplifier, the signal is fed back to the piezo to form a regulation loop, also called a *lock*. The locking scheme is described in detail in the masters thesis of Maximilian Faden [56], on which he worked under my guidance.

In transmission of the PMC another set of mirrors, a set of lenses and a set of quarter- and half-wave plate are placed. These are used to navigate the laser through a second EOM, which is necessary for the arm cavities.

The second EOM imprints a modulation of 163.97 MHz, which is right between the FSRs of the arm cavities. This is further explained in chapter 7.3.

A final lens set and two mirror sets are placed behind it to match the beam to the interferometer and the arm cavities. The coated window to the vacuum chamber marks the beginning of the interferometer, which is described in the following section. At this point the maximum power, that enters the interferometer is measured to be 7.75 W. An error value can be estimated, using observation of drifts in the power to be 0.1 W.

4.2 Interferometer design

Inside the vacuum chamber, a two inch mirror steers the beam onto the central beam splitter (BS), which provides the two beams for the interferometer. Behind the BS, the input test masses are placed in their suspension structures. The end test masses follow after about 0.91 m of propagation. Using the *Linear Cavity Calculator*, programmed by S. Steinlechner, the TEM_{00} mode for this cavity has with a minimal waist radius of 380 μm at a position about 6 mm behind the input mirror [57].

The experimental results with the measurement of the finesse, mirror reflectivities and other figures are described in chapter 7.2.

In the future, the prototype will be expanded, using a power recycling mirror (PR) and a resonant signal extraction mirror (RSE), which will be placed in front (PR) and behind the central beam splitter (RSE) to improve the signal to noise ratio. They are not part of this thesis, but the space in the side chambers needed for them is thus kept empty.

4.3 Output optics

The optics behind the interferometer will become more important in the future of the prototype, when the squeezing source will be implemented. To prepare for this phase, I guided the signal path through a Faraday rotator - PBS combination, which will allow the incoupling of the squeezed light. Behind that a 50:50 BS is set up in front of a homodyne detector, to allow a balanced homodyne detection. A separate path for the LO leads to the remaining port of the BS. Additionally, a removable mirror leads the light towards a diagnostic cavity, similar to the mode cleaners, to align and match all beams to one another.

5 Three piezo alignment system

One of the critical aspects in the ET prototype is the control of the suspended mirrors. Since the vacuum chamber prevents manual work on the optics, as soon as the chamber is closed, it was necessary to design an appropriate suspension, that can be steered with motors. The requirement is to align the beam's vertical and horizontal angle. The mirrors are suspended with up to 5 cm long wires and must be controlled in at least two degrees of freedom in vacuum.

The challenge was to move and tilt the mass, without anything touching it but the suspension wires. Thus piezo motors were implemented to tilt a plane and by this steer the suspended test masses. Using curved mirrors, the reflected beam can be steered, using a translation of the mirror, rather than with a rotation of the test mass. The setup is visualised in figure 5.1.

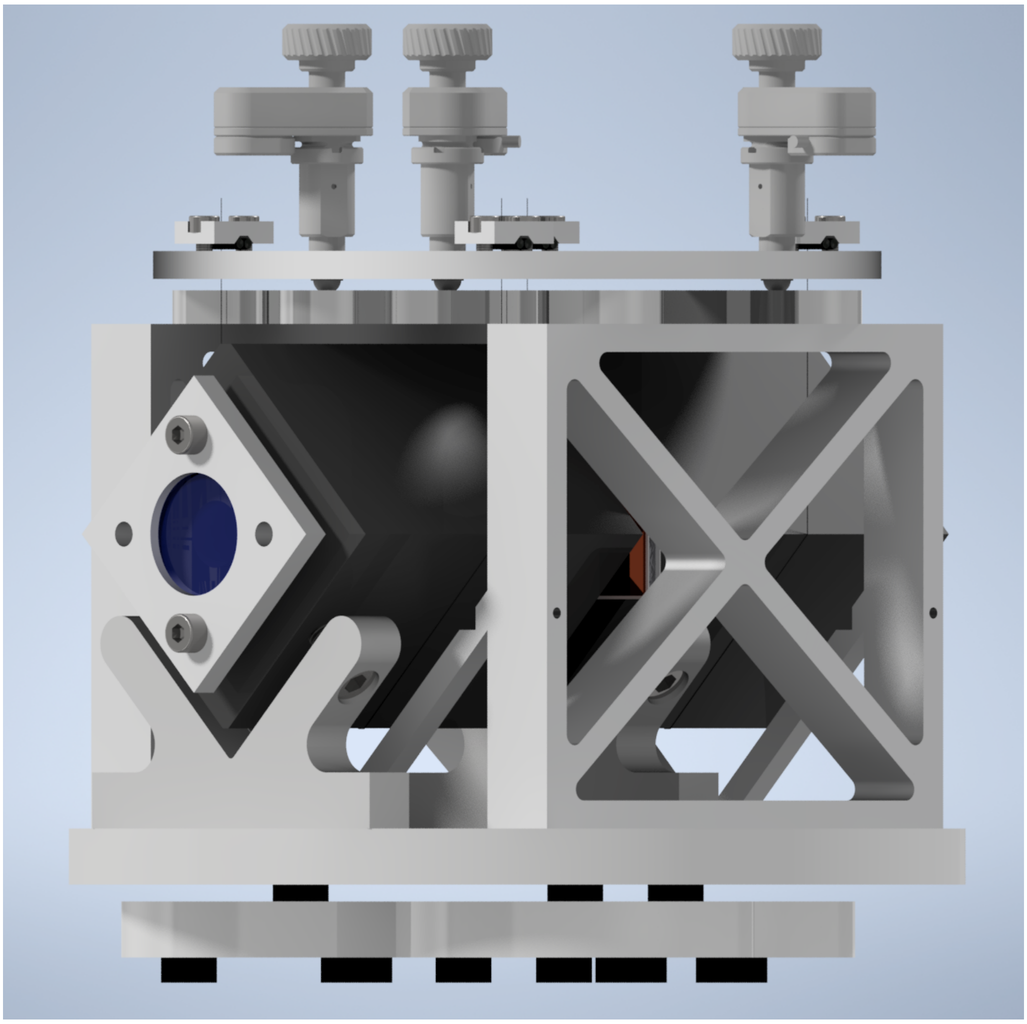

Figure 5.1: A 3D model of the suspension system. The three motors are screwed into an aluminium disk, where the wires are attached. The tips of the motors rest on drillings in a plane below. In operation the wires are the only connection to the surrounding the test mass has. The V-shaped structures below the test mass are limiting the fall height in case a wire breaks, but do not touch the mass in operation.

5.1 The test mass

One of the goals for the Hamburg ET prototype is to measure on the shot noise limit with high squeezing factors. Thus, I designed a setup, that is not as expensive and complicated as other prototypes and can fit on an optical table in a laboratory [58].

In aLIGO the test masses weigh 40 kg each, measure about 35 cm in diameter and have a thickness of 20 cm [59]. Our one inch optics are clamped to tungsten blocks, which adds the majority of the mass of 6 kg in total. The tungsten blocks are rectangular cuboids with a width and height of 50 mm and a length of 70 mm, each weighing 3 kg. The quadratic faces are the front and back side in the sense of this experiment, since they are orthogonal to the beam axis.

In the front and back face of the tungsten blocks are threads for screws. The threads on the backside are left handed. In the centre of theses faces, between the threads, a drilling through the whole length of the block provides a path for the laser. The mirror is clamped onto the front, using a specifically designed holder, shown on the left side in the picture 5.1.

To control the position of the mirror along the optical axis, and thus the round trip phase of the light, a piezo ring actuator is placed on the backside of the tungsten block. A second identical tungsten block without any optics is then screwed to the first one in such a manner, that the piezo is clamped between them and pushes them apart, once a voltage is applied. The piezo can counteract fast fluctuations and distortions up to a movement of about 0.5 µm. Its range is about 1 µm, but the effect is shared between both blocks and therefore the mirror experiences only the halved displacement. The bandwidth of the piezo itself is about 20 kHz.

Other influences like thermal drifts, that happen on much larger timescales like minutes up to hours need to be counteracted to keep the piezo in its operational range. Thus Peltier elements are clamped in between the two tungsten blocks, that transfer heat from one to the other, which leads to a length change ΔL of both. A schematic view of the actuation principle is shown in figure 5.2.

The used Peltier elements have a resistance of a few Ohms, and thus produce heat, when currents are flowing through them, while transferring thermal energy from one side to the other. I expect this additional heating to be small compared to the heat transferred, because we operate the Peltier elements with less than 20 % of their maximum current,

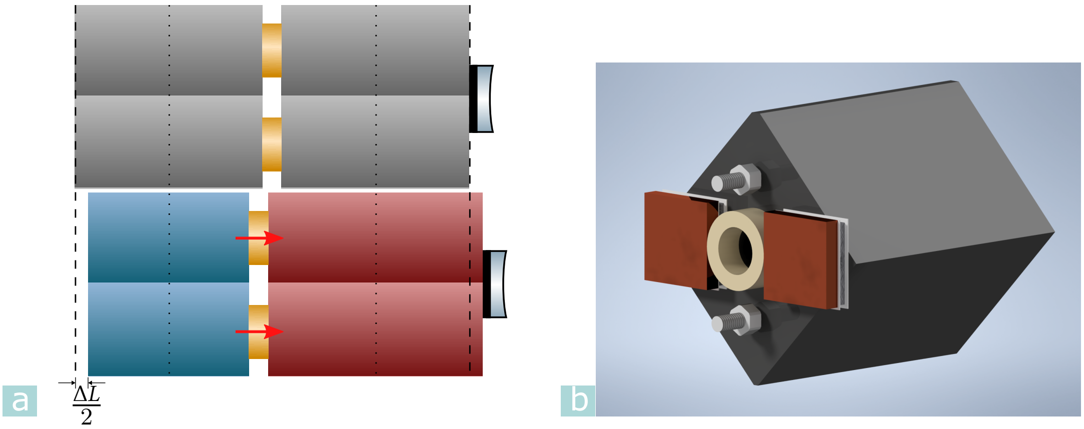

Figure 5.2: The actuators in between the tungsten blocks. a) Schematic view of the thermal stabilisation. In the lower case thermal energy is transported from the left to the right tungsten block. The Peltier elements between the tungsten block allow low frequency stabilisation. Heat is transferred from one to the other block, which leads to a length change of both. The red arrow shows the direction of the transport. The dotted lines mark the suspension points, which are in the planes of the centres of masses of the tungsten blocks. The expansion and shrinkage therefore are symmetrical to them. For a length change of ΔL of the tungsten block the mirror changes its position $\frac{\Delta L}{2}$, which the dashed line shows. b) 3D view on the actuators. The piezo ring is placed centrally on the quadratic face of the tungsten block. The Peltier elements are put next to it. Pieces of copper make up for the different thicknesses of piezo and Peltier elements to ensure thermal contact. The screws pull the two masses together and create a load for the piezo and clamp all elements.

which is where they operate highly efficient. Hence, the absolute value of the length change is nearly identical for both masses, just the sign changes. The suspension points in the centre of each block are considered to be fixed, since they share their planes with the centres of masses of the tungsten blocks. The expansion and shrinkage therefore are symmetrical to these points. The mirror attached to one block is as a result shifted by $\frac{\Delta L}{2}$.

The maximum temperature difference ΔT_{max} between both sides of these Peltier modules is about 70 K in vacuum [60]. The achieved temperature difference is depending on the applied current. Our power source circuit to drive Peltiers supplies up to 750 mA, which is about 19 % of the maximum current. According to the manufacturer, this results in an ultimate temperature difference of about ≈ 30 K [61]. Following the symmetry assumptions previously made, I assume each of the tungsten blocks to change its temperature by half the difference. The length change of the test mass is given by

$$\Delta L = L\alpha\Delta T, \tag{5.1}$$

where L is the test mass length, α is the thermal expansion coefficient and ΔT is the temperature difference. Using the parameters listed in table 5.1, this leads to a change of the mirror position of rounded 2.4 µm in each direction of thermal flux giving a total range of 4.7 µm. Thus the low frequency drifts can be counteracted over a range of multiple fringes.

L	70 mm
α	$4.5 \times 10^{-6}\,\frac{\mathrm{m}}{\mathrm{m\,K}}$ [62]
ΔT_{max}	70 K
$\Delta T_{\mathrm{expected}}$	30 K
$\frac{\Delta L}{2}$	±2.4 µm

Table 5.1: The test mass parameters for thermal control. The power source limits the current to an efficient range, reducing the achievable temperature difference

The Peltier elements are thinner, than the piezo ring and therefore copper pieces compensate the difference. A visualisation is shown in picture 5.3. To clamp the ring piezo, the three actors and two copper pieces, two double-sided screws pull the masses together, just enough to create a load for the piezo. The piezo pushes the blocks apart, if a voltage is applied. To ensure that the copper pieces and Peltier elements do not fall out of the assembly, a tiny amount of vacuum compatible two-component glue on the edge of the tungsten blocks is applied. The copper piece and Peltier element are not glued to each other.

The tungsten blocks have two chamfers, one at the bottom edge and one on the top edge. The bottom chamfer is to distribute the pressure onto the wire, without accidentally cutting it. The top chamfer is a bit deeper to lower the centre of gravity slightly below the beam axis and achieve a more stable system, when the tungsten masses are resting in the wire loops.

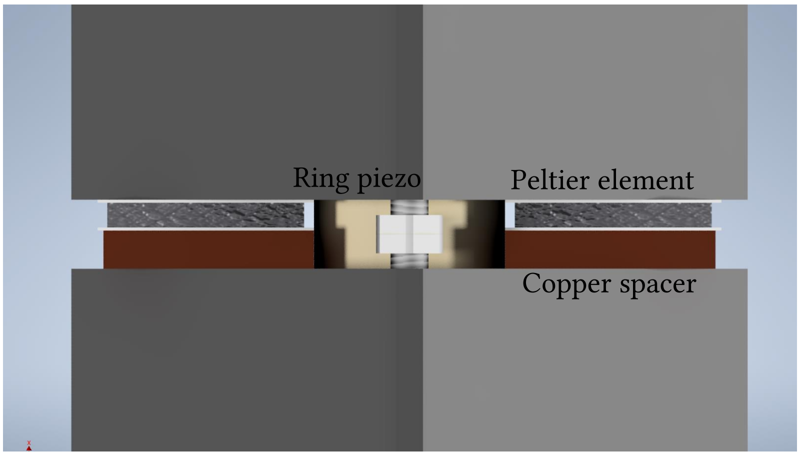

Figure 5.3: Top view onto a 3D model of the test mass actuators. The ring piezo is placed centrally around the hole trough the test mass. Peltier elements are placed next to it. The copper spacers make up for the difference in thickness of the actuators. One double sided screw is visible in the middle and placed above the ring piezo.

The electric devices are wired mostly with vacuum compatible copper wire, insulated with Kapton. This single core wire has a diameter of 0.6 mm and its stiffness leads to a mechanical connection from the test mass to the surroundings, since the wire is connected to the electrical feed trough and guided along the inside walls of the vacuum chamber. Not only do distortions couple to the test mass in mass, but its movement was also disturbed To eliminate mechanical coupling, a small piece of wire is exchanged by enamelled copper wire loop with a diameter of few ten micrometers. This is much more flexible, prevents stress and compression in the wire and isolates both sides from movement.

5.2 Suspending the test mass

The goal, to have suspended test masses and thus reduced coupling to the environment, requires, that the test masses are hanging from the suspension. Since the noise, that reaches the test mass through the pendulum, is damped above the resonance frequency, we want the resonance frequency to be as small as possible. This requires to maximize the wire length.

The wires themselves must be able to carry the weight of the mass while providing minimal friction, thus having a small diameter. For this reason the wires are chosen to be loaded with 60 % of their ultimate tensile strength, providing a safety margin for minor impacts during installation and adjustment. The wire material is the same as the test mass (tungsten) to provoke cold welding, reducing the possible friction. It was challenging to install the test masses with these wires, since the clamping mechanism can weaken the wire's strength, causing rupture.

In section 5.2.1 the first suspension design is explained and measurements are discussed. Section 5.2.2 contains an explanation regarding the improved suspension with shorter wires.

During the installation of the test masses, M. Faden assisted me. The test mass setup in the main chamber rests on a steel plate, that is supported by three rubber feet, which are arranged in an equilateral triangle. The seismic isolation stages are explained in more detail in chapter 6. We noticed a tilting of the seismic isolation platform, such that both stages of steel plates were in contact. This inclination caused a displaced beam and needed to be accounted for. The tungsten masses and the support structure lead to an unequal weight distribution on the plate, which tilts the plane and the steering mirrors, causing the displaced beam. To balance the platform, we removed the test masses and rotated the seismic isolation. The goal was to distribute the weight not mainly on one foot, but on two, and therefore reducing the tilt. The tilt before any counteraction was −10.1 mrad in X-direction, described by α, and −11.2 mrad in Y-direction, defined as β.

As the coordinates in figure 5.4 show, the rotation of the seismic isolation stage reduced the angles α and β by 34 %. To level the plane I added counterweights and reduced the inclination α to a value of −0.2 mrad, which is a reduction of factor 50, compared to the initial tilt. The counterweights also reduced the (absolute) value of β to 2.4 mrad, which is approximately a factor of 5 smaller than initially. The remaining inclination can be neglected, since it was possible to guide the laser beam through the chamber and optical windows as planned.

5.2.1 Design with long wires

The suspension system is shown in figure 5.5a. The support structure is made up of aluminium, except for screws, the motors and tungsten wires. On the seismic isolation

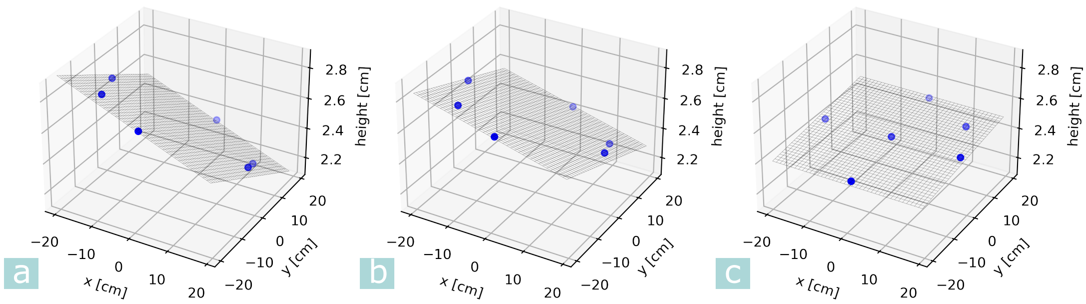

Figure 5.4: We measured the height on different positions in the chamber and Maximilian fitted these to plane equations, visualising the tilt[56]. a) The uncorrected plane, described by tilt in x: $\alpha = -10.1$ mrad, tilt in y: $\beta = -11.2$ mrad. The x and y axes point into the directions of the X and Y arms respectively. The seismic isolation plate supporting the suspension systems is tilted due to unequal weight distribution. Rotating the seismic isolation, so that two feet support the masses, reduced the tilt. b) The plane with rotated seismic isolation, described by α=−6.7 mrad, β=−7.4 mrad, which has a reduced tilt in both directions. Adding counter weights cancels the inclination nearly completely. c) The plane with counterweight, described by α=−0.2 mrad, β= 2.4 mrad, which has close to no tilt left.

inside the vacuum chamber stands a framework, consisting of two walls and a top cover lying on top. There are three holes in the top cover, forming an equilateral triangle. In these holes the tips of the three piezo step motors rest. The motors are screwed into a circular plate and are placed on the top cover. The circular plate has four elongated holes as feedthroughs for two wire loops, in which the test mass rests.

On top of the ring, the wires are clamped, using two cylindrical pins. This is shown in figure 5.6. A clamp above these pins has two surfaces angled at 45°, which press the pins towards each other and squeezes the wire between them. This clamping mechanism was designed by Daniel Hartwig [63].

The wires are made out of tungsten, identical to the test masses to provoke cold welding in vacuum. To amplify the chances for the welding process, I chose thin wires with a diameter of 150 µm, so that the stress is about 60 % of the ultimate tensile strength. This can reduce slipping and friction. In this design the wires are 5 cm long. This leads to a pendulum frequency of 2.2 Hz, calculated with the formula

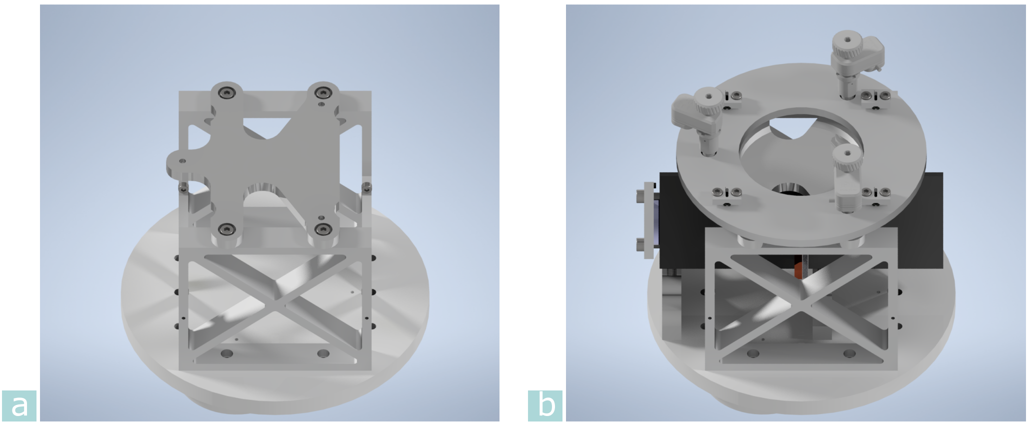

Figure 5.5: The suspension system. a) The framework for the suspension. The three drillings in the top plate are the resting points of the motor tips. b) The test mass hangs from a ring structure. This structure stands on the tips of three linearly moving piezo motors.

$$f = \frac{1}{2\pi}\sqrt{\frac{g}{l}}. \tag{5.2}$$

[64] During construction, the test mass rests on the tips of four screws, which are embedded in two of the V-shaped stands below the test mass. This is shown in figure 5.1.

After we put the wires in place, the wire was tensioned, while tightening the clamps. By driving the motors, which work like screws and push the ring plate structure upwards, as its tips rested on the top plate, the test mass was lifted together with the ring plate. For the test of the long wire design, the interferometer in the main chamber consisted of two of these suspended test masses and was aligned by roughly overlapping the reflected beams and the incoming beams by moving the suspension structure as a whole. The mirrors had a ROC of 1 m. Behind the output of the beam splitter we placed a photodetector. A time series of the voltage is displayed in figure 5.7a.

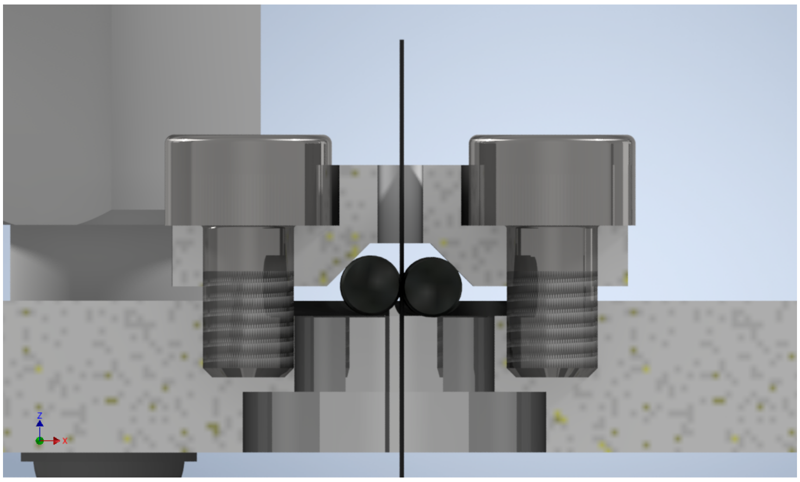

Figure 5.6: Cut through the support plate. The angled clamp presses the cylinders into the wire and hold it in place.

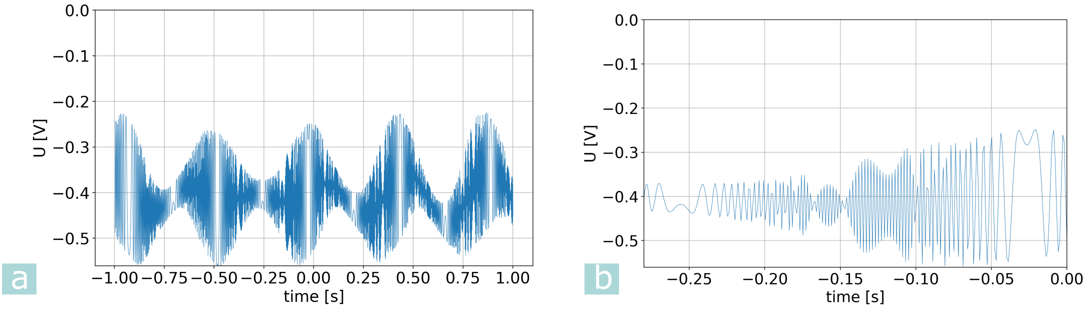

Figure 5.7: Swinging test masses cause a changing output. Yaw movement and swinging in the optical direction shape the signal. a) Time series of the photodiode voltage on the interferometer output with long pendulum wires. Only the input mirrors are in place and form a ≈ 20 cm interferometer. The interference contrast is roughly 40 %. The contrast varies due to excited pendulum and yaw modes of the test masses. The pendulum mode of the test masses leads to visible fringes with the doubled pendulum frequency. b) Section of the time series between two turning points of the test masses. The frequency of the fringe changes is proportional to the differential velocity.

The voltage is proportional to the light power on the detector. The negative sign is caused by the circuit but has no physical influence.

Both beams interfere on the beam splitter and the shown signal shape has an internal structure inside a modulated envelope. This is best visible in figure 5.7b. When the test masses swing in the same direction with the same velocity, the signal remains constant around these points. This happens close to the timestamps $t = -0.26$ s and -0.03 s, because during one period of the swinging identical pendulums, they have the same speed twice. The signal frequency changes sinusoidally with a frequency of 4.4 Hz.

An easier example would be to consider one test mass resting, while the other swings. Per period the swinging pendulum reaches two points of return, where the velocity is 0 for an instant. Then the voltages stay nearly constant in the graph. This doubling of the frequency from pendulum to detected voltage is called *upconversion*. It is also evident, that the contrast of the interference changes over time. Two envelopes can be thought of for the time series, the period of the lower envelope is approximately 0.408 s and for the upper envelope it is 0.456 s. This is equal to frequencies of 2.45 Hz and 2.19 Hz and can be interpreted as the yaw frequencies of the two test masses.

During these measurements I noticed a lateral movement of the beam on the photodetector, which leads to a part of the moving beam not being measured. This observation was made with a viewer card, so that the beams position is visible to the eye. The beam moved sideways but no vertical movement was visible. The beam does not move enough to not be measured at all, since an interference is maintained with much smaller contrast. It changes between values just over 40 %, where the highest signal oscillations are visible, and less than 10 % in the necking. One possible reason for the contrast changes is the yaw mode of the pendulums. This is a rotation of the test mass around the vertical axis through the centre of mass. An illustration is given in figure 5.8a. This leads to the reflected beam moving on the active surface of the photodiode and potentially leaving it, so that a part of the power is undetected. This happens for both beams individually and approximately without correlation. The upper and lower envelope of the graphs change with different frequencies, which indicates different yaw mode frequencies for the two pendulums. The frequency of the yaw mode in a pendulum with one wire loop can be approximated by [65]

$$\omega^2 = \frac{2Tab}{J_z L} \tag{5.3}$$

where T is the tension of each wire, a and b the distance of the suspension points on the frame and test mass, J_z the moment of inertia for rotation and L the wire length.

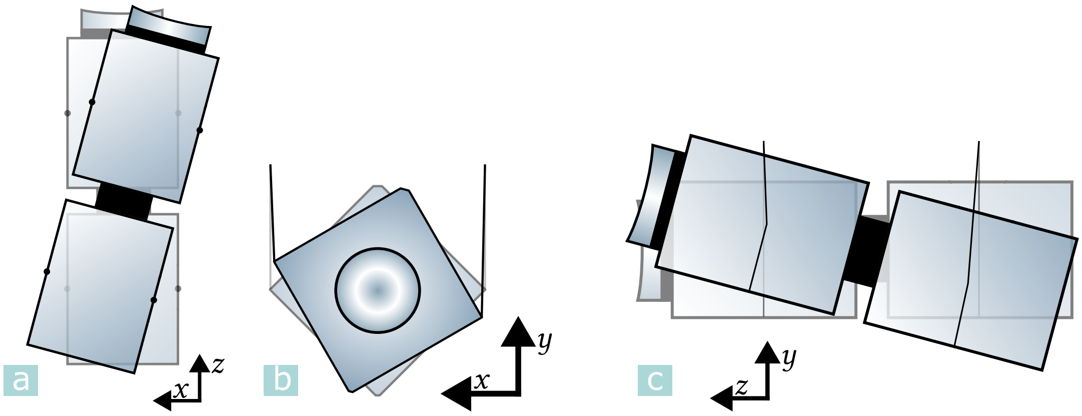

Figure 5.8: The three rotational modes of the test mass, that have a dynamic influence on the beam pointing and the contrast, even when the mirrors are well aligned in resting position. The half transparent pictures in the background show the test mass in neutral position with no rotational mode excited. The x direction is in the optical plane and orthogonal to the beam propagation, y is the vertical direction and z along the beam axis. a) The **yaw** mode seen from above. The rotation leads to the mirror moving in the horizontal plane around the centre of mass. The dots mark the suspension points, where the wires are in contact with the edge of the tungsten blocks. This mode was identified to be problematic, since the beam was severely deflected at the yaw frequency. b) The **roll** mode as seen from the front. Its axis is equal to the beam axis. A rotation around this axis leads to no measurable effect in the light, assuming a flawless mirror. c) The **pitch** mode seen from the side. The mirror moves vertically, rotating around the centre of mass. In the ideal case the wire bends at the point, where it gets into contact with the test mass, but does not move beneath this point or along the edges. We could not identify an influence of this mode, which we expect to operate in the order of kHz with small amplitudes.

T [N]	62.8
a [m]	0.035
b [m]	0.035
J_z [kgm^2]	0.0129
L [m]	0.052

Table 5.2: Parameters of the test masses

The numerical value in this case is 2.48 Hz, using the values of table 5.2, which suggests the approximation formula is adaptable for two wire loops, because it is on the same scale as the observed values.

Since the test mass suspensions are build the same, a and b must be roughly identical as well. The test masses themselves also have the same mass and mass distribution, if we neglect production tolerance, therefore T and J_z can also have only neglectable differences for both test masses. During setup of the suspension we noticed, that the wire length is not easy to control. The wires tend to slip when the mass is lifted and the clamp is not tightened enough, so that the wire is longer as it should be. Unfortunately, when the clamp is too tight, the wires break or rip at the suspension points and need to be exchanged. A lot of finesse and trials are necessary to apply the right torque, so that the test masses are well suspended.

When installing the wire, the test mass lies on the tips of screws in the V-stands, which are adjusted evenly. We adjusted the motors to be at the lowest possible position any time we needed to install or replace a wire. Even though we tried to have the conditions as repeatable as possible, a length difference of one or two millimetres is still possible. Since the wire length is the most probable parameter for deviations, I assume the frequency difference is mainly caused by it. Assuming a length error value of 2 mm, the frequencies values are given as 2.45(5) Hz and 2.19(4) Hz, using error propagation with one sigma values. These errors are too small to explain the behaviour, assuming the yaw mode causes the contrast changes. Therefore taking into account other possibilities of movement, I estimated the pitch mode, seen in figure 5.8c.

The rotation around the horizontal axis perpendicular to the beam is in its approximation formula linear dependent from a parameter, which is zero for the geometry of our test masses, so that it vanishes. Additionally, that pitch mode would result in a vertical

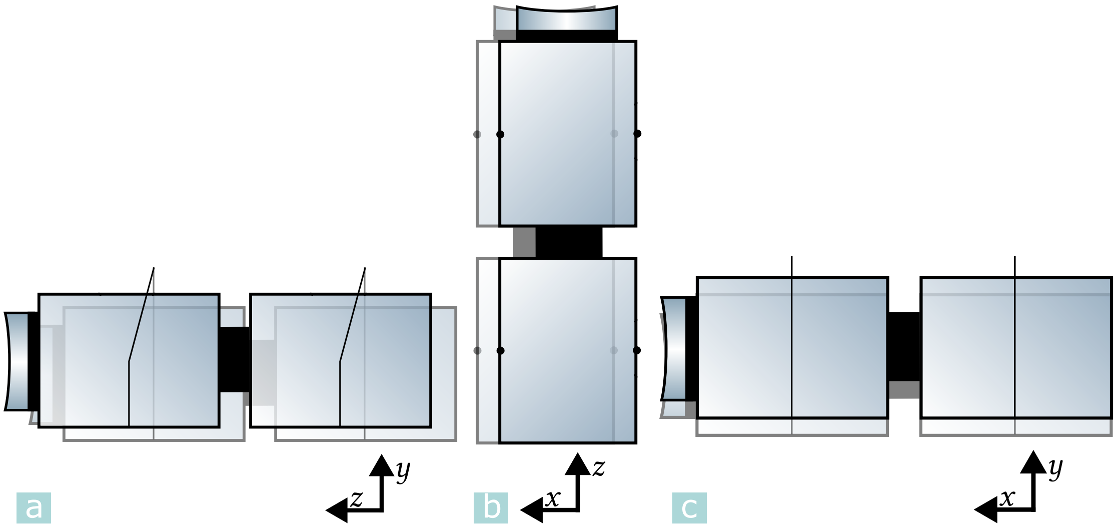

Figure 5.9: The three swinging modes of the test mass. The half transparent pictures in the background show the test mass in neutral position with no swinging mode excited. a) The **pendulum** mode seen from the side. The test mass moves along the beam axis. b) The **perpendicular** pendulum mode as seen from the top. The movement is in the horizontal plane perpendicular to the beam axis. The dots mark the suspension points, where the wires are in contact with the edge of the tungsten blocks. c) The **bounce** mode seen from the side. The mirror moves vertically.

movement and not cause the horizontal displacement of the beam. It is therefore unlikely, that this movement is contributing to the contrast problem, since it was not observed vertically. This was not verified using a quadrant photo diode or a beam profiler, since the horizontal movement was so present, it would have been the dominant factor in any case.

The third mode of rotation is the roll mode (right figure 5.8), which does not effect the beam position and accordingly it can not contribute to the problem.

Other than rotation there is the translation. The motion of the pendulum in direction of the beam is causing the phase difference in the arms, resulting in the changing fringe. The movement perpendicular to the beam axis has the same frequency and amplitude, but since the mirrors are curved, the beam alignment changes. The amplitude can be calculated by counting the fringes between two turning points. In the measurement displayed in graphic 5.7 there are on average 70.8(34) fringes between two turning points, which equals an amplitude of 54.9(26) µm movement.

To summarise the change and modulation in the contrast was most likely caused by a sum of the excited yaw and pendulum modes. These modes never completely vanished, even though the optical table was not touched. Thus I assumed seismical noise as a source of the movement on the table. As S. Verclas measured for her Bachelors Thesis, the concrete block on which the optical table rests has a resonance frequency of 2.2 Hz, which is coincidentally also the pendulum frequency[66]. The fundament is consequently exciting the test masses.

As a solution I redesigned the suspension with shorter wires, so that the resonance frequency shifts towards higher frequencies. Additionally shorter wires would result in less movement for the same energy applied to the system.

5.2.2 Design with short wires

The main difference to the prior design is, that the wires are shortened from 5 cm to 5 mm, achieving a resonance shift from 2.2 Hz to 7 Hz. To achieve that, I designed a suspension structure with distant suspension points below the top structure. Spacers and screws keep a small cage structure in place, which allows the same wire clamping as before. Figure 5.10 shows a three dimensional model of the structure.

This design has two big advantages compared to the one with long wires. The first is the shifted pendulum resonance towards higher frequencies. This moves it away from the 2.2 Hz resonance of the concrete block, reducing its influence on the pendulum motion. In the frequency range above 5 Hz the concrete base has a damping effect on seismic noise and thus a pendulum frequency above this value is necessary. This is shown in chapter 6 in figures 6.2 and 6.3. The second advantage is the now possible conversion of a tilted suspension to a movement of the test mass in unity with a beam steering. A downside is, that the setup procedure is more complex and time consuming, than the one with longer wires. Additionally absolute deviations in the length of the pendulum have a higher relative impact on the frequency now. The goal wire length of the newer design is 5 mm. A minimal vertical distance between the surface of the suspension structure and test mass of 1.5 mm ensures free movement, but also prevents much higher frequencies.

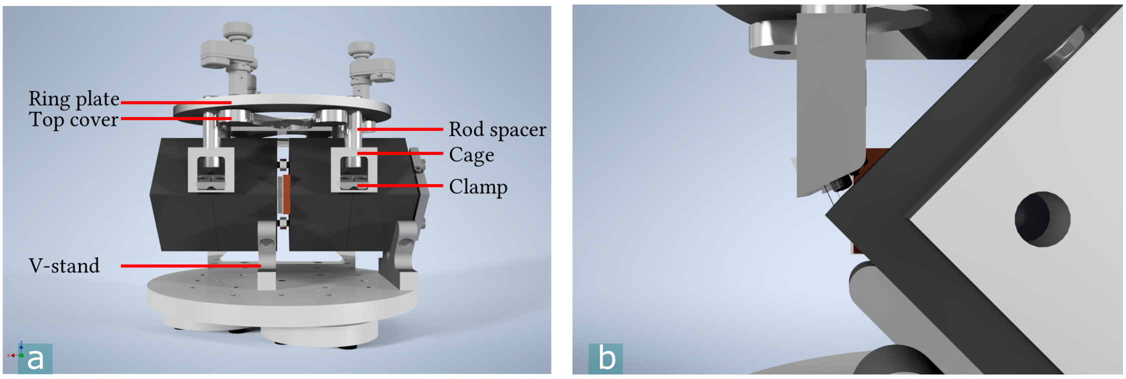

Figure 5.10: The suspension system with short wires. a) The lowered suspension points reduce the wire length. This allows for better adjustment. b) The suspension point is now angled to achieve a smaller gap and thus shorter wires. During installation it is crucial to verify, that no mechanical contact between test mass and suspension structure occurs. The vertical wire length from suspension point to contact with the test mass is about 5 mm. This increases the pendulum frequency to 7 Hz. Additionally the spacers act as a cantilever and allow to vertically move the test mass by tilting the upper platform with the motors. One side wall is not shown for better visibility.

Estimating the resulting wire length to be 5(1) mm, the expected frequency is 7.0(14) Hz, using one sigma error propagation.

5.3 Suspending and alignment procedure

The overall alignment of the ET prototype is very challenging, because three degrees of freedom must be locked synchronously. This includes the mode matching of the two arm cavities (two DoFs) and the interferometer itself (one DoF). To achieve this, I set up a reference cavity, to match all paths onto. The reference is a ring cavity comparable to the PMC, but smaller.

5.3.1 Suspending algorithm

In the following, I explain the workflow, which worked the best and was the preferred procedure to successfully suspend the test masses.

1. Build the test mass outside of the vacuum chamber on a clean surface. Clamp the masses to each other with two Peltiers, copper spacers and the piezo in between. Clamp the mirror to one end surface. Apply a tiny amount of vacuum glue on the edges between test mass and Peltier, as well as between test mass and copper spacer.

2. Set up the framework. Place two v-stands below the framework and regulate the screw tips to stick out 4 mm. This value worked best, but the important constraint is, that the axis of the test mass is later on beam height without the test mass touching anything but the wires. The more the screws stick out, the shorter the wires. Too short wires might cause contact between test mass and suspension.

3. Screw the piezo motors into the ring structure. The motors thread should not stick out more than a few millimetres on the side of the masses.

4. Connect the motors to the electrical feedthrough and test if they are working properly.

5. Retract the linear actuator of all motors.

6. Place the ring with the motors on the framework.

7. Connect clamps, cages and rod spacers.

8. Place the test mass on the v-stands and thread the electric wires through the framework. Connect the wires to the feedthrough.
9. Clamp two tungsten wires, with a length of about 11 cm each, within two cages each. The wires must be of equal length. The wire must be clamped by tightening the clamp screws. Too few torque will lead to a slipping wire and too much will increase the risk of a ripping wire, since the wire diameter is squeezed.
10. Lay the wire loop around the tungsten mass and connect it loosely to the ring structure with screws.
11. Tighten the screws. Ideally this puts tension on the wires, without lifting the test mass.
12. Align the cages, so that their lower edges are parallel to the support walls.
13. Lift the ring structure a few millimetres, to check, if the wire slips or breaks. If so, repeat the last three steps and exchange the wire, if necessary.
14. Place two v-stands, that have no screws sticking out, in the chamber, where the test mass shall be placed.
15. Lift the test mass including the suspension framework into the chamber above the v-stands. The test masses should hang freely and not touch the v-stands.
16. Arange the cables so, that the chamber could be closed.
17. Pre align the mirror, using the whole suspension. Rotate the structure slightly if necessary to make sure your beam is reflected into the desired direction. The piezo motors are only for fine tuning later and can compensate a deviation of maximum 1.5 mrad in horizontal and approximately 4.5 mrad in vertical direction.

5.3.2 Prealign all test masses

Firstly, I installed one end test mass and suspended it. I matched the reflected beam onto the diagnostic mode cleaner. Simultaneously I matched the reflection onto the PMC, thus ensuring that the reflection from the interferometer can be detected on one of the isolator output ports. During this process, manual alignment, by turning the whole suspension structure, was necessary. Important was to account for relaxation effects of the seismic isolation platforms, where the viton feet react on torque and have a restoring force. Once I achieved a stable mode matching above approximately 95 %, I repeated this with the second end test mass, where a matching onto the DMC was now automatically a matching onto the PMC. During this process, the beam of the first test mass was blocked.

After I reached a similarly good matching onto the DMC I installed the input mirrors in the same way. As a result the mirrors for each cavity were already well enough aligned onto a reference and the cavity modes of the arm cavity were visible in transmission. Scanning the cavity length with the laser wavelength, allowed me to optimise the mode matching, with swinging test masses.

Having the mode fixed, I added the homodyne detector and matched it to the output mode.

5.3.3 Piezo alignment

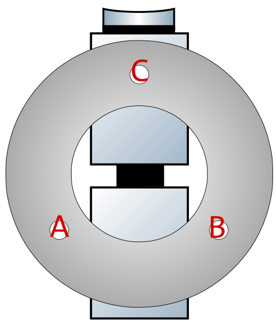

Figure 5.11: The motors are labeled **A**, **B** and **C** in a mathematical positive way, when looking onto it from above. I defined the motor directly above the beam axis to be the **C** motor.

The three motors are arranged in an equilateral triangle with its center above the center of mass of the test mass. One motor is placed directly above the optical axis, which simplifies the vertical alignment. The motors are named **A**, **B** and **C**, where the direction is mathematically positive, when looking onto the setup from above and **C** is above the optical axis. Figure 5.11 illustrates the setup. The weight distribution of the masses onto the motors is approximated by $2:1$ for the motor **C**, compared to the other two. This problem occurs, because four suspension points are distributed onto three motors. This uneven load leads to a different step length, when the motors are working against the gravitational pull. Using four motors instead, to solve this issue, would cause another problem. While three points always define a stable plane, four points are not necessarily in one plane, so that a bistable system could form.

The motors act on the mirror, which deflects the beam. The deflection in X and Y can be described as a matrix: $\begin{pmatrix} X \\ Y \end{pmatrix} = L\mathcal{R}_i \begin{pmatrix} \alpha \\ \beta \\ \gamma \end{pmatrix} = L \begin{pmatrix} c_{AX} & c_{BX} & c_{CX} \\ c_{AY} & c_{BY} & c_{CY} \end{pmatrix} \begin{pmatrix} \alpha \\ \beta \\ \gamma \end{pmatrix}$

with the rotationmatrix $\mathcal{R}$ for the directions i clockwise (c.w.) and counterclockwise (c.c.w.), the number of steps (α, β, γ) applied to the motors **A**, **B** and **C** and the distance from the mirror to the point of measurement L. The matrix coefficients c_{jk} define the coupling between motor action and beam angle.

I measured the deflection, caused by mirror movements, by placing a beam profiler behind the vacuum chamber. One arm was blocked, to observe only the displacement of the beam. For these measurements, I installed mirrors with a radius of curvature (ROC) of one meter at the position of the input test masses.

These deflection values are unfortunately only reliable relative to each other, since the distance from the beam profiler to the mirror was not noted, when making this measurement. I reconstructed the value and estimated it to be 1.00(15) m, so that the error is not arbitrary large, but it remains an estimation. Since this is true for all values equally, the relation between the factors is reliable nonetheless.

I calculated the deflection coefficients with the measurements shown in figure 5.12. The numbers correspond to the order of measurements and each data point is marked with a cross. For every measurement 100 data points were taken to average the position. The first measurement were taken as a reference value and thus set to the coordinates $(0, 0)$. For each direction rows of values, that did not lay at the horizontal boundary, were used and a linear function fitted to them. Afterwards, these values were converted to angles and used for the error propagation, which includes the one sigma standard deviations of the fitted coefficients and the distance uncertainty of the beam profiler.

The angles are summarised in the following matrices. For these small angles the small angle approximation $\tan(\phi) = \phi$ can be applied, so that the displayed angles are equivalent to the matrix coefficients.

$$\mathcal{R}_{\text{c.w.}} = \begin{pmatrix} -0.144(22) & 0.085(13) & 0.006(1) \\ 0.231(35) & 0.159(24) & -0.246(37) \end{pmatrix} [\mu\text{rad/step}]$$

$$\mathcal{R}_{\text{c.c.w.}} = \begin{pmatrix} 0.186(31) & -0.114(20) & -0.001(2) \\ -0.285(43) & -0.133(20) & 0.299(46) \end{pmatrix} [\mu\text{rad/step}]$$

An important feature these values show, is that the movement of the motors A and B lead to a deflection in the horizontal plane and the motor C does not. This is explained by the positions of the motors relative to the suspension points. C is directly over the beam axis, while A and B are symmetrically left and right of it. In combination with the suspension structure for the short wires, I expected a displacement, which is verified by this result.

The figure 5.12a shows, that the mirror moves to the side for six measurements (10-16) with 2000 steps each. For an unloaded motor this is equal to a range of 0.3 mm, which induces theoretically 1.4 mm of motion of the test mass. These limits could be explained by the test mass gliding in the wires, the test mass touching the v-stands below or the suspension touching the framework. Latter would only explain a one sided limit, since the motors A and B can only cause a tilt to one side each.

The mirrors sometimes do not move horizontally, even if they should and I could not figure out a clearly defined reason besides a potential gliding in the wire or a blocked movement.

When changing the moving direction of the motors a small reproducible shift occurs, which is most likely caused be a change of the torque direction. The torque appears when a rotational force is applied, which is what is happening at the tip of the motor.

Figure 5.12b illustrates the behaviour for motor B, which is analogous to the one of motor A. The horizontal deflection of motor B is opposed to the one of motor A, since it is on the opposite site of the beam axis. Whereas the vertical movement of both motors have the same direction.

It is noticeable, that the step width of motor A is larger than of its counterpart B. There is no difference by design between these, so they should be similar. This circumstance remains unexplained. During the adjustments the motors behaved nonlinear often when close to the end of their operating ranges. Maybe this was the case for motor B.

The reason, that the counterclockwise rotation has a larger step size, than the clockwise, is the weight of the test mass. The resulting force counteracts the movement, lifting the

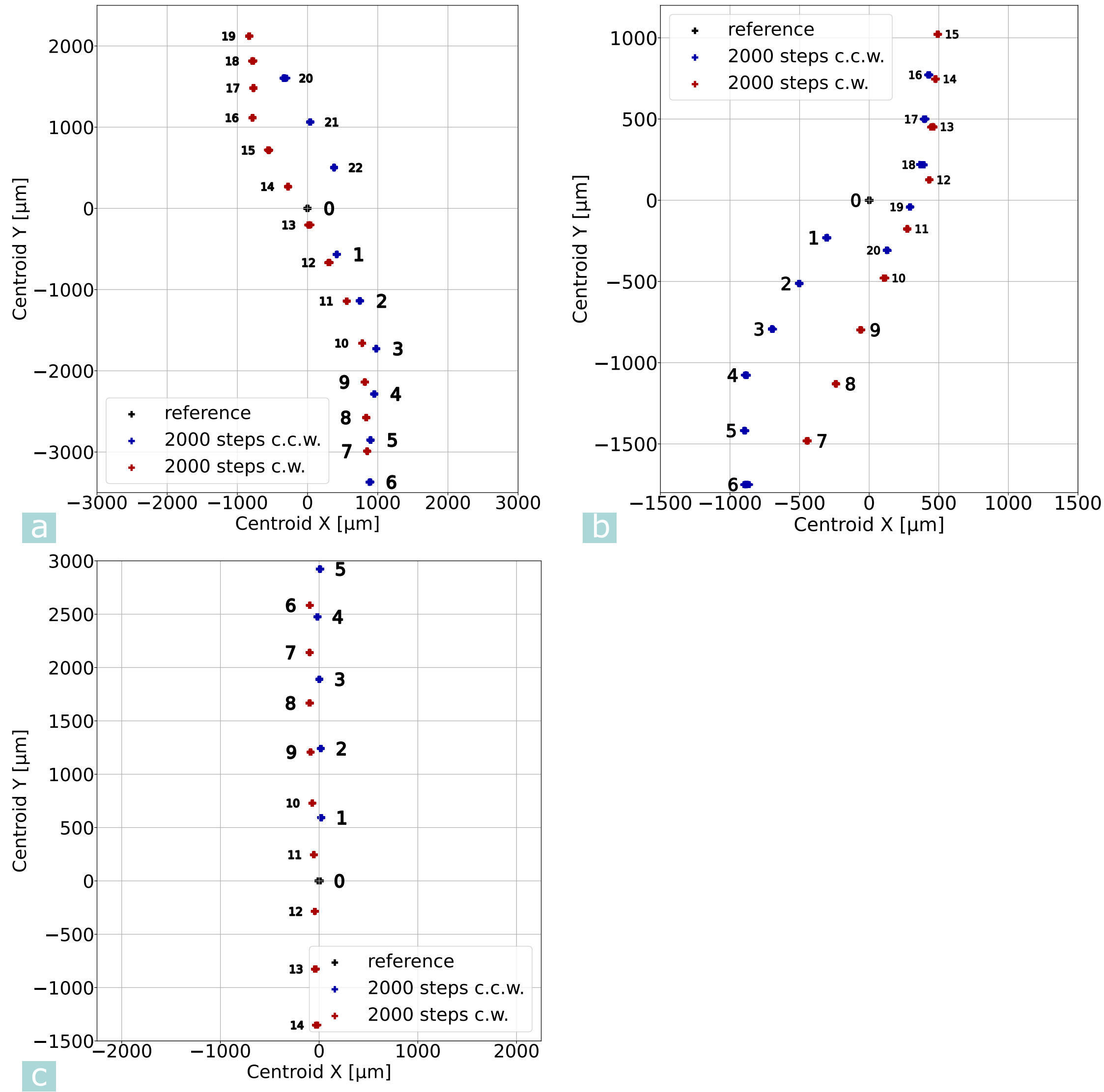

Figure 5.12: The beam deflection with the individual motors. a) Motor A, b) Motor B, c) Motor C. Measured approximately 1 m behind the BS output. The '+' markers are located at the positions of the beam and the numbers show the order of the movements. The colour indicates the movement of the motor, upwards is blue, downwards is red. The motors movement is linear around the reference and a horizontal deflection is present for motors A and B. The horizontal beam angle is limited and shows a behaviour close to a hysteresis. Furthermore the horizontal deflection of the motors is in opposing direction, while the vertical beam movement is in the same direction. Motor Cs vertical deflection opposes the other motors and shows only a minor horizontal shift after changing the direction of movement. For each direction rows of values, that did not lay at the horizontal boundary, were used and a linear function fitted to them. Afterwards, these values were converted to angles and the uncertainty used for error propagation, which includes the one sigma standard deviations of the fitted coefficients and the distance uncertainty of the beam profiler.

test mass up. This happens, when the screws of the motors are turning in a clockwise direction.

This is true also for the last motor C. This motor acts on the beam mostly vertically. A small horizontal deflection is visible at the turning point of the movement direction. In the figure 5.12c this happens between steps five and six.

Limiting factors for the movement of the suspension system are illustrated in figure 5.13.

v-stands The support structures below the test mass to prevent falls from height are placed centrally under it. The space between test mass and v-stand allows the test mass to move freely, but when the test mass is adjusted with the suspension structure, the distance between tungsten block and v-stand can shrink down to both touching. In the optimal case the test mass hangs in the middle of the framework, the horizontal and vertical distance is 5 mm.

Framework The framework on the sides of the suspension structure can not touch the tungsten masses directly, but the small cages containing the wire clamps. These can block further movement, when a horizontal adjustment leads to them touching each other. Ideally the space to either side is 2.6 mm.

Top plate The plate, which connects the support framework and is also the base for the motor tips limits the height position of the test mass. When lifted too high, the test mass will collide with the top plate and the forces might cause a breaking of wires or that these slip out of the clamping mechanism. The designed default space is 3.6 mm.

Additionally, for tilts of the test mass using the C motor, also clipping of the beam may occur. This theoretically limits the range also, but is not problematic in the experiment, because the range is far bigger than needed. It can in fact be used to actively suppress a reflection and interference of the beams, if necessary.

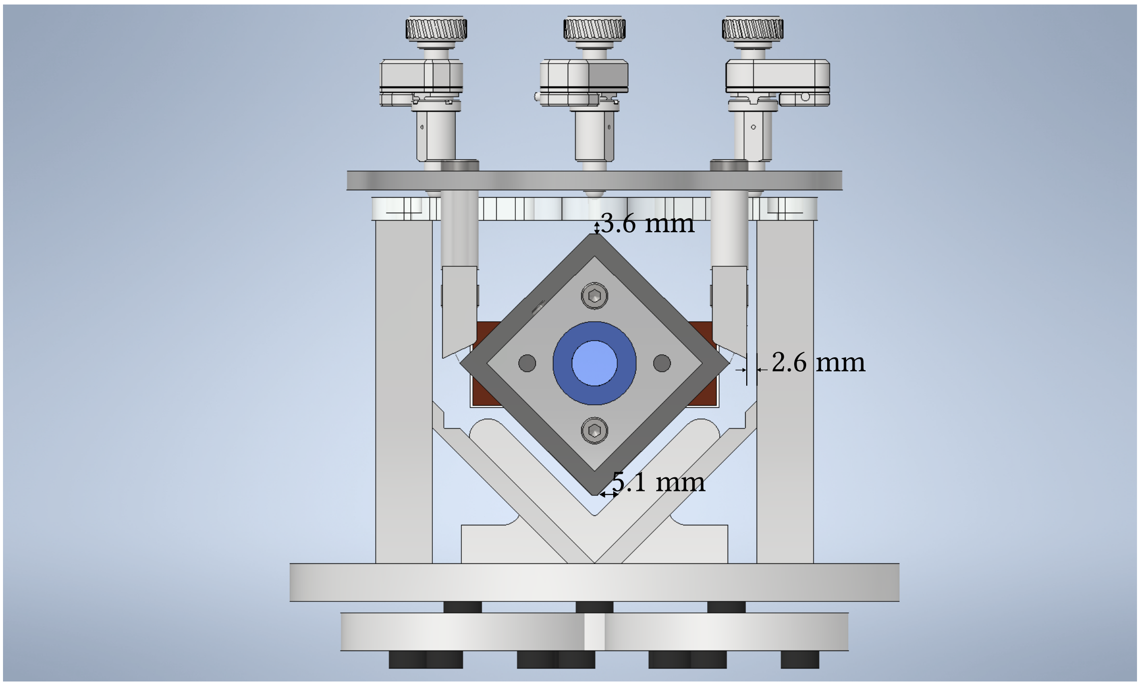

Figure 5.13: The v-stands, framework and top plate set limits for the movement of the test masses.

5.4 The vacuum system

As previously explained, the test masses need to be isolated from the surroundings as well as possible. Thus the suspensions are placed inside a vacuum system. The system consist of five chambers, as visible in picture 5.14. The main chamber with a diameter of 40 cm is connected to two steel pipes, of which the axes form a right angle, needed for the arm cavities. At the end of each pipe, one 20 cm diameter chamber is attached, which contains one end mirror. Additionally two more 20 cm chambers are attached on opposite sides of the main chamber, forming a 45° with the arm cavities. These are meant to contain the PR or the RSE mirrors in the future.

Summarising the results, the test mass suspension is controllable using three piezo motors, that tilt the suspension plane. This allows to steer the mirror and the beam in the closed vacuum chamber to reach good mode overlap and interferometer contrast. The maximal horizontal deflection was measured to be about 1.6 mrad and the vertical about 4.5 mrad.

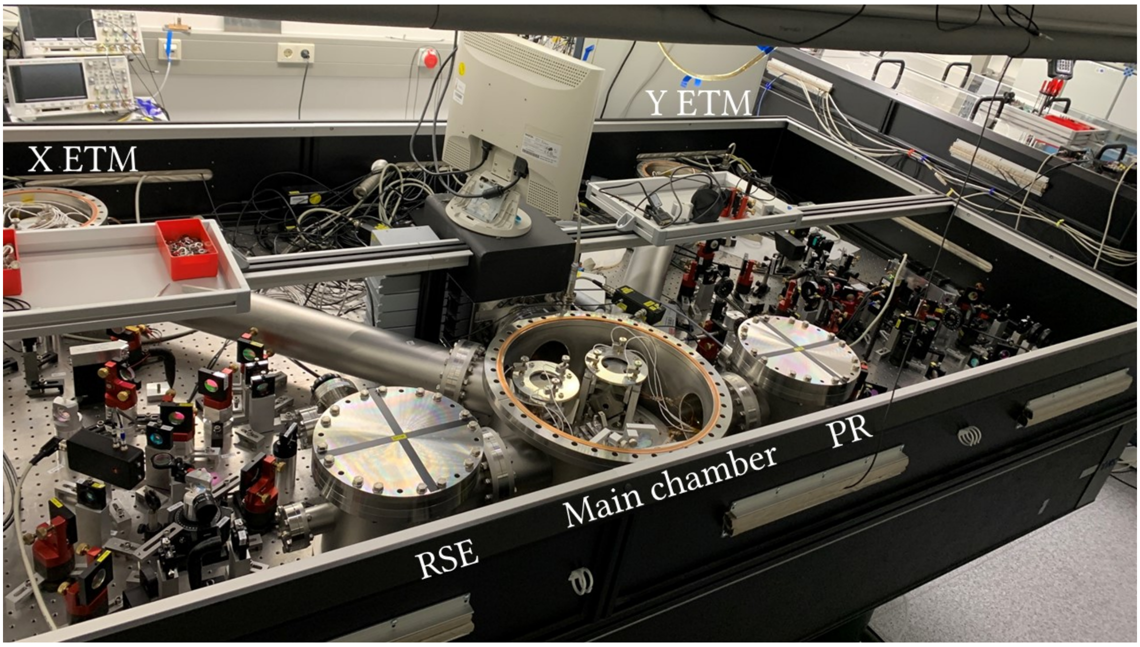

Figure 5.14: Photo of the optical table with the vacuum system. The main chamber and the two side chambers for the end mirrors are open. Two more side chambers are closed

6 Seismic isolation feedback control

The seismic noise is a limiting factor for GWOs, this is also true for the comparably small prototype. Since the seismic excitations are causing continuous fluctuations in the optics movements, it is necessary to dampen and counteract these.

6.1 Passive seismic isolation

The seismic isolation in the experiment consists of several stages, complementing each other, to reach a high value of attenuation, as shown in figure 6.1. Starting at the basis a concrete block resting on springs is the first stage. Its weight can estimated to be 32.7 metric tons, using its dimensions, measured by Daniel Hartwig and Jan Petermann for their project on a similar block, and the density of 2.5 g/cm^3 as a rough mean value [67].

S. Verclas examined the seismic noise in neighbouring laboratories and compared the noise on the lab floor with the noise on top of a concrete block similar to the one for the Hamburg prototype. Her comparison measurements are shown as frequency spectra in figures 6.2 and 6.3. The used seismometers were the Nanometrics Trillium120QA and Geotech Instruments GS-13.

The data taken proofs a reduction in horizontal noise in the frequency range 6 Hz to 40 Hz by a factor around five. For higher frequencies a damping effect can only be assumed, since the seismometers were operating at their measurement limit and could not proof or quantify a noise reduction [66, Chapter 2.1.2]. For the frequency range from 1 Hz to 6 Hz the noise is amplified with a resonance at 2.2 Hz.

Vertical noise is reduced by the block from 4 Hz to over 200 Hz, where the measurement range of the seismometer ends, by more than one order of magnitude. The vertical noise resonance is at 2.8 Hz, resulting in a amplification of noise in the range from 0.3 Hz to

4 Hz. To sum up, the concrete block attenuates the seismic noise above ≈ 5 Hz by roughly one order of magnitude. The vertical attenuation is higher, than the horizontal one [66].

On top of the concrete block the optical table rests on pneumatic vibration isolators. Their damping is specified by the manufacturer Newport with −20 dB per decade for horizontal and −40 dB per decade for vertical excitations above the resonances at about 1 Hz [68]. These were inactive during measurements with the long wire suspension, because their resonance frequency around 1 Hz in combination with the one from the concrete block excited the pendulums up to a point, where no control over the Michelson fringe was possible. For later experiments with the short wires, they were used.

The table itself has damping properties regarding its own resonances, to behave like a rigid body [69].

During our Masters Theses, Alexander Franke and I developed and optimised a vibration isolation stage for high frequencies [70, 71]. The isolator consists of one big steel plate resting on three FKM (Fluorine Kautschuk Material/Viton) feet, which rest on smaller steel plates. These are themselves supported by three FKM feet each. The simulated behaviour is shown in figure 6.4 and the $\frac{1}{f^4}$ behaviour expected from equation 2.33 for a two-staged vibration isolator is well visible.

Such isolation platforms are on top of the optical table inside the vacuum chambers and further reduce high frequency noise, which could also be acoustic waves, coupling to the chamber.

Lastly the pendulum itself is an isolating element as well. The test mass is in the final version of the experiment suspended with wires of ≈ 5 mm length. This results in a resonance of about 7 Hz. In this region the concrete block dampens the seismic noise, instead of amplifying it, as visible in figures 6.2 and 6.3. More details can be found in chapter 5.

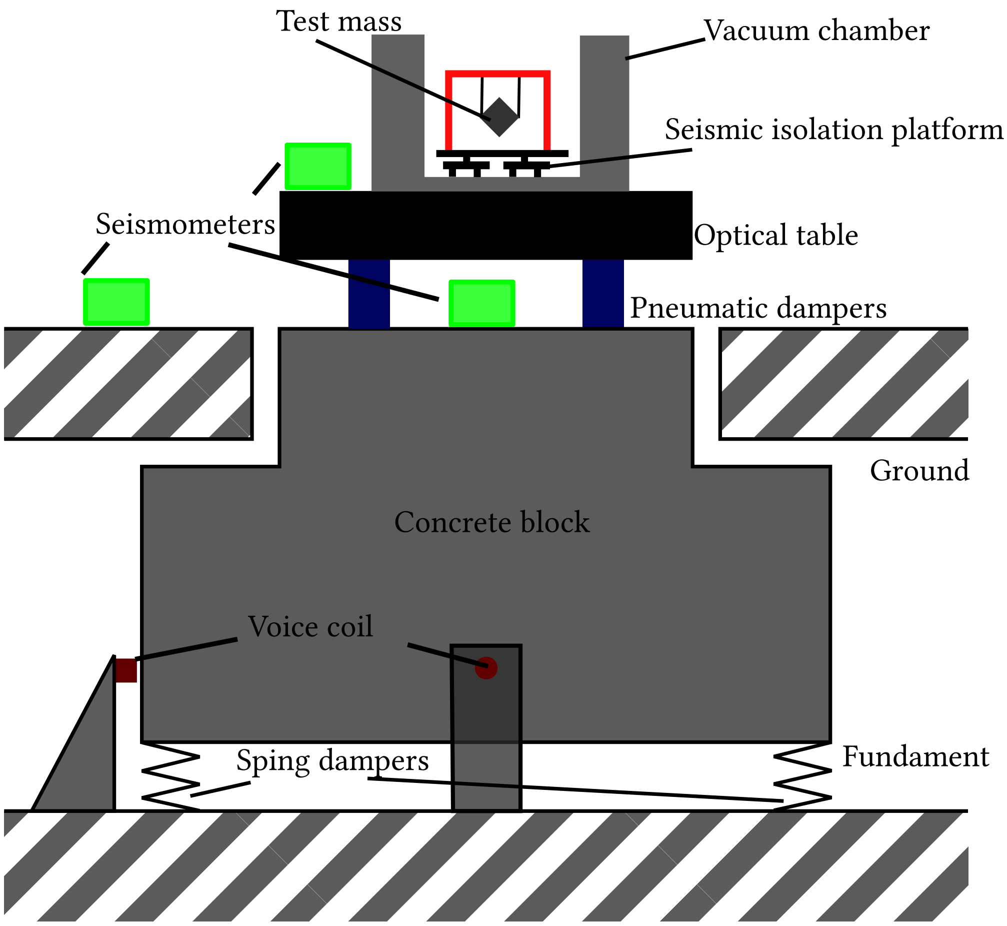

Figure 6.1: A schematic view of the seismic isolation. The concrete block is mounted on springs and can be actively controlled with voice coil actuators shown in red. The goal is to keep the surface of the optical table as stationary as possible. The blue pillars can be used to air suspend the optical table. The shaded areas are the structure of the building. In green the positions for seismometers, needed to measure the effect of the isolation stages, are shown.

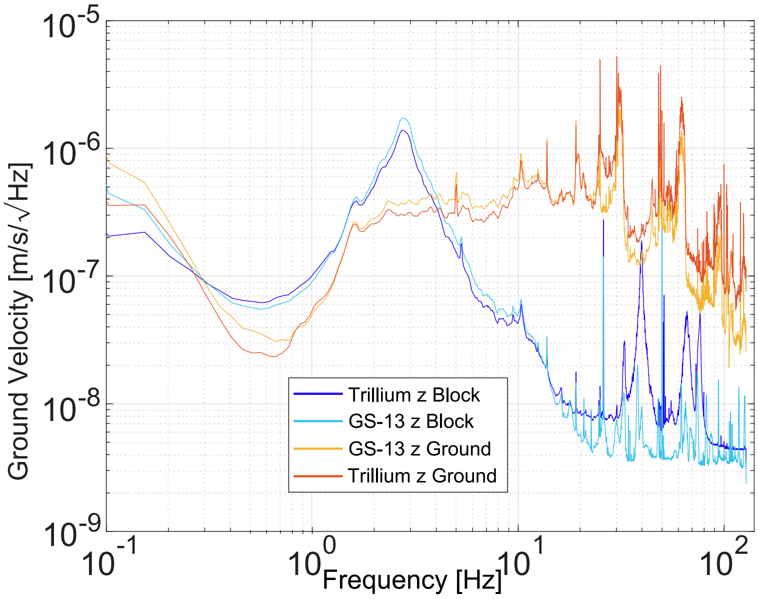

Figure 6.2: Seismic isolation effect of the concrete block. Vertical noise is damped above 4 Hz. Between 0.3 Hz and 4 Hz the noise is amplified, especially around the resonance at 2.8 Hz. Figure kindly provided by S. Verclas.

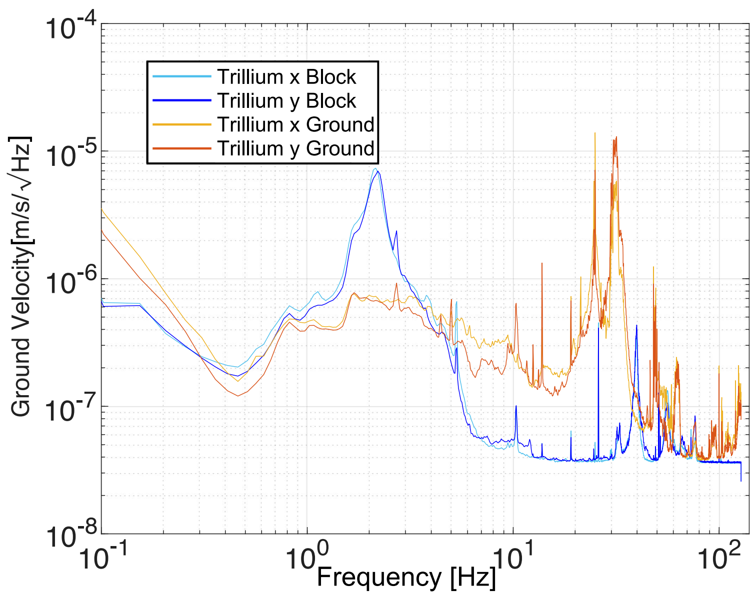

Figure 6.3: Seismic isolation effect of the concrete block. Horizontal noise is damped above 6 Hz. Between 0.3 Hz and 1 Hz the noise is amplified, especially around the resonance at 2.2 Hz. Figure kindly provided by S. Verclas.

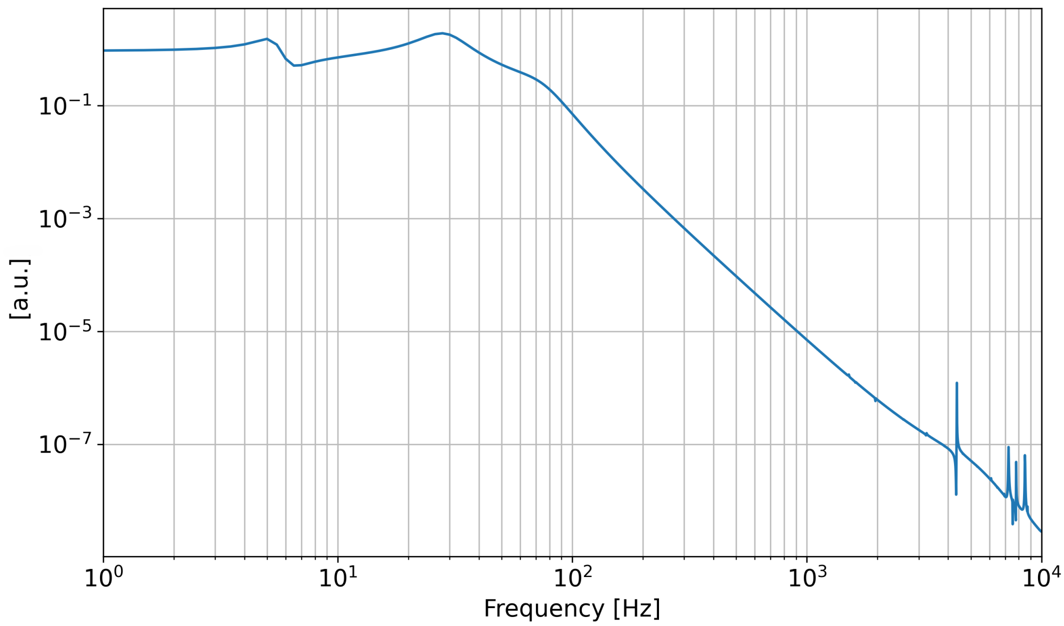

Figure 6.4: COMSOL simulated frequency dependent transfer function of the seismic isolation stage in the vacuum chamber. Evaluated is the horizontal motion of the top plate while a distortion in the same direction is applied to the rubber feet under the lower stage. For frequencies over 30 Hz the responses drops roughly with $1/f^4$. Data provided by Alexander Franke [70].

6.2 Active regulation

To stabilize the concrete block of the experiment, a control system was set up in cooperation with Nima Ehsani Armaki and Daniel Hartwig. The control system is based on the design, which was developed for the *MassQ* Experiment from Daniel Hartwig.

The system consists mainly of two voice coils, which apply a force onto the block to reduce its motion. The coils are installed at the bottom of the concrete block, where it rests on the springs, see figure 6.1. The block has a quadratic footprint and the actuators are placed in the middle of two neighbouring sides, in the height of the springs. This allows to control the two different degrees of freedom.

The error signal for the system is provided by a Trillium seismometer, standing on the concrete block below the optical table. This gives information about the velocity of movement in three dimensions. For the two axes spanning the ground plane, the signals are fed into a digital PID *ADwin* controller. This device, together with software *NQontrol*, written by C. Darsow Fromm, allows to apply frequency filters, integrating, differentiating and gain stages digitally to the signal, before it is passed onto the coil driver [72].

The measurements of the transfer functions, the filter design and optimisations were done by Daniel Hartig and Nima Ehsani Armaki. A more detailed description can be found in their theses [63, 73].

The graphs in figure 6.5 show the frequency resolved movement of the surface of the optical table for different configurations. The active control loop improves the damping between ≈1.5 Hz and 5.5 Hz. In the small frequency limit the noise is left unchanged. Adding air suspension to the passive damping improves the noise damping in the frequency range above 3.5 Hz, while it drastically increases the noise for frequencies below 1 Hz.

Concluding the experiment is isolated against seismic noise by several passive and one active isolation system. These suppress possible excitations due to seismic waves in the important frequency band 5 to 7 Hz. It suffices to allow a stabilised arm cavity, as explained in chapter 7, but further improvements in the active stabilisation in the future would be helpful to increase the time span the system can stay in a locked state.

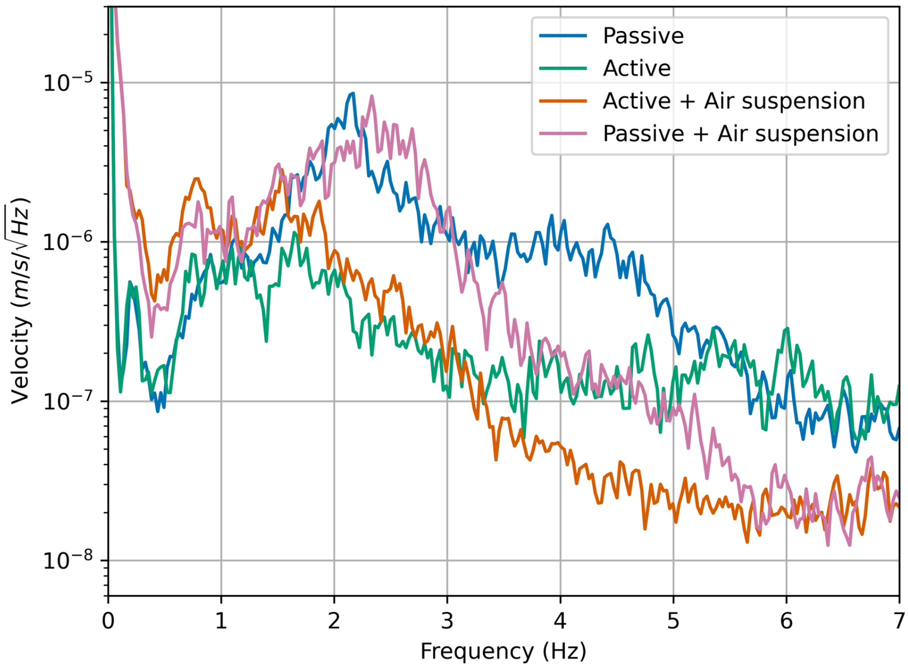

Figure 6.5: Comparison between passive damping and active control, both with and without using the air suspension. Passive means the damping of the concrete fundament. Active means the voice coil actuators additionally counteracted the movement of the concrete block. The lines show, that in the region of 2 Hz to 5 Hz a visible noise reduction between a regulated and an unregulated system can be achieved. Above 3.5 Hz the air suspension significantly reduces noise. Above 6 Hz the air suspension is the most important damping factor. The measurement was made and the data provided by Daniel Hartwig and Nima Ehsani Armaki.

7 Stabilised Michelson interferometer

A Michelson interferometer's sensitivity for gravitational waves is increased, when arm cavities are added. For a positive effect the light must circulate in the resonators. This only happens on resonance. The resonance state is fragile and a control loop and actuators must act on the mirrors or the laser, to maintain this state. Additionally, the arms must be stabilised against each other, so that the output is constant. How I achieved these stabilisations and how well they perform, is explained in this chapter.

7.1 Michelson fringe Lock

To measure gravitational waves, the signal to noise ratio should be maximised. The photon shot noise is dependent on the light power and the output power of the interferometer is dependent on the phase difference of the light returning from the mirrors. Using the number of photons n and the optical phase difference of the light coming back from the arms, the signal to noise ratio (SNR) is given by

$$\frac{d\bar{n}_{\mathrm{out}}(\phi)}{\sigma\left(\bar{n}_{\mathrm{out}}\right)} = \frac{\sin\left(\frac{\phi}{2}\right)\cos\left(\frac{\phi}{2}\right)d\phi\bar{n}_{\mathrm{in}}}{\sin\left(\frac{\phi}{2}\right)\sqrt{\bar{n}_{\mathrm{in}}}} \overset{\phi\neq 0}{=} \sqrt{\bar{n}_{\mathrm{in}}}\cos\left(\frac{\phi}{2}\right)d\phi, \tag{7.1}$$

[74] which is maximal for $\phi = 0$. $\bar{n}_{\mathrm{in}}$ and $\bar{n}_{\mathrm{out}}$ are the mean number of photons propagating into the interferometer and transmitting through it. Under the condition $\phi = 0$ the signal vanishes completely, so the perfect spot is close to 0, but unequal to zero. Therefore the interferometer is operated close to the configuration called dark port or dark fringe, because the light is reflected back to the input of the interferometer and no power is transmitted to the output.

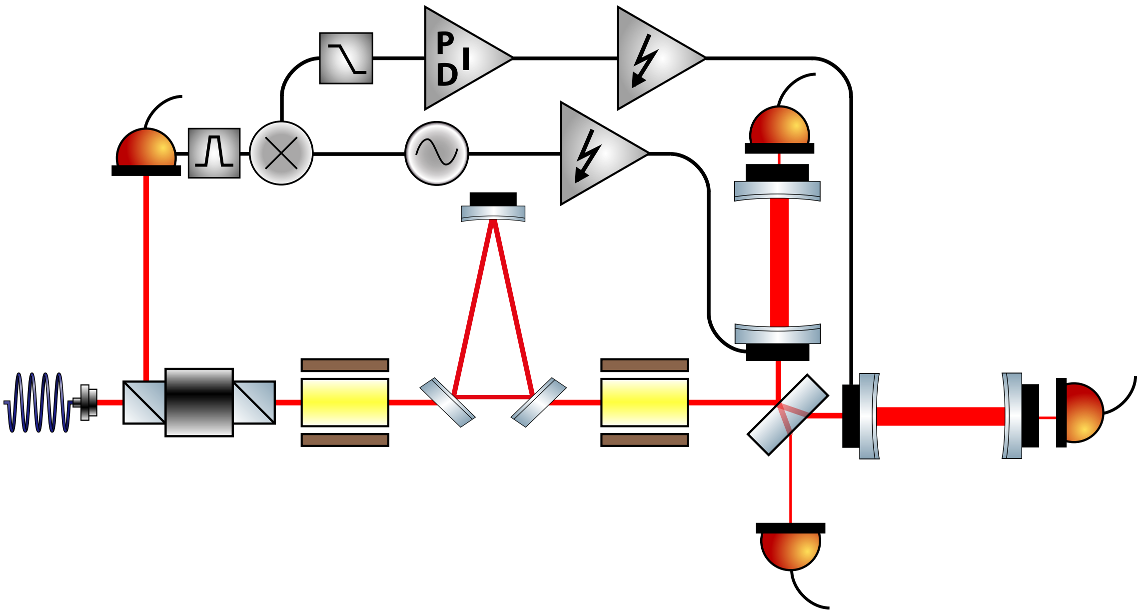

Figure 7.1: Scheme of the dither lock principle. One input mirror is dithered and the signal read out in reflection from the interferometer. To do so, I placed a PD behind the output of the isolator. Demodulating with the dither frequency creates the error signal to lock onto the extreme points of the fringe, like the desired dark output.

To lock the interferometer close to the dark port, its arms must be stabilised accordingly. Thus error signals must be generated using photo diodes, that measure the light power. If the light power is measured behind the interferometer, it must be minimized and if measured in reflection from the interferometer, maximised.

Since the power fluctuations are several Watts in the unlocked state, the photodiodes might be destroyed. Optical loss can not be used to minimize the light on the diodes, since the squeezed light, which will be installed in the future, is very sensitive to loss. Thus, I installed the PD for locking in reflection of the interferometer at the output of the Faraday isolator, as shown in figure 7.1. In the locked state the complete light power is reflected, providing a large signal to achieve a locked state. The lock at the extreme points of the fringe, like the dark output, I need to generate an error signal. This can be done for Michelson interferometers for example with the help of asymmetric distances of the input mirrors to the beam splitter and modulation sidebands, also called *Schnupp asymmetry* or *Schnupp modulation* [75]. To prevent mode mismatch in the output

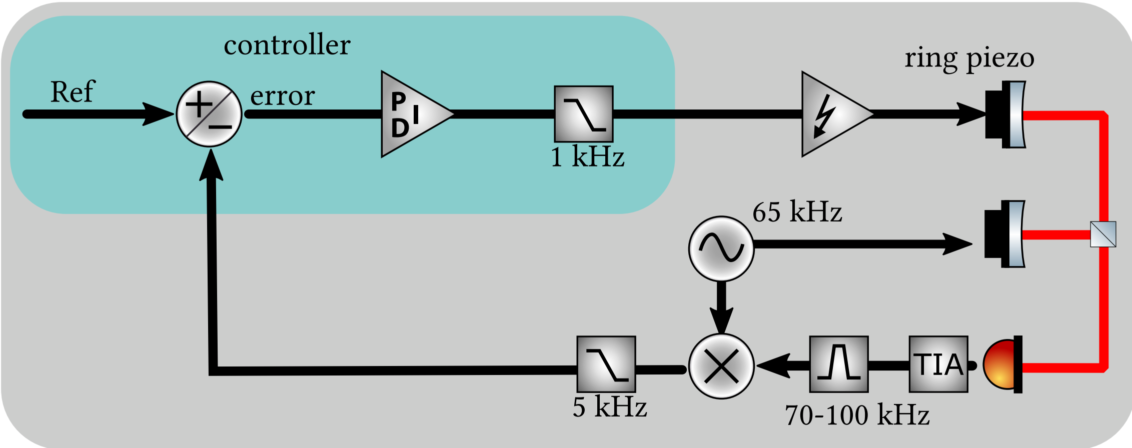

Figure 7.2: Block diagram of the dither lock principle. The signal detected by the PD is band pass filtered and demodulated to create the error signal. The servo creates a control signal, which is fed to the HV amplifier and thus to the attached piezo.

by different propagation length I decided for a different method, the dither lock. This technique uses a vibrating mirror, which creates a phase modulation, which is converted to an amplitude modulation on the beam splitter. This amplitude modulation is measured with the mentioned PD and band pass filtered. Afterwards, the signal is demodulated with the initial frequency and lowpass filtered to elimiante higher order terms. This gives the error signal, shown in figure 7.3. The measured signal shows the same behaviour as the simulated curve and allows the dark fringe lock.

The dither frequency of 65 kHz was chosen, because it must be high enough to not disturb measurements in the linewidth of the cavity, which is designed to be 80 kHz. The piezos only work in a limited range with their full range, which is 20 kHz for the piezo with the used HV amplifier. Thus the frequency was swept in the range of 10 kHz to 100 kHz and the amplitude of the signal and error signal observed. A not further examined mechanical resonance led to a higher amplitude, than for the frequencies around. Thus this frequency was chosen to dither the mirror.

The figure 7.4 shows the stabilised output power. The PD voltage stays constant, as long as the piezo can counteract changes, thus stabilising the error signal to zero. The visible peaks in the PD voltage occur, when the piezos reached the end of their ranges and could not counteract the whole movement. I expanded the range by using both input

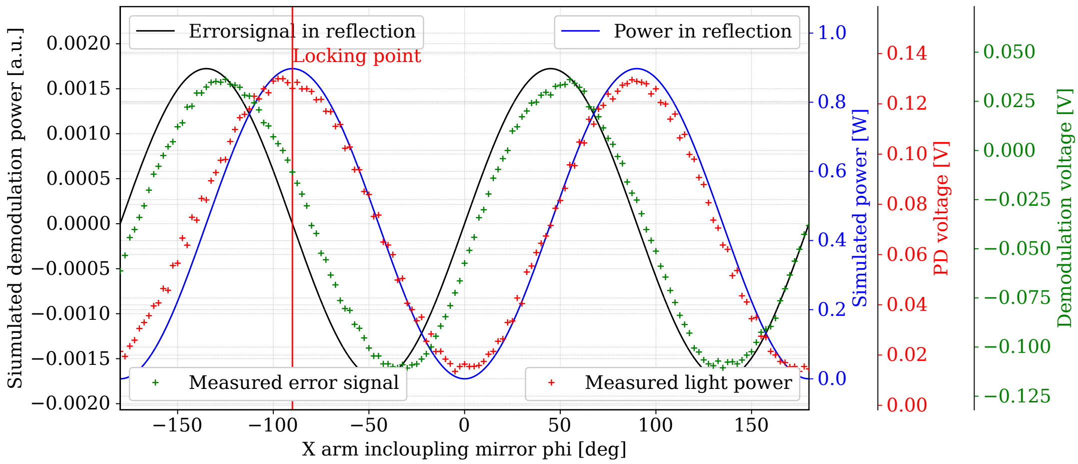

Figure 7.3: Simulated error signal of the interferometers fringe position compared to the measured values. Dither frequency is 65 kHz. It is noticeable, that the error signal is a scaled derivative of the light power. The measured error signal was recorded after exciting the pendula and the time series converted into the phase. The error signal of the dither lock is the derivative of the power in regard to the phase difference. The measured signal fits well the simulated curve and was inverted for better visibility. The difference in the sign is of no importance, since during the signal processing it can be easily inverted, if necessary. A phase shift by 180° in the demodulation process would yield the same effect. Since the velocity of the test mass changes during its pendulum motion, the conversion to phase gets distorted towards the turning points, resulting in a shifted phase. The goal is to lock on the maximal light, because it is measured in reflection from the interferometer.

mass piezos with opposing signs of the steering signal, but a peak signal at about 6 Hz to 7 Hz remains visible in the piezo voltage. The range of the piezos did not suffice to cover the range of motion of the test masses, which indicates a differential change in the arm lengths larger than 1 μm. The servo was designed with an integrator bandwidth of 3.3 kHz, unfortunately the transfer function could not be measured due to the occurring peaks, breaking the lock state.

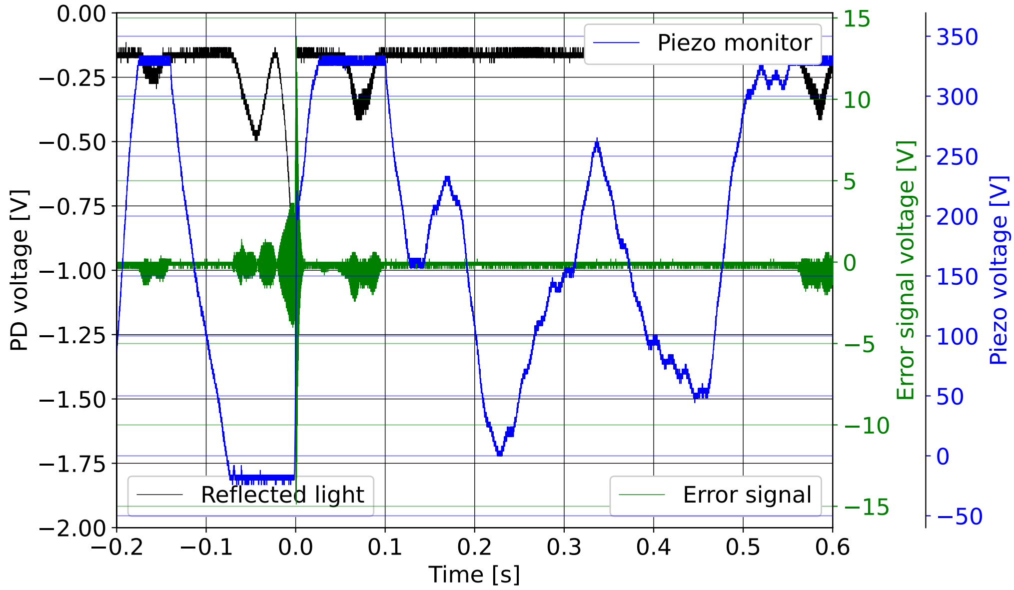

Figure 7.4: Michelson fringe with active lock. The movement of the test masses is counteracted by the piezos. To extend the range, both input mass piezos are used with opposing signs of the driver signal. The peaks in the PD voltage (black) occur, when the maximum range of the Piezos (blue) is reached. At these times the error signal (green) can not be held at zero. These can only be prevented by a greater seismic stabilisation or a further improvement of the piezo range. This measurement was made without arm cavities.

7.2 Arm cavities

The arm cavities are built with curved mirrors. The incoupling mirrors have a radius of curvature (ROC) of 15 meters. The end mirrors have a ROC of one meter, so that the arm cavities are stable under the condition given by equation 2.27, with a value of $g_1 g_2 = 0.0845$.

The arm cavities are independent from each other, but since they have nearly the same length, I used one modulator for both cavities. The EOM imprints 163.97 MHz sidebands on the light, before it enters the vacuum chamber. When the light passes the cavities, it accumulates phase, depending on the detuning. The sidebands can be detected behind the cavity with a resonant photo detector (RPD). Mixing the detected signal of the RPD of a length or frequency sweep across the cavity, with the modulation frequency, generates the error signal, that is needed to lock the cavity. The amplitude of the error signal depends on the frequency. A frequency must be inside the cavities linewidth to propagate trough it. This is also true for frequencies around a multiple of the FSR. So we can consider the error signal generated by a certain frequency depending on its detuning from the FSR. Coming from a far detuning the amplitude of the error signal increases as the modulation frequency approaches the FSR. When the modulation frequency reaches the FSR, the error signal rapidly shrinks until it vanishes on resonance. The reason is, that exactly on resonance there are no sidebands. The upper and lower sidebands, which create the error signal, coincide and cancel each other out. This allows to determine the arm lengths more precisely, than with actual length measurement tools, using equation 2.19. I sweeped the modulation frequency and measured the maximum amplitude of the resulting error signal. The frequency generator allows steps of 10 kHz, which limits the resolution. The result is shown in figure 7.5.

The measured values show the expected behaviour with the local minima at 163.9 MHz for the X arm and 164.04 MHz for the Y arm. This corresponds to arm lengths of 0.914 56(3) m and 0.913 78(3) m. For the error calculation I assumed half the width of the 10 kHz step size for the frequency error.

For a cavity the reflectivities of the mirrors are critical values, since they influence the nature of the resonator and its behaviour on resonance. The input mirrors used for the arm cavities are specified with a reflectivity of 99.7(1) % and a ROC of 15 m, while the end mirrors are highly reflective and have a ROC of 1 m. The two individual mirrors of incoupling and end mirrors are assumed to perform equally.

I measured the transmissivity of the mirrors to estimate the expected finesse of the cavities. For the end mirrors the result was a transmission of 4.0(2) ppm, where the error was estimated, since the dynamic range of the power meter was not sufficient. For the incoupling mirrors a reflectivity of 99.67(1) % could be measured. With the formula 2.17 this yields a finesse of 1898(58) in the lossless case. Using the manufacturer value of 99.7(1) %, the design finesse is calculated to be 2100(700).

To verify the cavities finesses and determine the loss, I ramped the lasers wavelength to scan the cavity. The resulting signal consists of peaks and their widths and distance defines how big the finesse is. Thus during ramping at least two peaks per half period are necessary, to determine a finesse value. Amplitude and frequency of the ramping is limited by the PMC, that can not follow arbitrary large wavelength changes. In the

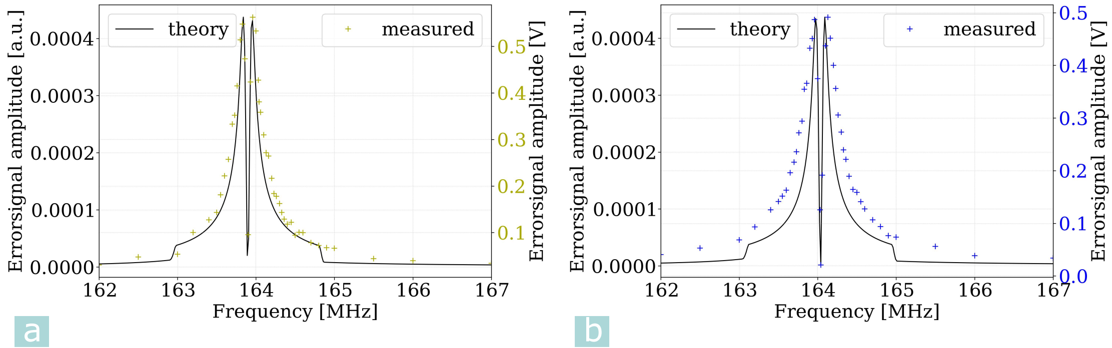

Figure 7.5: The amplitude of the detected error signal depends on the detuning from the FSR. a) X arm, b) Y arm. For modulation frequencies equal to $n \cdot \Delta\nu_{\mathrm{FSR}}$ the error signal vanishes. This allows to determine the FSR and therefore the length of the cavity. I used the measured peak amplitude to calculate the length of the cavities. Afterwards, I simulated a theoretical curve for the signal with this specified length and for the X arm they match well. For the Y arm, the measured width of the peaks is broader, than the theoretical curve, which might indicate, that the mirrors in the Y arm have a lower reflectivity, than the ones in the X arm, resulting in a lower finesse. The theoretical curves assume lossless cavities and reflectivities of 99.7 % and 99.9996 %.

evaluation process a time series of these ramps is divided into parts and the suitable ones are analysed for the finesse. The results for both arms are shown in figure 7.6.

The plot shows a kernel density estimation (KDE) of the distributed values. The values deviate and the real values can hardly be evaluated. It is imminent, that the X arm has a higher finesse, than the Y arm.

The point of maximum probability is 2180 and the mean value 2540. Both is higher than the theoretical value, which would mean the mirrors would have a higher reflectivity, then specified and measured on structurally identical mirrors. This means it is likely, that the finesse value is overestimated. For the Y arm the mean value is 1430 and the maximum probability is at 1330.

I used the finesse model to fit the measured curves more to the theoretical ones, where the round trip loss is the fitting parameter.

The result in figure 7.7 shows, that the Y arm loss of 2050 ppm is about four times higher, than the X arm loss with a value of 550 ppm.

To check the numerical values, a second approach was made.

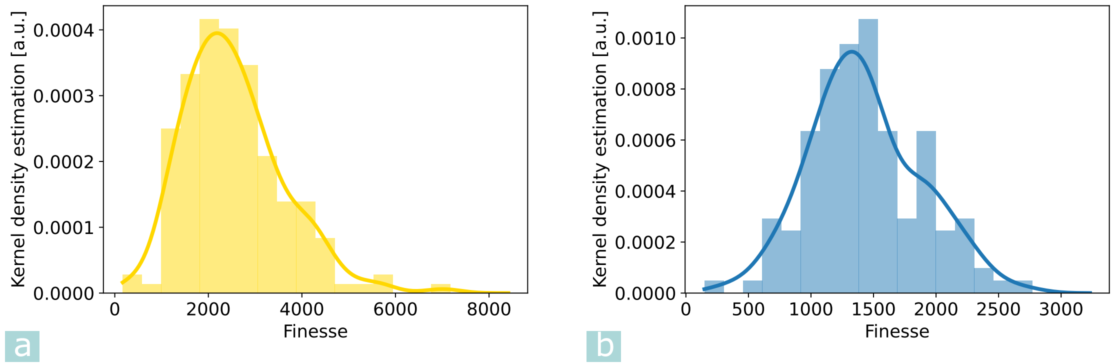

Figure 7.6: Scanning the cavity by ramping the wavelength is used to measure the FSR and FWHM linewidth. With this the Finesse is calculated and the results displayed in this KDEs. a) X Arm, Point of maximum probability: 2180, Mean finesse: 2540, b) Y Arm, Point of maximum probability: 1330, Mean finesse: 1430

In a simulation, I reduced the end mirror reflectivity, while keeping the incoupling reflectivity constant at 99.7 %. The resulting finesse was matched the maximum probability of the KDE, shown in figure 7.6. This resulted in loss values of about 1800 ppm for the Y arm and about 0 ppm for the X arm.

As previously mentioned, the finesse measurement is dependent on the ramping speed. A different measurement with a smaller ramping frequency resulted in a loss value of 500 ppm for the X arm and about 2000 ppm for the Y arm.

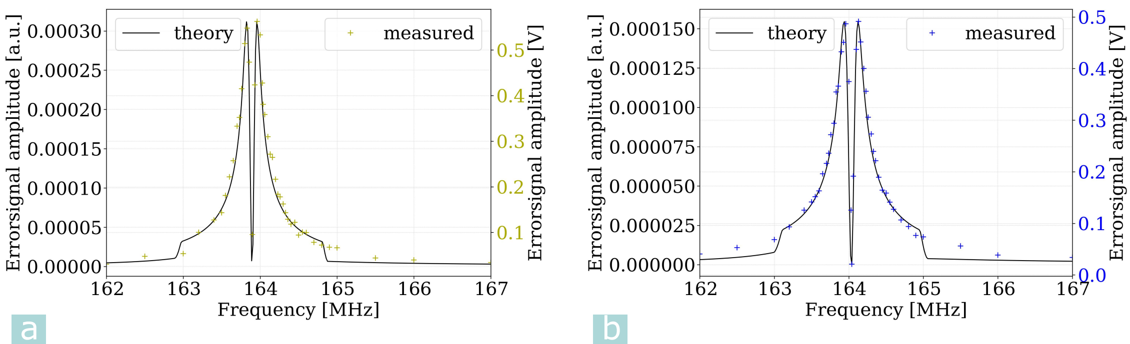

Figure 7.7: The cavity loss matched so that the theoretical curves and measured overlap. a) X arm with 550 ppm round trip loss, b) Y arm with 2050 ppm round trip loss

An opposing argument is, that the amplitude of the theoretical error signal maxima deviate by a factor of two, but the measured only by 14.5 %. Nevertheless a big difference in the round trip loss must be present, because the finesse of the Y arm is close to the theoretical maximum.

The origin of the loss is not known, but it can be assumed, that at least one dust particle on the surface of a mirror causes this loss. Even though the mirrors were cleaned, before the test masses were suspended, it was not possible to exclude the possibility of contamination. The idea of a clipped beam can on the other hand be excluded, since it would be noticeable during mode matching. Additionally, it would not alter the frequency dependency of the amplitude of the error signal.

Concluding, the loss of the Y arm is much higher, than the one in the X arm. Both cavities have a high finesse, roughly 1300 and 2000.

Using the reflectivities measured, no loss for the X arm cavity and equation 2.26 the power build up factor is 1207(37). This results in an intracavity power of 4.7(11) kW. Because of the loss, the Y arm reached only 400(29) W, assuming 2000(100) ppm of loss, while the X arm reached 1819(35) W, assuming 500(100) ppm of loss.

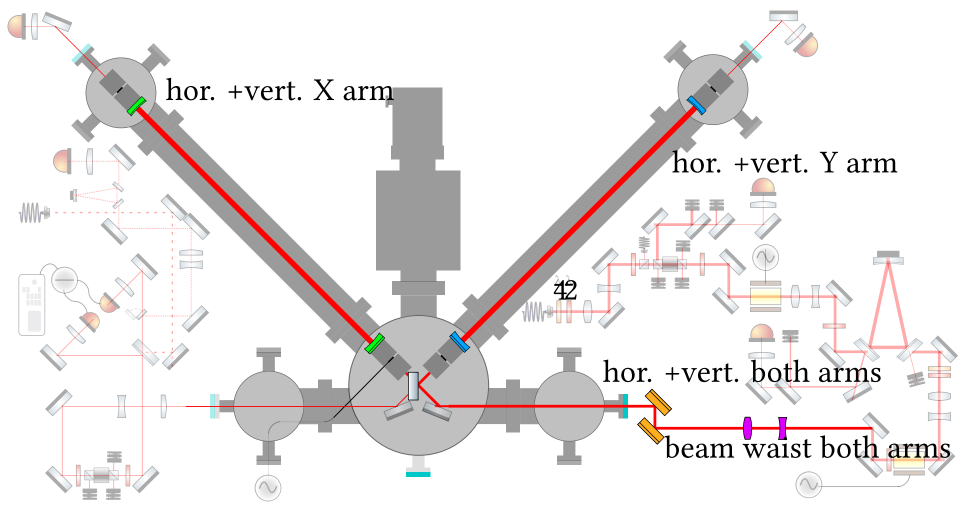

Figure 7.8: Setup overview with marked components for mode matching. The violet lens set adjusts the minimal beam waist size and position. The orange mirrors in front of the chamber are used to align onto the common mode of both cavities. The blue and green mirror sets are used to align the modes of the individual cavities.

The mode matching of the cavities must be done, using the optics in front of the interferometer for common misalignments and the cavity mirrors for remaining modes, which is shown in figure 7.8. In transmission of the cavity the modes can be measured, when the wavelength of the laser is ramped. The best mode matching measured this way for a single cavity was 99.1 %.

Adjusting the beam onto both arm cavities together is more complex, than onto one cavity, since the degrees of freedom are coupled. The beam pointing and position are not independent and the mirrors can be moved, but not tilted. Thus perfect matching for both cavities synchronously is challenging.

Additionally the mode matching unfortunately does not stay absolutely constant over time. Small drifts in the tilting of the optical table, thermal drifts and other minor effects tend to alter the mode matching up to a few percent over a period of days. A common mode analysis after readjusting, resulted in the plots shown in figure 7.9.

In this plot the main TEM_{00} mode is not shown, since it would disguise the smaller peaks. The X arm cavity shows a mode matching of 96.7 %, while the Y arm reaches 95.1 %.

Since values in the order of 99.99 % are possible, the values shown are not ideal, but more than enough to work on the lock, which only requires a dominant TEM_{00} mode.

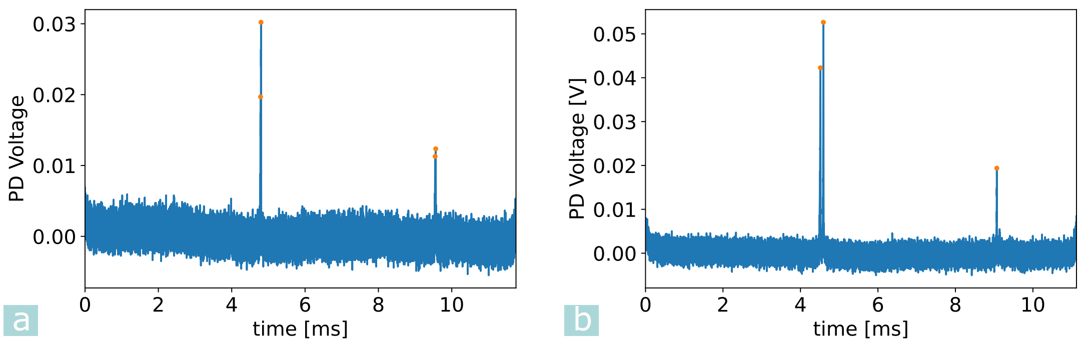

Figure 7.9: Mode matching measurement for the arm cavities. The ramped wavelength shows peaks of the modes in transmission of the cavity. The dominant TEM_{00} peaks are not shown. The mode matching of the a) X arm is 96.7 %, b) Y arm is 95.1 %

Higher values will only be necessary, once the cavities are stably locked and the Michelson fringe controlled to a dark output at the same time, which can be achieved by a realignment of the beam and readjustment of the cavity mirrors.

7.3 Arm cavity lock

The error signal, explained in the last section, is shown in figure 7.10. The comparison shows, that it follows the theoretical curve. For the transmitted light it is a Lorentzian peak and for the error signal a single cycle oscillation, centred at the peak position.

The time series of measured values was converted into phase values, using the finesse, which are presented in chapter 7.2. The knowledge of the cavities finesse allows to determine the linewidth in terms of phase.

The arm cavities are, generally speaking, two independent systems. They share the same optical wavelength and use the same modulation for the error signal, but the mirrors and actors move independently from each other. The piezos in between the tungsten blocks are used, among others, to lock the cavities. One possibility is, to use one or both piezos per cavity, to counteract to mirrors movement and lock the cavity onto resonance. This did not work, since the movement exceeds the maximum range of 1 µm of both piezos combined. Thus, I implemented an altered version of the Pound-Drever-Hall technique. It is shown in figure 7.11 [53].

Instead of locking a laser to a stable cavity, thus reducing wavelength noise, the moving cavity causes more wavelength detuning as a parameter to keep the cavity on resonance. In transmission from both arm cavities RPDs detect the light, that passes on resonance, including the sidebands at 164 MHz. Mixing these signals with the identical modulation frequency together with frequency filters results in the error signal.

Mixing is a multiplication of two signals, which can be expressed with the addition theorem

$$\sin(\alpha)\sin(\beta) = \frac{1}{2}\left(\cos(\alpha-\beta) - \cos(\alpha+\beta)\right). \tag{7.2}$$

That means the output is a superposition of two different parts, one with the difference frequency and one with the sum of the frequencies. For the LO and the signal frequency coinciding, one receives a term dependent of the doubled frequency and a constant DC term. A low pass filter, which filters the doubled frequency, leaves the constant term. The information about the detuning is not lost in the process.

A PID controller for each channel processes the error signal to a control signal. The control signal of the first cavity is fed back onto the laser for actuation on the wavelength.

The control signal of the second cavity is applied to the piezos, after it was fed to four HV amplifiers, of which two are coupled to an upstream inverter. The not inverted but amplified signal is connected to the piezos of the second cavity and counteracts its detuning. The inverted and amplified voltage is connected to the piezos of the first cavity. Thus, the first cavity approaches the detuning of the second cavity. The laser still follows the resonance condition of the first cavity and ultimately both cavities are on resonance.

It was not possible to combine the Michelson fringe dither lock with both arm locks yet, because of the noise in the arm locks. Nevertheless the dithering must be counteracted to lock both arms simultaneously. For this the dither signal must be inverted and applied to the second piezo of the cavity. The piezos act with different ranges, even when driven with the same signal, because of small variations in the preload and thickness of the Peltier elements and copper pieces of the different test masses. This makes it necessary to scale the signal, when feeding it to the second piezo.

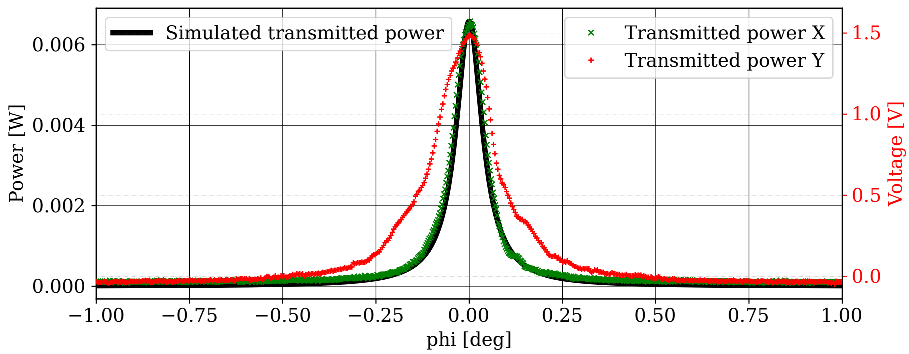

a

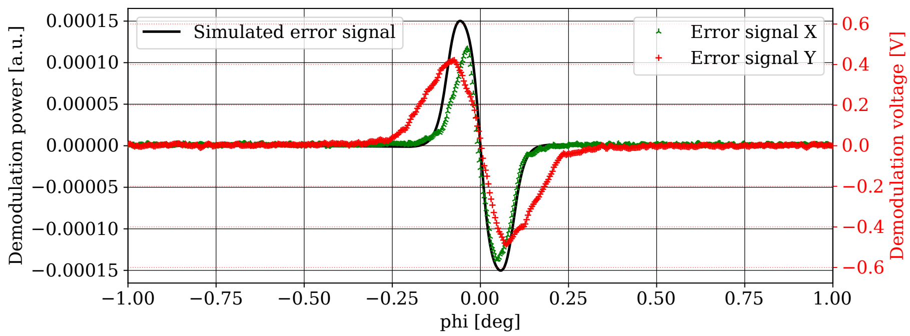

b

Figure 7.10: Comparing the theoretical and measured signals. In the simulations the power is normalised to the input power of the interferometer. a) The light transmitted through the end mirror, when the cavity passes a resonance. b) The error signal in transmission of the cavity is a single oscillation cycle around the transmission peak. The zero crossing is simultaneous with the peak. The measured behaviour fits well the theoretical simulation. The modulation frequency is 163.96 MHz and thus close to the middle between both FSRs. The time series was converted into phase values, using the finesse values evaluated in chapter 7.2

.

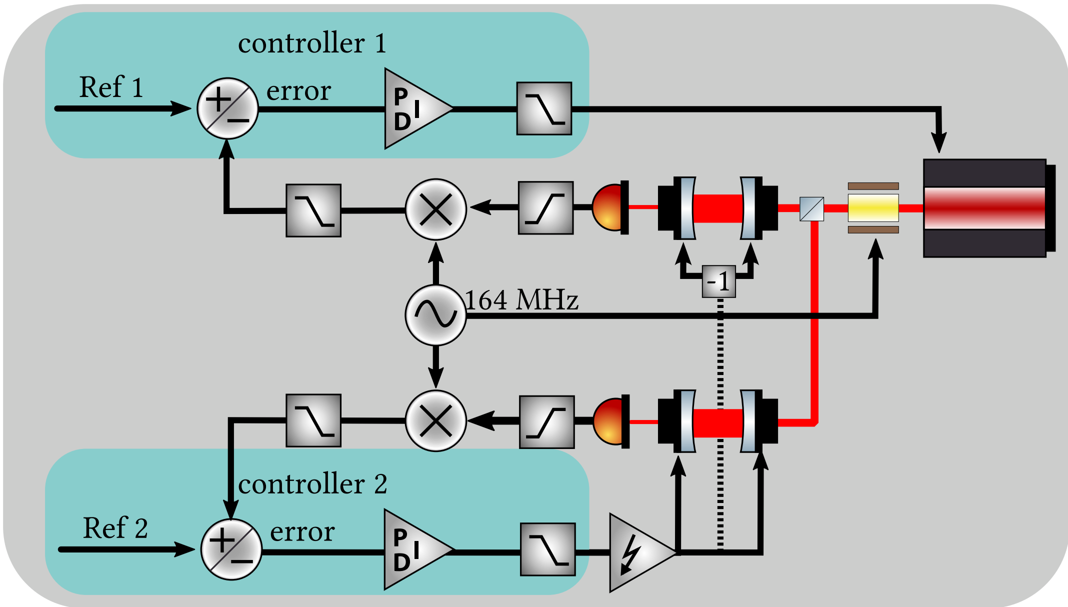

Figure 7.11: The locking scheme for the arm cavities. The EOM imprints modulation sidebands onto the light field, that are resonant in the cavity. In transmission from both arm cavities RPDs detect the light, that passes on resonance. Mixing these signals with the modulation frequency together with frequency filters results in the error signal. A PID controller for each channel processes the error signal to a control signal. One control signal is fed back onto the laser, so that an altered version of a Pound-Drever-Hall technique is realised. The other control signal is applied to HV amplifiers and afterwards to piezos, connected to the mirrors [53].

In the graphic 7.12 the blue and black trace are the voltages of the two RPDs in transmission of the cavities. Both cavities can individually be locked, using the laser. The used locking scheme for this measurement added the error signals of both cavities, which causes the jumps between the cavity locks. It was only used once to determine if both cavities can be locked in general.

As visible the arm cavity on resonance shows noise, which is shown in figure 7.13. The noise is approximately frequency independent from 1 kHz to 20 kHz, before it shrinks with about −60 dB per order of magnitude.

While no measurement is free of noise, it is very uncommon for the power to drop by values of 50 % or less of the maximum/minimum value in the noise peaks, while in a closed loop. As possible reasons for this, I examined in-air distortions and density fluctuations,

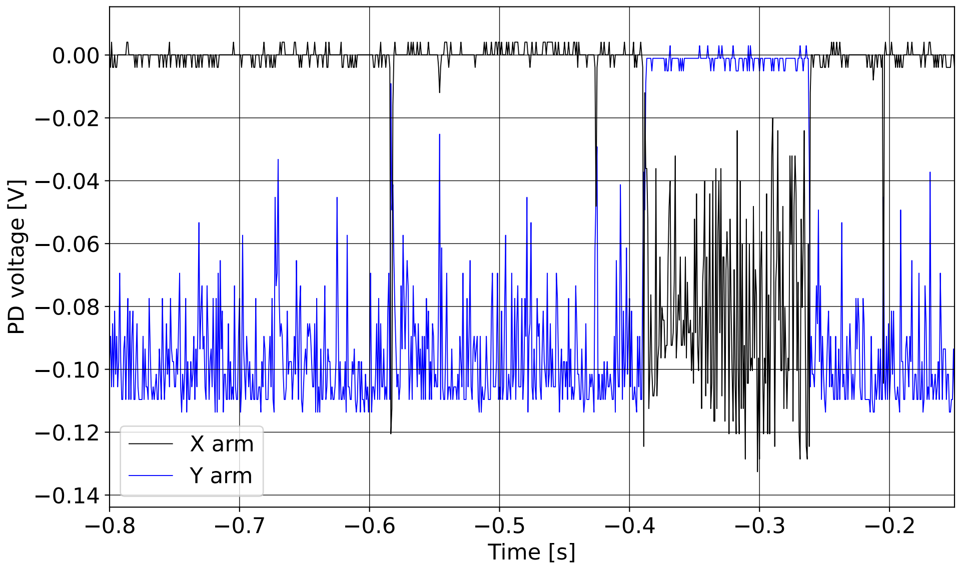

Figure 7.12: The traces show the voltage of the PDs, which are directly proportional to the optical power. The detector measures the power in transmission of the arm cavities. In the state of a closed loop, the laser wavelength is controlled, so that the cavity stays in resonance. The noise visible indicates, that the cavity is not kept well on resonance, but fluctuates around it, without necessarily falling out of the loop. The lock switches intentionally between the arms at about t =−0.4 s and −0.25 s and both show the same behaviour.

as these measurements were made without vacuum conditions in the chamber, and noise on the laser light itself.

I re-established the vacuum conditions in the order of 10^{-6} mbar and measured the noise in transmission from the cavity again, which turned out to be similar and thus falsified the theory of in-air distortions being the cause of the noise.

To determine the noise of the laser, I used the PMC, which gives the opportunity to detect amplitude and phase noise. In reflection from the incoupling mirror the PD detects the light power. When the PMC is adjusted well on resonance and with a good mode matching, the reflected field can be used to gain information on the amplitude noise of the laser, since frequency noise is suppressed. To measure the frequency noise of the laser the PMC is tuned to mid-fringe, where a small change in the frequency leads to a large change in power.

The result, shown in plot 7.13, is that amplitude noise is much smaller than frequency noise. Both noise sources have their own specific features. The amplitude noise shows an overall low level with a peak at 2 kHz. The frequency noise has recognisable ripple features in the region from 200 kHz to 700 kHz. These were also found by Dr. M. Korobko [30] and are features of the NKT laser.

The spectrum of the cavity transmission shows none of these features, but two peaks around 50 kHz and 80 kHz. This suggests, that the noise has another origin. The most probable reason is the feedback loop, which can not counteract the distortions accordingly. Different approaches were chosen to create a functioning feedback, resulting in a locked state. None of these could prevent the noisy output.

As an alternate source also radiation pressure was taken into account. The force applied to a lossless mirror under normal incident by radiation pressure is

$$F = \frac{2P}{c} \tag{7.3}$$

with the intracavity power P =1.8 kW this yields 6 µN. Constructing a force triangle with the gravitational force and the radiation pressure force as its legs, the angle of displacement that forms is 0.1 µrad. And with a wire length of 5 mm the total displacement is 0.5 nm per mirror. The effect occurs for both mirrors simultaneously and altogether the displacement is 1 nm. This is much smaller than the wavelength, but since the light is making more than one round trip and both mirrors experience this displacement, it is more than enough to push the mirrors off the resonance. The theoretical linewidth is 80 kHz for the given cavities in the lossless case. Analogous to equation 2.18 we can define a length change, that is within the linewidth of the cavity. It is given by

$$\Delta L = \frac{\lambda}{2\mathcal{F}}, \tag{7.4}$$

which yields 0.775 nm in our case. That means the radiation pressure can indeed distort the cavity resonance. Whether that is the cause of the transmitted noise is not yet clarified, but it would not explain why the feedback loop is not capable of cancelling it. At least the noise below the unity gain bandwidth should be cancelled. Additionally, measurements with different input powers were made, that all had similar outcomes, while the influence of the noise should vary with the power, if the radiation pressure noise was the origin.

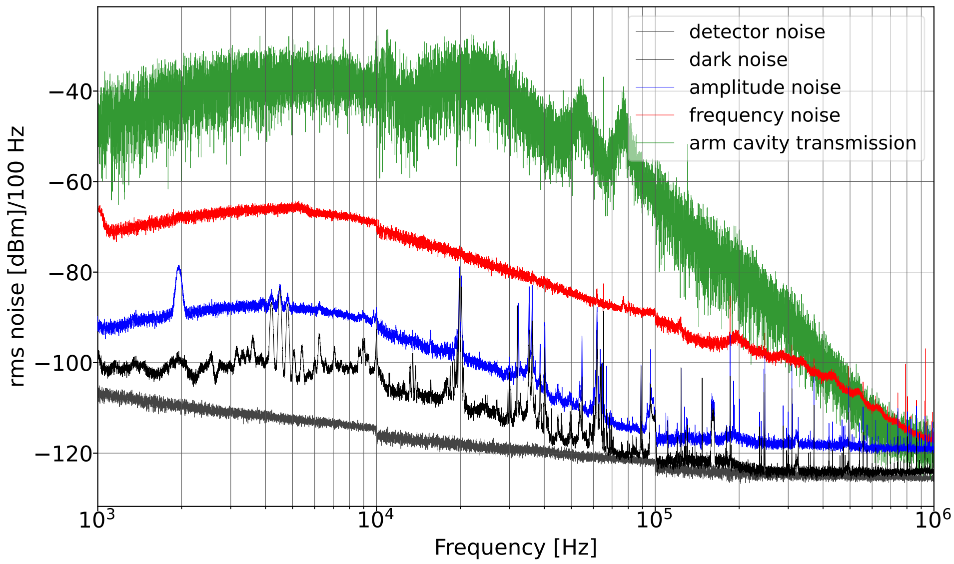

Figure 7.13: The arm cavity noise compared to the noises of the laser. The amplitude noise shows an overall low level with a peak at 2 kHz. The frequency noise has a much higher level, but has recognisable ripple features in the region from 200 kHz to 700 kHz. The spectrum of the cavity transmission shows none of these features, but two peaks around 50 kHz and 80 kHz.

Different controller schemes were tested. The first design consisted of a 0.8 kHz integrator and a proportional gain. It worked also with an integrator corner frequency of 2.4 kHz, but was less stable. The transfer function for this design is shown in figure 7.14. The unity gain bandwidth is about 7 kHz in both cases.

A different approach used three differentiator stages, an integrator and a low pass filter and was tested with various corner frequency combinations, but none was able to eliminate or suppress the noise significantly.

That there is a kind of lock, meaning a stable state, that the controller maintains, is proven in figure 7.15. The light power on the PD never vanishes, as would be expected in a random, unlocked, state. Additionally the control signal, which determines the wavelength detuning, follows the movement of swinging test masses. The signal is a beat between two close frequencies, which meats the expectations. Thus there must be a kind of locking.

A different effect was observed during these measurements. There are at least two different locked states, that were observed during the improvement of the lock. One

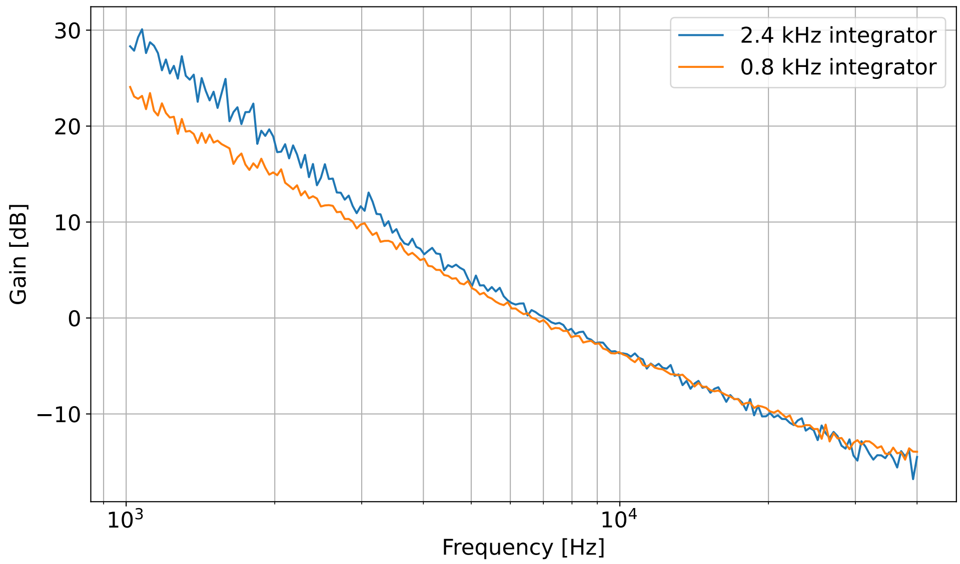

Figure 7.14: Open loop transfer function of the arm locking servo for two different integrator corner frequencies. The unity gain is about 7 kHz in both cases.

state can be described as a fluctuation around the resonance, so that the amplitude is close to the maximum transmission. The second state seems to operate on a slope of the resonance, because the voltage on the transmission diode stays close to half the maximum. The lock sometimes changes the state it is in, without falling out of lock. The reason could not be determined. In the figure 7.15 this is visible as different levels of minima in the PD voltage.

As previously mentioned the piezos act with different ranges, which must be accounted for. In figure 7.16 the noise spectra of the PD in transmission from an arm cavity is shown. To monitor the spectrum, the cavity was locked. The curves prove, that the dithering can be counteracted in a way, that both mirrors dither equally.

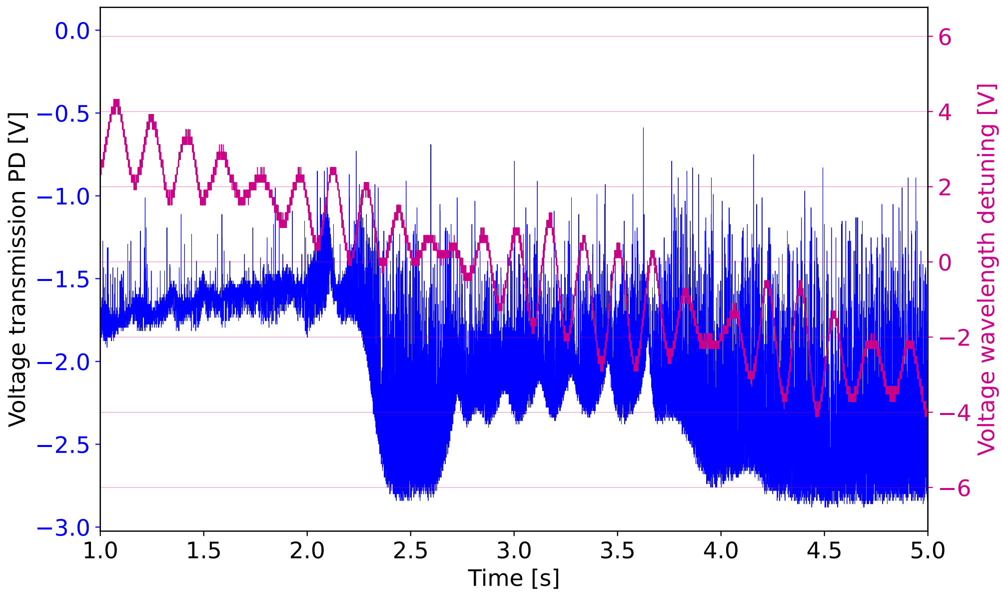

Figure 7.15: Time series of light power behind the arm cavity and the laser control signal. The amount of light on the PD (blue trace) changes between two lock states. First the cavity is detuned, so that half the maximum is transmitted. Then it changes to the state, in which the cavity is close to resonance. The laser wavelength tuning is shown in the violet trace and the beat between both pendulum frequencies is visible. The wavelength is tuned to follow the resonance condition, which is equal to a locked state.

Even more importantly this measurement also shows, that it is possible to create a locking state, while the mirrors of the cavity are dithering, which is crucial for future operation.

It was indeed possible to lock both arm cavities together. The traces are shown in figure 7.17. One cavity is kept on resonance, using the laser, while the piezos keep the other one locked.

Summarising the chapter it was possible to lock the arm cavities individually and simultaneously. To combine the arm locks with the interferometer dither lock it is necessary to improve the stability of the arm cavity lock, by eliminating the origin of the noise.

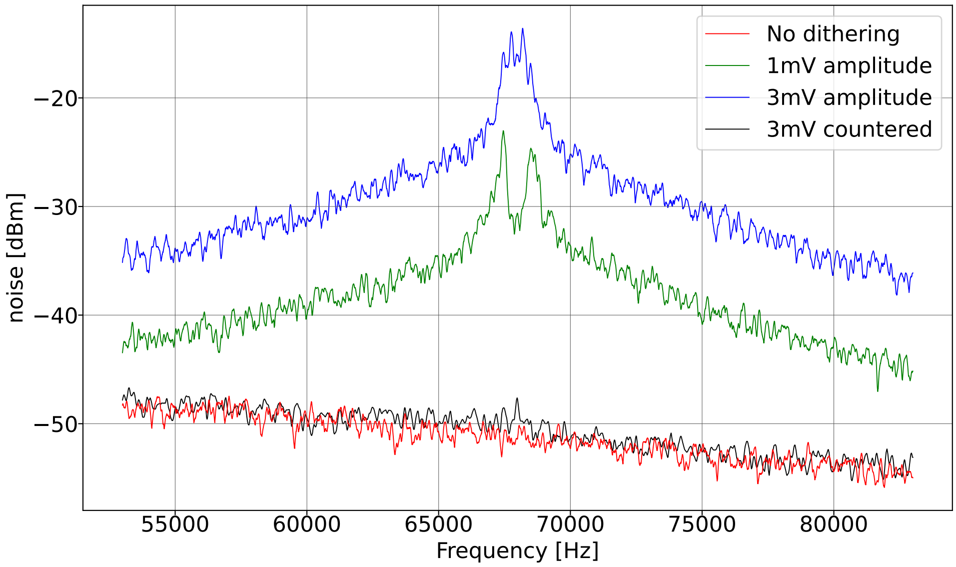

Figure 7.16: The dithering signal is inverted, scaled and fed to the second mirror. This makes both mirrors move simultaneously, which allows the cavity to stay on resonance. The amplitude is measured before being fed to the HV amplifier, which magnifies the signal by an approximate factor of 10.

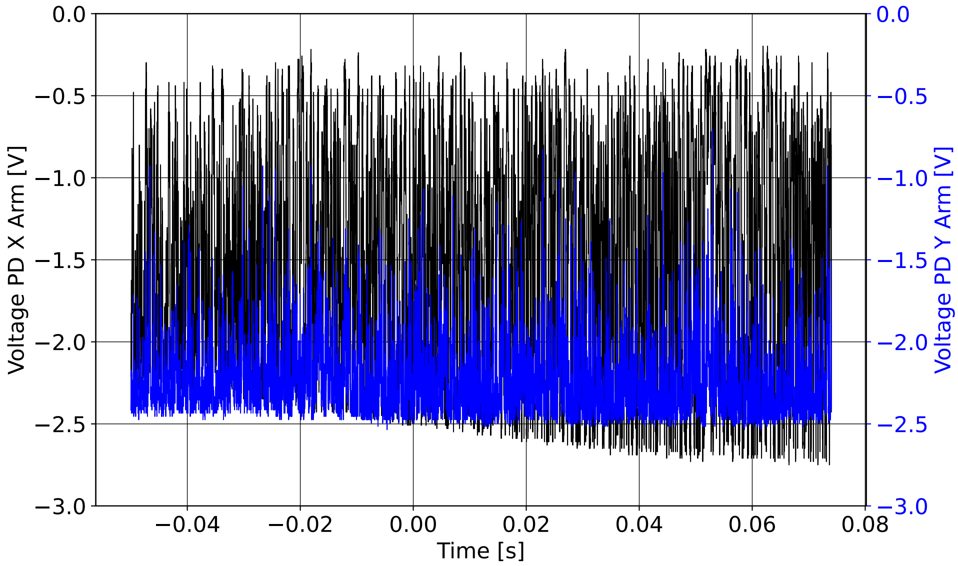

Figure 7.17: The transmitted power of both cavities. Both are kept on resonance simultaneously. The Y arm in blue shows less noise amplitude, thus can be concluded, that the feedback loop might perform better, than the one of the X arm. A different, but related explanation could be, that the scaling of the piezo gain is not optimal.

7.4 Pendulum frequency measurement

Using the altered Pound-Drever-Hall technique, I locked the laser to both cavities individually and analysed the tuning of the laser frequency. A Fourier transformation of the time series gives information about the most participating frequencies. That should give information about the swinging frequencies of the test masses and thus their pendulum lengths. The power spectral density (PSD) of the data is shown in figure 7.18. The used measurements were about three minutes long.

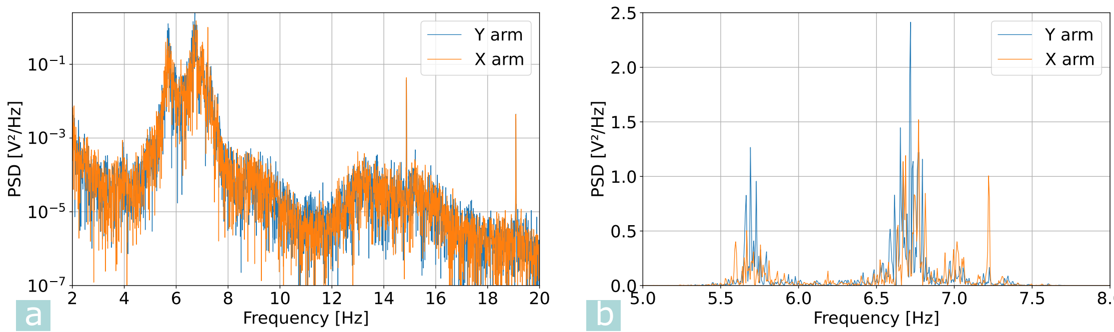

Figure 7.18: Power spectral density of the cavity control signal for both arms. a) Overview, b) detail view. The Y arm shows resonances around 5.7 and 6.7 Hz. The X arm has its most participating frequencies around 6.7 and 7.2 Hz.

Generally both curves look very coinciding. On the logarithmic scale, both arms appear to have their resonances at 5.7 Hz and 6.7 Hz. If this is coincidence, has its origin in an unknown dynamic of the control system, or has different unknown reason could not be identified. In the linear detail view the peaks differ slightly for the arms.

The Y cavity shows high resonance peaks at 5.7 and 6.7 Hz, which corresponds to 7.6 mm and 5.5 mm long wires.

The X arm has its highest peaks around 6.7 and 7.2 Hz. That means the wire suspension wires are 4.8 mm and 5.5 mm long.

Since this method can only determine the effective length of the pendulum, the two individual wire loops per test mass may still vary in length.

The amount of spikes in the linear detail view and the noise in the logarithmic view suggests, that not all peaks derive from own modes, but may be part of the noise.

Other modes of the pendulum might also appear in this graphic, although they have not been precisely identified. The yaw mode of the test masses, calculated with equation 5.3, is just 0 % to 15 % higher, than the pendulum mode. This range is a result on the assumption, that the angle of the wires is between 0° to 45°. This means the 7.2 Hz peak of the X arm could be the yaw mode of a test mass, whereby the length of a wire loop would correspond to one of the other similarly high peaks. It was not possible to precisely determine this.

The pitch mode can be expected to be much higher, in the kHz region, because tungsten, the wire material, has a high tensile strength. And since the test mass rest in two wire loops the stretching of the wires would be essential for the pitch mode.

7.5 Interferometer characterisation

After locking the arm cavities, the interferometer must be locked. The interferometers performance depends on good alignment, mode matching and control loop performance. To be more precise the two arm cavity control loops and the interferometer control loop, which determines the fringe and that can only be operated simultaneously once the arm cavity control cancels the noise.

As a first indicator the central BS is set up to split the power as balanced as possible. The best splitting ratio achieved was 49.5 % (reflection) by 50.5 % (transmission), which is close enough to the optimal case. The reason of the deviation is, that the optimal angle of incidence for the given BS would be smaller, but the optical windows at the end of the arms limit the range.

7.5.1 Contrast

A crucial property of an interferometer is its contrast. This figure indicates the visibility of a phase change between the interferometer paths. Thus the interest of a good contrast is high. It is calculated with equation 2.15 and therefore is a value between zero and one but often specified as a percentage value. To reach a perfect contrast the two beams superposed on the beam splitter must have equal modes. Small differences in the alignment or paths lengths will lead to residual modes, that lower the contrast. These could be, that the beams have different positions, directions or diameters on the beam splitter. The alignment suspension allows to control the motors and the beam alignment even under vacuum conditions and thus the interferometer contrast.

M. Faden and I set up the input test masses with highly reflective mirrors and a radius of curvature of 1 m as an interferometer and tested the applicability of the suspension. The mirrors were placed like they would face the arm cavities and thus the conditions were similar to later use cases.

To detect and monitor the contrast, for testing we placed a PD behind the output of the interferometer, which detects the light power. Detecting the contrast makes it necessary to see the extreme values of the interference, but a mechanical excitation of the pendulums might distort the alignment and the beam directions. I applied a sine voltage from a frequency generator to the HV amplifier of the ring piezo in one test mass and thus created a periodical phase shift with a constant amplitude in the direction beam propagation. We ramped the frequency and for a value close to 4 kHz a mechanical resonance of the test mass leads to amplitudes of mare than a half wavelength. With this we can detect the extreme values of interference at all times. The PD is read out with an *Advantech* data acquisition card and the data processed with a self written python code. The coding done to automatically evaluate the interferometer contrast was part of M. Faden's Thesis. More details on the movement of the motors and the contrast can be found in [56].

Before the alignment started, we measured the dark noise of the PD. Afterwards, we sent the light on the PD and a time series of values is written into a file. The algorithm finds peaks in the series, subtracts the mean value of the dark noise and calculates the contrast values for all pairs of neighbouring peaks. After we moved a motor we start a new measurement and the contrast is updated.

In figure 7.19 a one millisecond section of the light on the PD is shown. The first local minimum at 0.05 ms marks a turning point of the piezo. Until approximately 0.45 ms the piezo moves in one direction, before reverting its movement. Thus the global maximum at 0.15 ms and minimum at 0.3 ms represent P_{min} and P_{max} from the equation 2.15 for the contrast. The local minima and maxima, caused by the turning points, lead to incorrect contrast values, since they are compared also to their neighbouring extrema.

To determine the contrast the algorithm calculates values for all neighbouring maxima and minima. Since electronic noise can never be completely prevented, there are fluctuations around the true value. When the contrast is close to one, the minimal power must be very small. Since the dark noise can only be subtracted as a mean value, it is possible, that the measured value for $P_{\min}$ fluctuates below the dark noise. This causes contrast values higher than one. The data processing must take this into account and average the fluctuations.

Firstly we decided to take the mean value of the highest five percent of values as the contrast, to eliminate this influence. This arbitrary filtering delivered values close to, but also higher than one. This result is non-physical and thus we changed our value estimation.

We decided for the first algorithm to bin the values in a histogram, which resulted in two peaks. One is centred around zero and the other at the true contrast. The peak close to zero is an artefact, originating from the turning points of the modulation. Therefore contrast values below 1 % were dropped from the data. The same was true for values larger than 1.01, since these are non-scientific and barely occurred.

The outcome of this method is highly dependent on the binning. For an example I binned a data set with a changing number of bins and the output was always different. The result is shown in table 7.1 and compared to the expectation value of a Gaussian fitted to the peak in the histogram.

Bins	contrast (highest count)	contrast (fit)
100	0.982272	0.994532
101	0.972646	0.987095
1000	0.997828	0.999333
10000	0.998606	0.999339
10010	0.999950	0.999315
100000	0.999151	0.999328
101000	1.000023	0.999328

Table 7.1: Different binning leads to altering positions of the highest count. A Gaussian fit applied to the peak and taking the centre value is above a certain threshold barely depending on the binning and thus more reliable.

I improved the method used in M. Fadens thesis by using the Gaussian kernel density estimation (KDE). A Gaussian fit can improve the value estimation, also shown in the binning table. This would make an assumption about the distribution of the values, which is not justified. The KDE method is used to estimate the probability density function (PDF) of a random variable [76] and makes no prior assumptions about the distribution. The

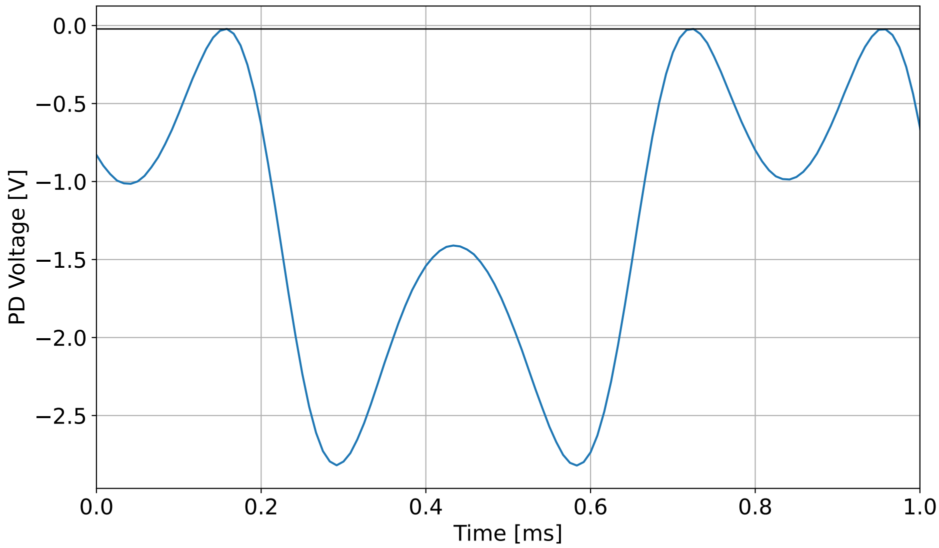

Figure 7.19: Contrast measurement, the modulated piezo leads to turning points. When automatically identifying the peaks and their height all points are taken into account. From the maxima and minima the contrast is calculated. The black line indicates the dark noise of the PD. The voltage values from the turning points are in between the maxima and minima, so that the difference between them and the extreme points is lower. This causes arbitrary values and washes out the distribution of values. Even values close to zero appear, but are of no significance.

result is dependent on the used estimator, which defines the bandwidth of the Gaussian. For too small bandwidths the result would be rough with artefacts of the data. Too high bandwidths on the other hand smoothen the distribution too much and disguise it.

After the standard estimators of the python *scypi* package proved a Gaussian shape of the distribution, I fitted a Gaussian of the form

$$f(x) = A\frac{1}{\sqrt{2\pi\sigma^2}}\exp^{\left(-\frac{(x-\mu)^2}{2\sigma^2}\right)} \tag{7.5}$$

[77] to the resulting PDF to receive the expectation value and standard deviation.

I displayed the result of different bandwidths estimators and covariance factors in table 7.2. Plotting the PDF it shows significant similarities with a Gaussian curve, so that I fitted on to the PDF, to get the expectation value and standard deviation. This is presented in figure 7.20, where also a binning example is shown for the same dataset as comparison. The binning might not be presented correctly in generated figures, which leads to wrong results. The Gausssian fit to the binned values is less fluctuating, but assumes a certain type of distributed values. The KDE based PDF of the measurements results in the least biased and thus most reliable values for the contrast. The afterwards fitted Gaussian to the PDF provides information about the expectation value and width.

bandwidth estimator(covariance factor)	Expectation value	standard deviation
Scott (0.146)	0.995	0.054
Silverman (0.154)	0.995	0.057
0.0005	0.9993	0.0019
0.001	0.9993	0.0019
0.002	0.9993	0.0021
0.005	0.9992	0.0028
0.01	0.9991	0.0044

Table 7.2: Using kernel density estimation, the expectation value and standard deviation can be identified without the dependence on binning.

Comparing the smoothness of the PDF and the Gaussian, I estimated the optimal value for the PDFs covariance factor to be the smallest value, where the PDF is still a Gaussian and has no artefacts yet. This was the case for a covariance factor of 0.002.

The contrast values above one occur, when the voltage during a local extreme transcends the mean value of the dark noise. Since we measured and averaged the dark noise before the contrast measurement, drifts and instantaneous fluctuations in the electronics can cause these transitions. When the algorithm calculates with these values, the subtrahend is negative, leading to a contrast higher than one.

Reviewing the dataset from M. Faden he used to determine the contrast we could reach, his evaluation gave a value of 99.7 %. I can now say it is 99.93 % and thus much closer to 1.

Concluding I can control the contrast of the interferometer and reach values higher than 99.9 %. Additionally the contrast can be measured, analysed and displayed semi-automatically.

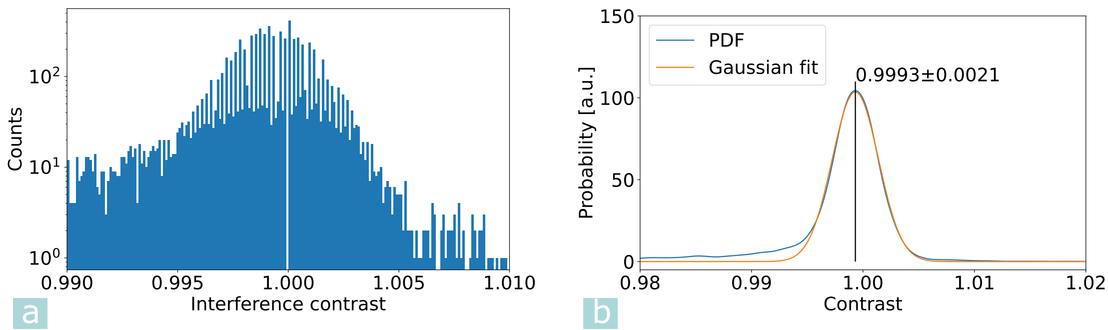

Figure 7.20: Comparing the script results. a) Histogram with binned values. The output value of 99.86 % is not visible as the highest count number in the plot. The value seems to be arbitrary. b) PDF and Gaussian fit of the contrast measurement. The centre of the distribution is well defined and visible. The value of 0.9993(21) proves, that high contrasts can be achieved, using the alignment suspension.

8 Conclusion & Outlook

8.1 Conclusion

The goal of the long-term project is to create a Michelson interferometer with arm cavities, power recycling and resonant sideband extraction, that is combined with squeezed light states, following the Einstein Telescope high frequency design. I set up a compact one meter Michelson interferometer with suspended test masses and arm cavities in a table top experiment. Each test mass is made up of two tungsten blocks weighing 3 kg each. In between these a piezo and two Peltier elements allow for an active length change for high and low frequency distortions.

I designed a suspension structure, that contains three piezo motors. The first design was tested, the performance analysed and afterwards upgraded to one with shorter wires, which drastically decreased the seismic excitations. With this upgraded structure the test masses can be moved vertically and horizontally, which allows beam steering with sub-micro radian precision, since the mirrors have a curvature. This allows mode matching and contrast improvement even in a closed vacuum chamber. Using this structure, I achieved contrast values of 99.93 %, which can be monitored semi-automatically.

The target, to measure on the shot noise level, requires a stable fringe position. With the suspended mirrors I achieved a fringe lock on basis of a dither lock, which needs no Schnupp asymmetry. The dither lock uses a build in piezo to create a vibration with known frequency and the light reflected from the interferometer is used to create the error signal, stabilising the Michelson fringe. As shown in chapter 7, the lock counteracts the movement of the masses, but is not able to prevent peaks, when the swinging amplitude is larger than a few hundred nano meters. Other piezo elements with higher range are needed to finalise the lock.

The sensitivity of a Michelson interferometer to length changes is dependent on the light power in the arms. The mirrors installed form two arm cavities in the Michelson interferometer, which have a finesse of about 1300 and 2000. The difference is explained by optical loss, which is about 2000 ppm for the Y arm and 500 ppm for the X arm. This results in circulating powers of 400 W and 1.8 kW, which I presented in chapter 7.2.

This allows for a theoretical sensitivity in the order of $1 \times 10^{-20} \frac{1}{\sqrt{\mathrm{Hz}}}$. The arm cavities are monitored by resonant circuits and can be held on resonance, using control loops. One arm cavity is locked onto the laser, using an altered Pound-Drever-Hall technique. The laser wavelength is changed accordingly, to fit the length of the moving cavity with a unity gain bandwidth of about 7 kHz and gain of 30 dB at a frequency of 1 kHz. The second cavity is stabilised, using all four piezos in all test masses. The piezos of the second cavity directly counteract the detuning, while the ones in the first cavity act in the opposite direction, which causes the laser to change its wavelength towards the second cavities resonance.

I achieved a simultaneous lock in both arm cavities. The lock states show noise in transmission from the cavity. That noise was analysed and air distortions can be discarded as a possible reason, since the noise is present under vacuum conditions. No hints were found, that the amplitude or phase noise of the laser are the origin for the noise either. Several controller configurations were tested, but the noise could not be eliminated. Once this is managed, the combination of both arm and dither locks would be possible, allowing for a first sensitivity measurement at the dark fringe.

8.2 Outlook

In this section I provide possible improvements for the prototype, to increase its testing capabilities of GWDs.

The most important improvement I would suppose, are piezo elements with higher range. These would directly improve the dither locks capability to counteract test mass movement and stabilise the fringe better against excitations. Since the position in the centre of mass is beneficial to prevent excitations and thus should not be changed, the range is the favourable parameter to change.

Especially regarding the future stabilisation of recycling cavities and the dark fringe lock, an improved arm cavity lock is needed. For that it is necessary to identify the noise source. Since the laser noises and controller were already investigated, the involved RPDs might be considered a potential cause.

Regarding the dark fringe it will at one point be necessary to open the vacuum chamber and clean the cavity optics, to eliminate the loss in both arms. If this would not help, the faulty optic needs to be identified and exchanged. Unless both cavities perform similarly well, the power reflected back to the BS is different and no dark output is possible on resonance.

The active seismic isolation is a good improvement, but yet is only controlling the horizontal translation of the concrete block. In the experiment the test masses are still being excited by seismic movement, which are strong enough to cause distortions of the dither lock, as seen in chapter 7, thus it might be beneficial to also account for the tilt of the block to further decrease the amplitude of the seismic noise.

To reach higher light power, better sensitivity and have a more realistic model of the Einstein Telescope, it will be necessary, if also not easy, to add a dual recycling, consisting of power (PR) and signal recycling (SR) or resonant sideband extraction (RSE). PR is a technique, where another mirror in front of the Michelson interferometer is added. This mirror reflects the light, which is back-reflected from the interferometer. So a cavity is formed, where the power recycling is the incoupling mirror end the two arm cavities act as one end mirror. This requires a stable lock on the dark fringe, but allows for higher power inside the arm cavities. A higher finesse in the arm cavity would result in a higher loss through the arms end mirror, since the state would get closer to an impedance matched cavity. To remain an over-coupled cavity, the light power can be increased only by more power from the laser or another mirror, which imitates the effect.

Since the signal for the arm cavities must couple through the power recycling cavity first, I simulated if that would still work. The result is, that the already chosen signal frequency around 164 MHz does pass the power recycling cavity, allowing the arm cavities to be locked nevertheless.

SR and RSE are techniques, that use a mirror behind the output. Simplified, signal recycling operates on resonance, the RSE on anti-resonance. While RSE lowers the reflectivity of the input mirror for the signal frequencies, SR increases the time of the signal in the interferometer and increases the signal on cost of the bandwidth [15].

This adds also two degrees of freedom to the system, that require an extension of the locking scheme.

Also it could be tested if a cavity, as proposed by Khalili, might be used in the place of the recycling mirrors. This would allow for mirrors with tunable reflectivity, depending on the cavity tuning. [34]

The squeeze laser, that shall reduce quantum noise, was built by Pascal Gewecke during the period of his Doctoral Thesis and has proven to deliver more than 10 dB of squeezed light [55]. Implementing this will improve the shot noise.

Acknowledgements

On this page I want to express my gratitude towards the people, that helped me directly and indirectly to write this thesis.

First of all, I want to thank Prof. Dr. Roman Schnabel for the opportunity to work on this topic as part of his group. Ever since I started my masters thesis and all way through until the end of my doctoral thesis, I enjoyed the heart warming atmosphere of mutual helpfulness in the group. In this sense a warm *thank you* to all (prior) colleagues in the group, that made this such an enjoyable experience.

Special thanks go to

Prof. Dr. Oliver Gerberding for his additional supervision, help and tips.

Prof. Dr. Katharina Isleif for our meetings, always having an open ear and the mentoring in general.

My parents, who helped me to pursue my interests.

Heike for her loving support.

Dr. Mikhail Korobko, for helping and explaining whenever it was necessary.

Dieter for his help to get everything running safely.

Maximilian for his work and help during his masters thesis. Additionally for mutual motivation in a hard time to go to the lab and continue working.

Leif for his interested questions and mutual brainstorming about the project.

Alex, Benedict, Julian, Maik and Pascal for the fun evenings and sessions all through the years.

Linda for her kind and loyal support, whenever it was needed the most.

S.M.S. for the changes in perspective.

Bibliography

[1] Alexander Franzen. *ComponentLibrary*. https://creativecommons.org/licenses/by-nc/3.0/. URL: http://www.gwoptics.org/ComponentLibrary/.

[2] Isaac Newton. *Mathematische Principien der Naturlehre*. Ed. by Jakob Philipp Wolfers 1872. 1687. URL: https://de.wikisource.org/wiki/Mathematische_Principien_der_Naturlehre.

[3] Chris Pollock. "Mercury's Perihelion". In: (2003). URL: https://www.math.toronto.edu/~colliand/426_03/Papers03/C_Pollock.pdf.

[4] B. P. Abbott et al. "Observation of Gravitational Waves from a Binary Black Hole Merger". In: *Physical Review Letters* 116.6 (2016), p. 061102. ISSN: 1079-7114. DOI: 10.1103/physrevlett.116.061102.

[5] A. Einstein and N. Rosen. "On gravitational waves". In: *Journal of the Franklin Institute* 223.1 (Jan. 1937), pp. 43–54. ISSN: 0016-0032. DOI: 10.1016/s0016-0032(37)90583-0.

[6] Albert Einstein. "122. Explanation of the Perihelion Motion of Mercury by Means of the General Theory of Relativity". In: *A Source Book in Astronomy and Astrophysics, 1900–1975*. Harvard University Press, Dec. 1979, pp. 820–825. DOI: 10.4159/harvard.9780674366688.c131.

[7] Peter R. Saulson. *Fundamentals of interferometric gravitational wave detectors*. Second edition. World Scientific, 2017. URL: http://tib-hannover.eblib.com/patron/FullRecord.aspx?p=4818761.

[8] J. Weber. "EVIDENCE FOR DISCOVERY OF GRAVITATIONAL RADIATION". In: *Physical Review Letters* 22.24 (1969), pp. 1320–1324.

[9] Odylio Denys Aguiar. "The Past, Present and Future of the Resonant-Mass Gravitational Wave Detectors". In: *Research in Astronomy and Astrophysics* 11.1 (Sept. 6, 2010), pp. 1–42. DOI: 10.1088/1674-4527/11/1/001. arXiv: 1009.1138 [astro-ph.IM].

[10] Joel M. Weisberg, Joseph H. Taylor, and Lee A. Fowler. "Gravitational waves from an orbiting pulsar." In: *Scientific American* 245 (1981), pp. 66–74.

[11] The Royal Swedish Academy of Sciences. "The Nobel Prize in Physics 1993". In: (1993). URL: https://www.nobelprize.org/prizes/physics/1993/press-release/.

[12] B.P. Abbott et al. "GW170817: Observation of Gravitational Waves from a Binary Neutron Star Inspiral". In: *Physical Review Letters* 119.16 (Oct. 2017), p. 161101. ISSN: 1079-7114. DOI: 10.1103/physrevlett.119.161101.

[13] R. Abbott et al. "Observation of Gravitational Waves from Two Neutron Star–Black Hole Coalescences". In: *The Astrophysical Journal Letters* 915.1 (June 2021), p. L5. ISSN: 2041-8213. DOI: 10.3847/2041-8213/ac082e.

[14] Konstantin Leyde. *Testing general relativity and cosmology withgravitational waves.* Université Paris Cité, 2023.

[15] Einstein Telescope steering committee editorial team. *Design Report Update 2020 for the Einstein Telescope.* Tech. rep. Sept. 2020. eprint: https://apps.et-gw.eu/tds/?call_file=ET-0007B-20_ETDesignReportUpdate2020.pdf. URL: http://www.et-gw.eu.

[16] S. Danilishin T. Zhang. *Conceptual Design and Noise Budget of Einstein Telescope.* 2023. URL: https://indico.ego-gw.it/event/562/contributions/5273/attachments/2781/4898/ET_Sensitivity_Curve_Update.pdf.

[17] ET collaboration. *ET noise budget git.* URL: https://gitlab.et-gw.eu/et/isb/interferometer/ET-NoiseBudget.

[18] LIGO Scientific Collaboration. *PyGWINC.* Ligo Scientific Collaboration. visited 20.03.2023. URL: https://git.ligo.org/gwinc/pygwinc.

[19] Einstein Telescope science team. *Einstein gravitational wave Telescope conceptual design study*. Tech. rep. June 2011. eprint: https://tds.virgo-gw.eu/?call_file=ET-0106C-10.pdf. URL: http://www.et-gw.eu.

[20] Christopher C. Gerry and Peter L. Knight. *Introductory Quantum Optics*. Cambridge University Press, 2023. ISBN: 9781009415293.

[21] Roman Schnabel. "Squeezed states of light and their applications in laser interferometers". In: *Physics Reports* 684 (Apr. 2017), pp. 1–51. ISSN: 0370-1573. DOI: 10.1016/j.physrep.2017.04.001.

[22] Albert A Michelson. "ART. XXI.–The relative motion of the Earth and the Luminiferous ether". In: *American Journal of Science (1880-1910)* 22.128 (1881), p. 120.

[23] Orazio Svelto. *Principles of Lasers*. Vol. Fifth edition. 2010. DOI: 10.1007/978-1-4419-1302-9.

[24] R. Paschotta. "Mode-locked Lasers - an encyclopedia article". In: *RP Photonics Encyclopedia*. RP Photonics AG, 2005. DOI: 10.61835/7dz.

[25] J J Fendley. "Measurement of refractive index using a Michelson interferometer". In: *Physics Education* 17.5 (Sept. 1982), pp. 209–211. ISSN: 0031-9120. DOI: 10.1088/0031-9120/17/5/001.

[26] J. V. Knuuttila, P. T. Tikka, and M. M. Salomaa. "Scanning Michelson interferometer for imaging surface acoustic wave fields". In: *Optics Letters* 25.9 (May 2000), p. 613. ISSN: 1539-4794. DOI: 10.1364/ol.25.000613.

[27] C.H.F. Velzel. "Inverse Fourier spectroscopy". In: *Optics Communications* 4.2 (Oct. 1971), pp. 121–124. ISSN: 0030-4018. DOI: 10.1016/0030-4018(71)90223-9.

[28] Hans-Albert Bachor. *A guide to experiments in quantum optics*. Ed. by Timothy C. Ralph. 3. ed. Wiley-VCH, 2019, p. 588. URL: https://onlinelibrary.wiley.com/doi/book/10.1002/9783527695805.

[29] Jan Petermann. "Suspended Mirror Pendulum with Radiation Pressure Compensated Laser-Interferometric Position Readout". en. Accepted: 2022-09-09T10:32:41Z Publisher: Staats- und Universitätsbibliothek Hamburg Carl von Ossietzky. PhD thesis. 2022. URL: https://ediss.sub.uni-hamburg.de/handle/ediss/9800 (visited on 09/13/2022).

[30] Mikhail Korobko. "Taming the quantum noise: How quantum metrology can expand the reach of gravitational-wave observatories". PhD thesis. Universität Hamburg, 2020. URL: https://ediss.sub.uni-hamburg.de/handle/ediss/8460.

[31] Leonard Bergstein. "Modes of Stable and Unstable Optical Resonators". In: *APPLIED OPTICS* 7.3 (Mar. 1968), pp. 495–503. DOI: 10.1364/AO.7.000495.

[32] Robert Cole Christopher Moore and Christopher Berry. *Gravitational Wave Detectors and Sources.* University of Cambridge. URL: http://www.sr.bham.ac.uk/~cplb/GWplotter/.

[33] N A Robertson et al. "Passive and active seismic isolation for gravitational radiation detectors and other instruments". In: *Journal of Physics E: Scientific Instruments* 15.10 (1982), pp. 1101–1105. DOI: 10.1088/0022-3735/15/10/032.

[34] F.Ya.Khalili. "Reducing the mirrors coating noise in laser gravitational-waveantennae by means of double mirrors". In: *Applied Optics* 45 (2006), pp. 1569–1574. DOI: https://doi.org/10.48550/arXiv.gr-qc/0406071. URL: https://arxiv.org/pdf/gr-qc/0406071.pdf.

[35] Alexey G. Gurkovsky et al. "Reducing thermal noise in future gravitational wave detectors by employing Khalili etalons". In: *Physics Letters A* 375.46 (2011), pp. 4147–4157. ISSN: 0375-9601. DOI: https://doi.org/10.1016/j.physleta.2011.07.063. URL: https://www.sciencedirect.com/science/article/pii/S037596011101142X.

[36] G. M. HARRY et al. "THERMAL NOISE FROM OPTICAL COATINGS". In: *The Tenth Marcel Grossmann Meeting*. World Scientific Publishing Company, Feb. 2006. DOI: 10.1142/9789812704030_0257.

[37] Gregory M. Harry, Timothy P. Bodiya, and Riccardo DeSalvo. *Optical coatings and thermal noise in precision measurement.* Cambridge University Press, 2012, p. 344. ISBN: 9781107003385.

[38] Gregory Harry. "Optical Coatings andThermal Noise in Precision Measurements". In: *Embry-Riddle AeronauticalUniversity Physics Colloquium* (Oct. 2011). URL: https://dcc.ligo.org/public/0072/G1101150/001/G1101150.pdf.

[39] Lucia Trozzo and Francesca Badaracco. "Seismic and Newtonian Noise in the GW Detectors". In: *Galaxies* 10.1 (2022). ISSN: 2075-4434. DOI: 10.3390/galaxies10010020. URL: https://www.mdpi.com/2075-4434/10/1/20.

[40] M G Beker et al. "Newtonian noise and ambient ground motion for gravitational wave detectors". In: *Journal of Physics: Conference Series* 363 (2012), p. 012004. DOI: 10.1088/1742-6596/363/1/012004.

[41] Jennifer C. Driggers, Jan Harms, and Rana X. Adhikari. "Subtraction of Newtonian noise using optimized sensor arrays". In: *Physical Review D* 86.10 (Nov. 2012), p. 102001. ISSN: 1550-2368. DOI: 10.1103/physrevd.86.102001.

[42] James Lough et al. "First Demonstration of 6 dB Quantum Noise Reduction in a Kilometer Scale Gravitational Wave Observatory". In: *Physical Review Letters* 126.4 (2021), p. 041102. DOI: 10.1103/physrevlett.126.041102.

[43] F. Acernese et al. "Quantum Backaction on Kg-Scale Mirrors: Observation of Radiation Pressure Noise in the Advanced Virgo Detector". In: *Physical Review Letters* 125.13 (2020), p. 131101. DOI: 10.1103/physrevlett.125.131101.

[44] R. Paschotta. *phase noise.* RP Photonics Encyclopedia. [Online; accessed 24-Octobre-2023]. URL: https://www.rp-photonics.com/phase_noise.html.

[45] R. Paschotta. *laser noise.* RP Photonics Encyclopedia. [Online; accessed 24-Octobre-2023]. URL: https://www.rp-photonics.com/laser_noise.html.

[46] R. Paschotta. *frequency noise.* RP Photonics Encyclopedia. [Online; accessed 24-Octobre-2023]. URL: https://www.rp-photonics.com/frequency_noise.html.

[47] R. Paschotta. *intensity noise*. RP Photonics Encyclopedia. [Online; accessed 24-Octobre-2023]. URL: `https://www.rp-photonics.com/amplitude_squeezed_light.html`.

[48] R. Paschotta. *quantum noise*. RP Photonics Encyclopedia. [Online; accessed 24-Octobre-2023]. URL: `https://www.rp-photonics.com/quantum_noise.html`.

[49] R. Paschotta. *shot noise*. RP Photonics Encyclopedia. [Online; accessed 24-Octobre-2023]. URL: `https://www.rp-photonics.com/shot_noise.html`.

[50] R. Paschotta. *radiation pressure*. RP Photonics Encyclopedia. [Online; accessed 24-Octobre-2023]. URL: `https://www.rp-photonics.com/radiation_pressure.html`.

[51] R. Paschotta. *Amplitude-squeezed light*. RP Photonics Encyclopedia. [Online; accessed 24-Octobre-2023]. URL: `https://www.rp-photonics.com/intensity_noise.html`.

[52] Jan 1952 Lunze. *Regelungstechnik 1 systemtheoretische Grundlagen, Analyse und Entwurf einschleifiger Regelungen : mit 77 Beispielen, 186 Übungsaufgaben sowie einer Einführung in das Programmsystem MATLAB*. Ed. by Springer-Verlag GmbH. 12., überarbeitete Auflage. Lehrbuch: Springer eBook Collection. Springer Vieweg, 2020. URL: `https://doi.org/10.1007/978-3-662-60746-6`.

[53] R. W. P. Drever et al. “Laser phase and frequency stabilization using an optical resonator”. In: *Applied Physics B Photophysics and Laser Chemistry* 31.2 (1983), pp. 97–105. DOI: `10.1007/bf00702605`.

[54] LSC. “GWTC-2: Compact Binary Coalescences Observed by LIGO and Virgo During the First Half of the Third Observing Run”. In: *LIGO DCC* (2020). URL: `https://dcc.ligo.org/LIGO-P2000061/public`.

[55] Pascal Gewecke. *The squeeze laser and its applications in quantum sensing*. Universität Hamburg, 2024.

[56] Maximilian Faden. “The Hamburg Gravitational-Wave DetectorPrototype of the Einstein Telescope”. MA thesis. Universität Hamburg, 2023.

[57] Sebastian Steinlechner. *Linear Cavity Calculator*. website. 2016. URL: https://sestei.github.io/jscav/.

[58] ETpathfinder Team. "ETpathfinderDESIGN REPORT". In: (2020).

[59] W. Kells G. Billingsley G. Harry. *Core Optics ComponentsDesign Requirements Document*. Tech. rep. LIGO Laboratory / LIGO Scientific Collaboration, 2015. URL: https://dcc.ligo.org/public/0011/T000127/004/COC_Design_Requirements_T000127-v4.pdf.

[60] uwe electronic GmbH. *Die 30 goldenen Regeln der Peltiertechnologie*. Tech. rep.

[61] uwe electronic GmbH. *Hintergrundwissen - Leistungsdiagramme Peltiertechnologie*. Tech. rep. URL: https://www.uweelectronic.de/de/temperaturmanagement-2/peltierelemente/hintergrundwissen.html.

[62] ASM International. "Thermal Expansion". In: (). URL: https://www.owlnet.rice.edu/~msci301/ThermalExpansion.pdf.

[63] Daniel Hartwig. "Working title - Mitigating seismic noise in pendulum suspensions for gravitational wave detection". PhD thesis. Universität Hamburg, 2024.

[64] M.G. Olsson Robert A. Nelson. "The pendulum - Rich physics from a simple system". In: *Am.J.Phys.* 54 (1985).

[65] Gabriela González. "Resonances, quality factors in LIGO pendulums: a compendium of formulas". In: (2001).

[66] Sophie Verclas. "Seismische Charakterisierung eines Versuchslabors für die Laserinterferometrie". Bachelors Thesis. Universität Hamburg, July 2018.

[67] Heidelberg Materials. *BetontechnischeDaten*. Tech. rep. 2022. URL: https://www.betontechnische-daten.de/de.

[68] Newport. *S-2000A Stabilizer™ Top Performance Pneumatic Vibration Isolators with Automatic Re-Leveling*. URL: https://www.newport.com/f/pneumatic-vibration-isolators-with-automatic-re-leveling.

[69] Newport. *Optical Table Selection Guide Compliance Curve*. URL: https://www.newport.com/f/tuned-damped-top-performance-optical-tables?.

[70] A. Franke et al. “Finite Element Simulations of Optomechanical Components”. MA thesis. 2019. URL: https://books.google.de/books?id=rv1RzQEACAAJ.

[71] Justin Nico Hohmann. “Construction of a Michelson interferometer under ultra-high vacuum conditions”. MA thesis. Universität Hamburg, 2019.

[72] Christian Darsow-Fromm et al. “NQontrol: An open-source platform for digital control-loops in quantum-optical experiments”. In: *Review of Scientific Instruments* 91.3 (2020). DOI: 10.1063/1.5135873.

[73] Nima Ehsani Armaki. “Working title - Aktive Seismikisolierung eines optischen Tisches mittelsgeschlossener Regelung via DC-Linearaktuatoren”. In: ().

[74] Roman Schnabel. *Lecture on gravitational wave detection*. 2022.

[75] Lise Schnupp. *Talk at a European Collaboration meeting on interferometric detection of gravitational waves in Sorrento*. 1988.

[76] Kernel density estimation. URL: https://en.wikipedia.org/wiki/Kernel_density_estimation.

[77] URL: https://en.wikipedia.org/wiki/Gaussian_function.

Eidesstattliche Versicherung / Declaration on oath

Hiermit versichere ich an Eides statt, die vorliegende Dissertationsschrift selbst verfasst und keine anderen als die angegebenen Hilfsmittel und Quellen benutzt zu haben. Sofern im Zuge der Erstellung der vorliegenden Dissertationsschrift generative Künstliche Intelligenz (gKI) basierte elektronische Hilfsmittel verwendet wurden, versichere ich, dass meine eigene Leistung im Vordergrund stand und dass eine vollständige Dokumentation aller verwendeten Hilfsmittel gemäß der Guten wissenschaftlichen Praxis vorliegt. Ich trage die Verantwortung für eventuell durch die gKI generierte fehlerhafte oder verzerrte Inhalte, fehlerhafte Referenzen, Verstöße gegen das Datenschutz- und Urheberrecht oder Plagiate.

Hamburg, den 29. April 2024

Unterschrift der Doktorandin / des Doktoranden